12-7-2012 12:00 AM

# Wireless Telemetry System for Implantable Sensors

Kyle G. Fricke
*The University of Western Ontario*

Supervisor
Dr. Sobot
*The University of Western Ontario* Joint Supervisor
Dr. Dounavis
*The University of Western Ontario*

Graduate Program in Electrical and Computer Engineering
A thesis submitted in partial fulfillment of the requirements for the degree in Master of Engineering Science

# WIRELESS TELEMETRY SYSTEM FOR IMPLANTABLE SENSORS
(Spine title: Wireless Telemetry System for Implantable Sensors)
(Thesis format: Monograph)

by

Kyle Fricke

Graduate Program in Electrical and Computer Engineering

A thesis submitted in partial fulfillment
of the requirements for the degree of
Master of Engineering Science

The School of Graduate and Postdoctoral Studies
The University of Western Ontario
London, Ontario, Canada

THE UNIVERSITY OF WESTERN ONTARIO
School of Graduate and Postdoctoral Studies

# CERTIFICATE OF EXAMINATION

Supervisor:

.....
Dr. Robert Sobot

Co-Supervisor:

.....
Dr. Anestis Dounavis

Examiners:

.....
Dr. George Knopf

.....
Dr. James Lacefield

.....
Dr. Mohammad Dadash Zadeh

The thesis by

**Kyle Gary Fricke**

entitled:

**Wireless Telemetry System for Implantable Sensors**

is accepted in partial fulfillment of the
requirements for the degree of
Master of Engineering Science

.....
Date

.....
Chair: Dr. Vijay Parsa

# Abstract

Advanced testing of medical treatments involves experimentation on small laboratory animals, such as genetically modified mice. These subjects are used to help researchers develop medication and cures for humans. To understand the effects of the treatments, innovative telemetry systems are developed, that enable remote real–time cardiac monitoring. The latest research in the field of cardiac monitoring has revealed two major limitations with wireless implantable systems: a) the current size of implantable electronics limits the physical size of the system to larger subjects; and b) the systems only interface with one sensor type (e.g., pressure sensor only). This research focuses on the design of a wireless telemetry system architecture, intended to retrieve blood pressure and volume data. A physical prototype is created that is 2.475 $cm^3$ and weights 4.01 g. This thesis will enable a path towards miniaturization, leading to the incorporation of a wireless system into small laboratory animals.

**Keywords:** mixed–signal, implantable, bio–medical applications, digital–signal–processing, radio frequency, sensors, pressure–volume, low–power, admittance, lock–in amplifier

# Acknowledgements

First and foremost, I would like to thank my supervisors Dr. Robert Sobot and Anestis Dounavis. I greatly appreciate their guidance and support not only in this research, but also throughout my university career. I also would like to express my thanks to my present colleagues in our research group for their care and assistance. Furthermore, I would like to thank my family for believing in me and encouraging me in my studies. I would like to acknowledge the Natural Sciences and Engineering Research Council of Canada (NSERC), CMC Microsystems, CFI, our industrial sponsor Scisense Inc. and The University of Western Ontario for providing the facilities and funding that made this research possible.

# Table of Contents

# List of Figures

# List of Tables

# List of Abbreviations, Symbols, and Nomenclature

| | |
|---|---|
| **CMOS** | Complementary Metal Oxide Semiconductor |
| **RF** | Radio Frequency |
| **AC** | Alternate Current |
| **DC** | Direct Current |
| **WPT** | Wireless Power Transmission |
| **MEMS** | Micro-Electro-Mechanical System |
| **ADC** | Analog-To-Digital Converter |
| **VCO** | Voltage Controlled Oscillator |
| **rms, RMS** | Root-Mean-Square |
| **PCB** | Printed Circuit Board |
| **PV** | Pressure – Volume |
| **IC** | Integrated Circuit |
| **LV** | Left Ventricle |
| **SV** | Stroke Volume |
| **ED** | End Diastolic |
| **ES** | End Systolic |
| **CO** | Cardiac Output |
| **EDV** | End Diastolic Volume |
| **EDP** | End Diastolic Pressure |
| **ESV** | End Systolic Volume |
| **ESP** | End Systolic Pressure |
| **EF** | Ejection Fraction |
| **SW** | Stroke Work |
| **MRI** | Magnetic Resonance Imaging |
| **PSD** | Phase Sensitive Detector |
| **LPF** | Low Pass Filter |
| **LDO** | Low Drop Out |
| **Iq** | Current Consumption |
| **TI** | Texas Instruments |
| **PSSR** | Power Supply Rejection Ratio |
| **dB** | Decible |
| **SPST** | Single Pole Single Throw |
| **SPI** | Serial Peripheral Interface |

| | |
|---|---|
| **GPIO** | General Digital Input and Output |
| **DCO** | Digital Controlled Oscillator |
| **CPU** | Center Processing Unit |
| **LPM** | Low–Power Mode |
| **IDE** | Integrated Development Environment |
| **ISM** | Industrial, Scientific and Medical |
| **SRD** | Short Range Device |
| **FSK** | Frequency Shift Keying |
| **HF** | High Frequency |
| **USB** | Universal Serial Bus |
| **ECG** | Electrocardiogram |
| **OP-Amp** | Operational Amplifier |
| **POT** | Potentiometer |
| **SNR** | Signal to Noise Ratio |
| **XOR** | Exclusive OR |
| **SPICE** | Simulation Program with Integrated Circuit Emphasis |
| **LED** | Light Emitting Diode |
| **IA** | Instrumentation Amplfier |
| **BALUN** | Balanced–Unbalanced |
| **LTCC** | Low Temperature Co-Fired Ceramic |
| **BNC** | Bayonet Neill–Concelman Connector |
| **SMA** | Sub Miniature Connector Version A |
| **FFC** | Flat Flex Cable |
| **CAD** | Computer Aided Design |

# Chapter 1

# Introduction

## 1.1 Motivation

The development of medical treatments for humans strongly depends on lab experiments involving small animals. These test subjects are genetically modified and injected with treatments for medical diseases. Researchers monitor various bio–signals during these experiments including blood pressure, temperature, blood volume, electrocardiography (ECG), Electroencephalography (EEG), etc. to understand the effects of the treatments on the subject's body. Through the use of modern telemetry systems, these bio-medical signals can be measured in real–time from inside a living body. Researchers can use this data to develop new treatments for many human diseases such as cardiovascular disease [2–4].

Telemetry systems are able to capture, process and transmit specific information to an end device, wired or wirelessly. These systems contain sensors to measure the bio–medical data from inside the living body and can be external, for example in ECG, EEG monitoring or implantable in the case of most cardiac monitoring. Implantable telemetry systems are found in many different areas of medicine including diagnostics and monitoring [5], drug delivery systems [6], neurology [7], audiology [8], and cardiology [9]. Many issues exist with the current implementations of such systems including size restrictions, power consumption, number of

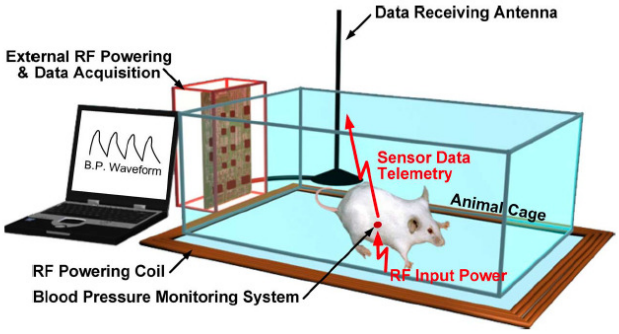


Figure 1.1: Wireless implantable system measuring environment, Cong [1] © IEEE 2010.

sensors used etc. These issues are significantly more important for cardiac research due to the size of the animals involved.

Real–time left ventricular (LV) pressure–volume (PV) loops have become the main analysis for understanding the health of myocardium in animals and humans [10]. PV loops allow researchers to quantify cardiac pathology, such congestive heart failure [11] [12]. To obtain this data, a small catheter is inserted into the left ventricle (LV) of the heart where measurements are taken. Pressure and volume measurements are captured separately by different electronic systems. A pressure measurement is acquired by using a solid state pressure sensor where the pressure from the blood will react with the sensor to cause a potential difference representing the pressure signal [13]. A volume measurement is obtained by using a four electrode catheter system inserted into the subject's left ventricle to generate an electric field and to continuously measure the conductance or admittance from the animal which is converted to volume [14].

Currently, the catheter is attached to an external base station where the main processing occurs. This does not allow the animal to move freely in their normal environment. To solve this, an implant is used, creating a measuring environment similar to the one outlined by Cong [1], Fig. 1.1. The implant would contain all sensor electronics as well as power and data transmission electronics. However, realistic design constraints are driven by the subject's body size and the implant's power consumption. Larger subjects (e.g. a cow or a human) can accept an implant whose volume is in the order of a few tens of cubic centimetres, while a tiny mouse

body can only tolerate a fully implanted object with the volume in the order of a few tens of cubic millimetres. Power consumption is also of great importance to the implantable system as decreased power consumption can lead to smaller battery sizes, further reducing the systems volume. A low–power telemetry system is capable of being implanted for longer periods of time while operating off of smaller capacity batteries. The proposed research focuses on creating a small wireless telemetry system suited for cardiac research that enables a path towards miniaturization, which can be incorporated into small laboratory animals such as a mouse. This research aims at establishing a benchmark for future research and development in the increasingly demanding field of miniaturized wireless implantable systems.

## 1.2 Research Objectives

The aim of this thesis is to develop a prototype of a discrete level, miniature, short–distance, low–power RF wireless telemetry system suited for small animal subjects. This system is designed to measure blood pressure and volume data from small laboratory animals (e.g., mice, rats, rabbits). The objectives of this thesis are:

- To create a telemetry system architecture suited for implantable applications. This architecture should contain all system level blocks to allow for data collection, processing, and transmutation to an end device for post processing. Prototypes should be created to test the designed architecture.

- To acquire pressure–volume measurements, a sensor interface must be developed to deliver excitation signals to the test subject and convert the measure voltages to valid application data.

- This research should advance the knowledge of RF implantable systems by providing a detailed literature review and insights on the trends in this research field.

## 1.3 Organization of the Thesis

In this thesis an architecture of an implantable system is developed leading to the manufacturing of two miniature discrete level prototypes using modern PCB techniques.

In Chapter 2, background into implantable systems is presented, indicating main research areas. Furthermore, pressure–volume loops are introduced along with background information on blood pressure and volume measurement techniques in small laboratory animals. In addition, theoretical concepts of lock–in amplifiers are discussed.

In Chapter 3, the proposed implantable wireless telemetry system architecture is discussed block by block in detail. The architecture consists of four main modules: power supply, signal and data processing, RF transmission, and sensor interface.

In Chapter 4, two discrete level prototypes are developed, one for poof–of–concept and a second to minimize the overall volume of the structure to a level where it can be implanted. Simulation results of the designed sensor interface modules are presented along with preliminary test setups and power consumption results.

The research work is summarized in Chapter 5. Achievements are listed, and suggestions for future work are presented.

# Chapter 2

# Wireless Measurement Background

In the previous chapter a brief overview of the research problems, motivation, and objectives was stated. In this chapter, implantable systems are introduced along with examples in specific active research areas to provide the reader with knowledge in this field. Basic concepts are introduced that provide background knowledge into pressure–volume measurement techniques in small lab animals as well as theoretical concepts of lock–in amplifiers. This background knowledge provides a basic understanding of the application subject and the required theoretical knowledge for sub–blocks used in the wireless telemetry system.

## 2.1 Implantable Systems

An implantable system is generally referred to as any device/system that is intended to function inside a living body for either short or long term use [15]. Implantable systems provide a method to improve the quality of life of living beings as well as provide monitoring techniques for various medical applications. The specific advantages of implantable devices in comparison to other monitoring methods such as magnetic resonance imaging (MRI), CT scans, etc are their small size [16], low weight [17], low power [18], and increased functionality [16]. As these mico–systems are dealing with living bodies, they require additional research into areas such as packaging [19], reliability [20], and bio–compatibility [21]. To achieve these various

measurements, different types sensors are utilized to convert the bio–signals to electrical data for processing. The most common sensor used is a pressure based sensor. These different sensors are utilized in many application areas such as retinal [18] [22], neurological [7] [23] [24], and cardiac [9]. In addition, the focus on power consumption, small size and wireless power are common themes found throughout the different application areas that implantable telemetry systems are utilized.

For example, the most recent advancements in retinal implantable systems have been achieved by Shih [18]. Here, Shih presents a 2.3 $\mu W$ wireless intraocular pressure/temperature implant. This implant is used to monitor intraocular pressures that are used in the diagnosis and treatment of glaucoma. In addition, Yang [22] has researched inductor modelling to wirelessly power such retinal implants. These retinal implantable systems have the potential to greatly improve the monitoring of such diseases as well as the possibility of early detection before current diagnostic methods can.

Another major application area for implantable systems is in neurological research. For instance, Neihart [24] presents a low–power bidirectional telemetry system that is designed to be fully implanted inside a human body for neural recording applications. Additional research into the area of neurological research was achieved by Ghovanloo [23] who developed an implantable system which contained a multichannel mircostimulating system–on–a–chip. This system was designed to work as a neural protheses. These systems are able to emulate natural neurological functions that are damaged and provide rehabilitation to the patient. Auditory and visual prostheses are examples that this device strives to emulate. One of the most recent publications presented on neurological applications of implantable systems was by Lee [7]. He presented an inductively powered wireless neural recording system, that contained a 14.19 $mm^2$ integrated circuit that consumes 5.85 $mW$. This system is able to record neural behaviour on a small animal while allowing the subject to freely move around. Implantable systems for neurological research purposes provide methods to monitor and stimulate brain functions to improved diagnosis and long term health care of patients with neurological disorders.

Implantable systems are actively researched in other application areas as well such as blood glucose motoring [25], drug delivery systems [26], and blood flow measurements [27]. A wireless implantable microsystem for blood glucose monitoring is presented in 2009 by Ahmadi [25]. These types of implants allow for diabetic patients to monitor their glucose levels in real time and can help reduce symptoms associated with diabetes as well [28]. Smith [26] proposed a miniaturized drug delivery system for delivering medications to the eye. These types of systems allow doctors to control the exact dosage and delivery areas for maximum effectiveness. In 2010, Khannur [27] presented an implantable IC for blood flow measurements within prosthetic grafts. These types of systems allow doctors to monitor and created better treatments for vascular based diseases. In addition to the major application areas above, much research is being conducted on specific features of implantable telemetry systems such as antenna design [29] [30], wireless powering [31] [32], and RF transmitters [5] [33].

However, the most important application area to this research is the field of cardiac monitoring. Most recently, researchers have focused on creating a wireless implantable system with integrated blood pressure sensors. These systems range from creating a fully implantable cardiovascular pressure monitor with a medical stent [9] to a fully implantable blood pressure sensor for hypertonic patients [34]. The most recent research in this application area is in cardiac monitoring of small animals. New research challenges occur such as reduced implantable area when dealing with smaller sized subjects over larger ones (e.g., humans). This prevents larger external components from being used along with larger power sources. Most recently in 2010, Cong [1] proposed a wireless batteryless implantable blood pressure monitoring microsystem for small laboratory animals. This publication represents the state–of–the–art in the field of murine cardiac monitoring. Cong's implantable system employes a blood pressure cuff to measure the blood pressure around the blood vessel it is attached to. The pressure cuff is made from bio–compatible materials and contains an internal MEMS pressure sensor. The fully implantable system dissipates 300 $\mu W$ and was experimentally tested. The complete size of the wireless system is 6.4 mm diameter with a length of 4 mm and was also powered wire-

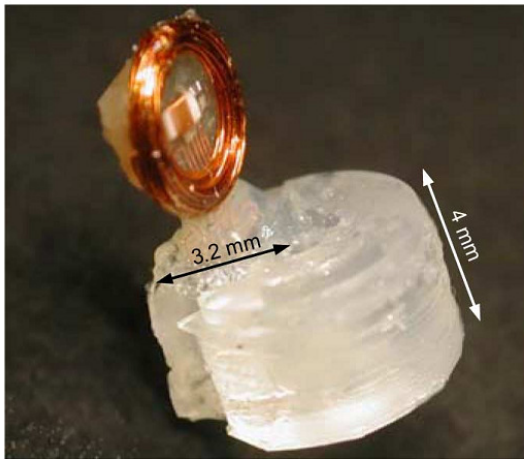


Figure 2.1: Implantable wireless telemetry system featuring a cuff blood pressure sensor, Cong [1] © IEEE 2010.

lessly via RF, Fig. 2.1. However, Cong's implantable system is only focused on blood pressure monitoring and does not combine any additional sensors to provide increased functionality. One such sensor is a blood volume sensor.

Implantable systems incorporating blood volume sensors for small animals have been an area that has yet to be exploited to its full potential. Currently, the majority of blood volume monitoring systems are what is known as tethered systems (i.e., attached to an end unit). These are generally commercially available from manufactures such as Scisense Inc. and Millar Instruments Inc. These systems obtain their power and communication from attached end units. The reason that these telemetry systems still remain wired is the increased external component count needed when dealing with accurate blood volume measurements in comparison to simpler blood pressure measurements. By being tethered to an end unit the test subject is not allowed to move freely in their own natural environment and may affect the measurement results [35]. The solution to this would be to create a wireless implantable system similar to Cong's implantable pressure system [1] but incorporate blood volume sensors as well. Preliminary research has been completed on this topic by Uemura [36] in 2004. Uemura et al. developed an implantable pressure–volume telemetry system. This was one of the first implantable systems that incorporated pressure and volume sensors. The telemetry system communicated

with an end unit using Bluetooth wireless technology. However, this telemetry system had a few drawbacks. First, the telemetry system was quite large as it used a programmable digital logic device and other large components to preform the processing. This increased the overall weight to 26 g. The second drawback of this initial telemetry system is that the conductance technique was used to measure volume rather than admittance and it also used a dual frequency method to remove parallel capacitance from the measured volume. This reduces the accuracy of the volume measurements as is documented in the following subsection. Raghavan [35] built upon this initial research to create an improved wireless telemetry system. Raghaven et al. created a new improved telemetry system that is built using analog circuitry with a printed circuit board size of 17.67 $cm^2$. This system improved over the previous system by using admittance based measurements rather than conductance methods, providing more accurate volume measurements. Although, the implantable system developed in [35] represents the latest research into pressure–volume telemetry systems, there are still drawbacks and areas of improvement. The size and weight of this telemetry system are still quite large for small animals, with the weight at 27 g, as noted in [35]. Therefore, it can be concluded that further miniaturization in size, weight, and power are required to improve the quality and length of pressure–volume measurements.

## 2.2 Pressure–Volume Loops

The heart is the most important muscle in the human body, as it regulates and pumps blood throughout the living body. The heart contains four chambers, two atria and two ventricles (left and right), Fig. 2.2. The left ventricle (LV) is generally studied over the right ventricle because it supplies blood to the whole body rather than just the lungs, as the right ventricle does, therefore accomplishes the majority of work in the heart [37]. In addition, the left ventricle pumps blood at a much higher pressures than the right ventricle. Two measurements, blood pressure and volume, of the LV provide insight into the efficiency of the living heart.

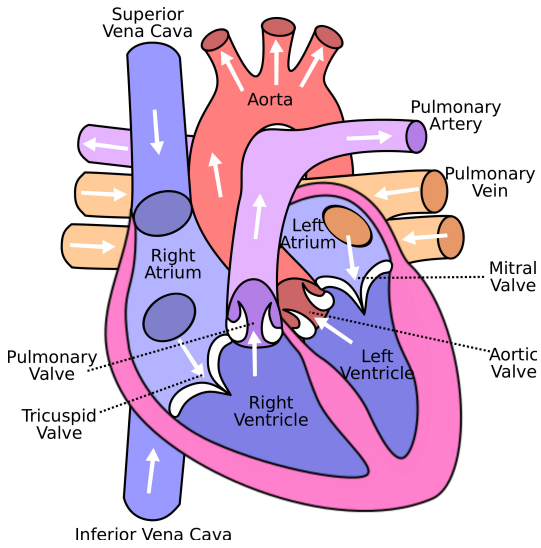


Figure 2.2: Diagram of a human heart, displaying the right and left atriums and ventricles.

Combining the measurement of the LV volume with measured LV pressure, pressure–volume (PV) loops can be created, allowing for the extraction of various medical parameters.

A pressure–volume loop can be described as the PV relationship during a cardiac cycle. Here, the four stages of the cardiac cycle: diastolic filling, contraction, ejection (systolic phase), relaxation are represented by various blood pressure and volume values [38] [39], Fig. 2.3. A brief overview of these four stages is given below:

- Stage 1: Diastolic Filling: During this stage the LV muscles relax to allow for the increase in blood volume. The blood pressure during this stage is relatively low and constant and the blood volume increases to its highest level.

- Stage 2: Contraction: This stage begins when the LV blood filling is complete. The mitral valve closes and the cardiac muscle starts to contract to increase blood pressure inside the LV. The blood volume during this stage is generally constant at its highest value and the blood pressure is constantly increasing. At the beginning of this stage two important parameters are measured, A in Fig. 2.3, end–diastolic volume (EDV) and end–diastolic pressure (EDP). EDV and EPV represent the value of blood volume and pressure in the heart at the time filling is complete [38].

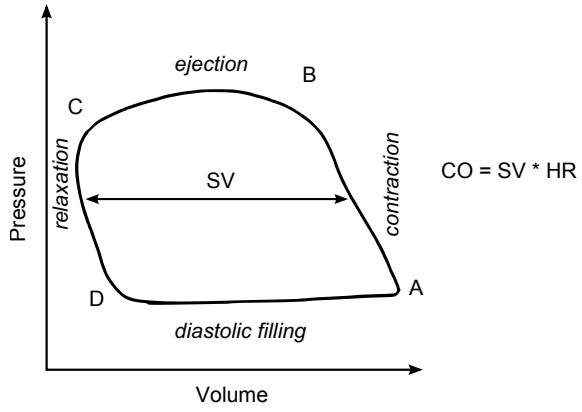


Figure 2.3: Pressure vs Volume loop (PV) Loop where A is the end-diastolic (ED) point, B represents the point where the aortic valve opens, C is the end-systolic (ES) point, D represents where the mitral valve opens. Stroke Volume (SV) is calculated by subtracting ES volume from ED volume. This is used to calculate the Cardiac Output (CO) in conjunction with the heart rate.

- Stage 3: Ejection (Systolic Phase): This stage begins at B in Fig. 2.3, where the aortic valve opens up and the blood is ejected into the blood stream. The heart muscles continue to contract to get the maximum blood ejection. The blood volume reduces to its minimum value during this stage

- Stage 4: Relaxation: The start of stage 4 ends the Systolic phase and the heart muscles begin to relax (i.e., reduce blood pressure) to allow the LV can refill and repeat the cycle. At the beginning of this stage two important parameters are measured, C in Fig. 2.3, end–systolic volume (ESV) and end–systolic pressure (ESP). ESV and ESP represent the value of blood volume and pressure in the heart at the time ejection is complete [38]. The during this stage the blood volume is at its lowest and the pressure is reduced to its minimum.

Specific cardiac parameters can be calculated from PV loops. Some of these include: stroke volume (SV), stroke work (SW), cardiac output (CO), ejection fraction (EF), etc [38], outlined in Table 2.1 with a small example located in Table 2.2.

By analyzing PV loops and extracting the various cardiac parameters, doctors can analyze the efficiency of the heart. This process allows the study of a variety of cardiac medical

Table 2.1: Various cardiac parameters

| Cardiac Parameter | Description | Formula |
|---|---|---|
| SV – Stroke Volume | Volume of blood being pumped with each beat | $SV = EDV - ESV$ |
| SW – Stroke Work | Mechanical work done by the heart muscle | $SW$ = Area inside PV loop |
| CO – Cardiac Output | Volume of blood being pumped by the heart in 1 min | $CO = SV x\ Heart\ Rate$ |
| EF – Ejection Fraction | Volumetric fraction of blood pumped out of the LV with each heart beat | $\frac{SV}{EDV} \times 100\%$ |

Table 2.2: Example of cardiac parameters

| Parameters given | Calculated Parameters |
|---|---|
| EDV = 130 mL | SV=90 mL |
| ESV= 40 mL | CO= 7.2 L/Min |
| HR= 80 bpm | EF= 69.2% |

conditions such as congestive heart failure [11] [12], and LV hypertrophy [40] in patients.

## 2.3 Pressure Measurement Techniques in Small Lab Animals

Blood Pressure is one of the most important vital signals [41] in the study of the living body. Implantable blood pressure monitoring has been around since 1959 [42] and has advanced from invasive wired techniques [43] [44] to fully wireless solutions [13]. Blood pressure refers to the force exerted by circulating blood on the walls of blood vessels [45]. Two main techniques exist for measuring blood pressure in small laboratory animals: a catheter inserted into the LV [46] or using a tail cuff device [47].

Implantable pressure sensors inside catheters are MEMS (Microelectromechanical Systems) based sensors and require a surgical procedure to insert them into the LV, i.e., invasive. MEMS pressure sensors create an electrical voltage when the blood pressure changes. Catheter based pressure systems are very accurate however they allow for minimal overall movement of the test subject due to its direct connection with a larger measurement source. The surgical procedure can also cause possible complications such infection or trauma to the heart [48–52].

Tail cuffs are a non-invasive method of measuring blood pressure from small lab animals. This method places a small cuff around the animal's tail to measured the blood pressure, similar to a human blood pressure cuff. Although a non–invasive technique, the lab animal will still require some confinement which can cause non–ideal measurements. Unlike pressure sensors inside of catheters, tail cuffs cannot obtain continuous blood pressure measurements, only systolic blood pressure data [13].

More recently, pressure monitoring systems have evolved into wireless based solutions for long term implantable use. In [53] a pressure monitoring system is proposed which uses a passive telemetry link to send and receive power and data. Further advancement in miniaturization and packaging techniques has lead to the implantable system developed in [34]. Full implantable blood vessel cuff monitoring systems have also advanced throughout the years to current state–of–the -art methods such as the systems mentioned in [13] and [54].

## 2.4 Volume Measurement Techniques in Small Lab Animals

Left ventricle volume measurements in small laboratory animals is a difficult task to achieve due to the size restrictions and heart rate of these animals. For example, a small mouse heart's LV volume can be as small as 40 $\mu L$ and have a heart rate of 500-600 beats per min (bpm) with heart rates reaching as low as 300 bpm for an anesthetized mouse [55]. This requires measurement systems to be quite small, impacting the effectiveness and overall functionality of the measurements. Various different approaches on the measurement of instantaneous blood volume from small laboratory animals have been accomplished, these include using magnetic resonance imaging (MRI) [56] [57], echocardiography [57], CT volume measurements [58] and piezoelectric crystals [59]. These measurement techniques all require large equipment and laboratories to achieve their respective measurements and are sometimes very costly. They do however, provide highly accurate LV volume measurements when used. Catheter based methods have been developed [60] [61] to provide a low cost, yet accurate measurement solution

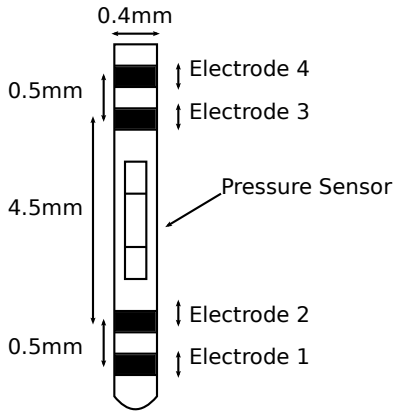


Figure 2.4: Example of the physical size of a implantable catheter, along with the electrode spacing for volume measurements and pressure sensor location.

for finding LV volume in small test subjects. Two techniques exist to measure LV blood volume using a catheter based system: conductance and admittance. These techniques provide methods for the accurate measurement of LV blood volume from small lab animals in a cost effective and accurate fashion.

### 2.4.1 Conductance

The classical method of measuring blood volume in a catheter based system is the conductance technique, which was first introduced by Baan et al. in the early 1980s [60]. In this method a tetra–polar catheter, Fig. 2.4, with two sets of rings located at the top and bottom of the catheter is placed inside the LV. The two outer electrodes inject a constant AC current into the blood to create an electric field within the LV and the two inner electrodes measure instantaneously the voltage created as the heart goes through its pump cycle. Conductance is calculated from the known excitation current and measured voltage using (2.1). It should be noted that the myocardium conductance varies over the cardiac cycle.

$$Conductance = \frac{Current\,(I)}{Voltage\,(V)} \tag{2.1}$$

The classical equation to convert the measured conductance to a LV volume is directly

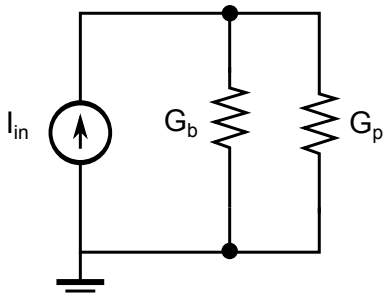


Figure 2.5: Conductance electrical heart model, where $I_{in}$ represents the injected current, $G_b$ blood conductance, $G_p$ muscle conductance.

found by using Baan's linear conductance to volume equation (2.2), where $\rho$ is the blood resistivity ($\Omega m$), L is the length between the voltage sensing electrodes (m), $\frac{1}{\alpha}$ is the stroke volume (SV) calibration factor (originally assumed to be 1), $G_{meas}$ is the instantaneous measured conductance (S), $G_p$ is the surrounding myocardial conductance (S), and $G_b$ is the blood conductance (S) [3]. Baan's equation makes the following assumptions: a) the electric field distribution is uniform throughout the cardiac cycle; b) the ventricular wall is insulated from the blood, i.e., the total measured conductance is due to the blood and not the heart muscle; c) the heart cavity has a cylindrical shape; and d) the catheter is stationary and always perfectly centred along the cylinder's axis.

$$\begin{aligned} Volume &= \frac{1}{\alpha}\rho L^2(G_{meas} - G_p) \\ &= \frac{1}{\alpha}\rho L^2 G_b \end{aligned} \tag{2.2}$$

The electrical model of the heart used in the conductance measurement method, Fig. 2.5, models the blood and muscle as single resistive components. A single conductance measurement includes information about both blood, $G_{meas}$ and myocardium muscle, $G_p$, leading to an over estimation of the LV blood volume. However, they are a combined value and cannot be separated without calibration [60]. One technique that is used to measure and calibrate out muscle conductance is Hypertonic saline bolus injection [62]. This technique is predominantly used in larger animals because the saline solution will significantly alter the blood resistivity and blood volume of smaller animals [61] causing Baan's equation to become invalid [60]. In

addition, other researchers have proposed combining the hypertonic saline technique with a simultaneous measurement at two different frequencies [63–65]. However, these calibration techniques are not time dependent, therefore not creating instantaneous calibration to the conductance measurement. The conductance value requires a time dependent calibration factor to take care of the change in LV volumes (i.e., changing the electric field based on heart cycle) during the cardiac cycle from end–diastolic to end–systolic. In summary, Baan's equation is a very simple conversion of conductance to volume, however, it is limited to measuring volume changes not absolute volumes because of its high error (overestimation of blood volume).

To correct for the effects from the nonuniform electric field on the conductance measurement, Wei et al. proposed a new improved equation denoted as Wei's equation (2.3) [66].

$$\begin{aligned} Volume &= \frac{\gamma}{\gamma - G_{meas} - G_p}\rho L^2(G_{meas} - G_p) \\ &= \frac{\gamma}{\gamma - G_b}\rho L^2(G_b) \end{aligned} \tag{2.3}$$

Where $\rho$ is the blood resistivity ($\Omega m$), L is the length between the voltage sensing electrodes (m), $\gamma$ is the field form factor, $G_{meas}$ is the instantaneous measured conductance (S), $G_p$ is the surrounding myocardial conductance (S), and $G_b$ is the blood conductance (S) [66]. The field form factor $\gamma$ is calculated by (2.4).

$$\begin{aligned} \gamma &= \frac{-b \pm \sqrt{b^2 - 4ac}}{2a} \\ where\ a &= SV - \rho L^2(G_{b-ED} - G_{b-ES}) \\ b &= -SV(G_{b-ED} + G_{b-ES}) \\ c &= SV \times G_{b-ED} \times G_{b-ES} \\ SV &= strokeVolume\ (L) \\ \rho &= blood\ resistivity\ (\Omega m) \\ L &= distance\ between\ sensing\ electrodes\ (m) \end{aligned} \tag{2.4}$$

The main benefit of Wei's equation compared to Baan's is the compensation for the non–

linear electric field throughout the LV. This is corrected using the field form factor or $\gamma$. Wei's equation does however, require an independent stroke volume (SV) measurement for the calculation of $\gamma$. For larger subjects, Wei's equation can reduce the overestimation error to 10% compared to using the original Baan's equation [66]. In addition, this equation still requires parallel conductance removal through Hypertonic saline techniques. Therefore, a new technique was created to separate blood volume from the surrounding muscle (myocardium) to calculate a more accurate LV volume measurement using Wei's equation.

### 2.4.2 Admittance

Porterfield et. al [67] proposed a new admittance based technique in the late 2000s, where the electrical and permittivity properties of the murine myocardium [68] are exploited to remove the myocardium conductance ($G_p$) component from the overall measured signal. In addition, this technique includes the effects of the parallel myocardium capacitance ($C_m$), where the original conductance method did not. This is described in the admittance equation (2.5), where the myocardium conductance and capacitance vary over the cardiac cycle.

$$\begin{aligned} Y_{meas} &= Y_{blood} + Y_{muscle} \\ &= G_b + G_p + j\omega C_m \end{aligned} \tag{2.5}$$

The motivation for measuring admittance (complex conductance) rather than conductance is that by using excitation frequencies of approximately 20 kHz, blood is purely resistive and the myocardium has both resistive and capacitive electrical properties [68] [69–71]. Therefore, an updated electrical model of the heart is realized, Fig. 2.6, where $G_b$ represents the conductance of the blood, $G_p$ myocardium conductance, and $C_m$ myocardium capacitance. Using an excitation frequency of $\sim$20 $kHz$ allows for the separation of the admittance of the myocardium from the combined measured admittance using electric field theory [67].

For an electric field E in homogenous tissue (left ventricle heart tissue), the conductance and capacitance between the inner electrodes are given by (2.6) and (2.7) [67].

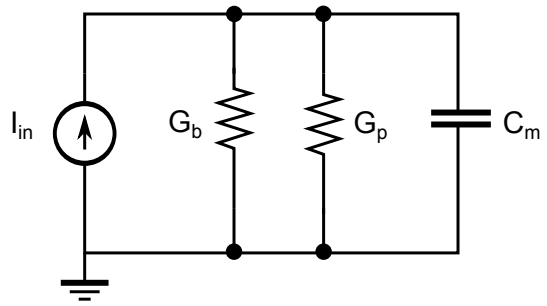


Figure 2.6: Admittance electrical heart model, where $I_{in}$ represents the injected current, $G_b$ blood conductance, $G_p$ muscle conductance and $C_m$ as the capacitive component of the muscle.

$$G = \frac{I}{V} = \frac{\iint \sigma_m E \cdot dS}{-\int E \cdot dL} = \sigma_m F \tag{2.6}$$

$$C = \frac{Q}{V} = \frac{\iint \varepsilon_m E \cdot dS}{-\int E \cdot dL} = \varepsilon_m F \tag{2.7}$$

Where, G is conductance (S), I is current (A), V is voltage potential (V), $\sigma_m$ is the electrical conductivity of the myocardium ($S/m$), $\varepsilon_m$ is the electric permittivity (F/m), F is the field geometry factor (m), C is capacitance (F), and Q is charge (C). The integration is from one inner electrode to the other along a vector pathway (L) and the surface (S). The measured conductance and capacitance of the electric field are related by (2.8), where the ratio of $\frac{\sigma_m}{\varepsilon_m}$ is found using a surface probe measurement before the main experimental procedure. The derivation and process on measuring and calculating these parameters is detailed in [68].

$$G_p = C_m \frac{\sigma_m}{\varepsilon_m} \tag{2.8}$$

During an experimental procedure, only the magnitude and phase of the admittance signal will be measured (i.e., $Y_{meas} = |Y_{meas}|\angle\theta$). This is conducted using the same catheter, Fig 2.4, as the conductance method. Therefore, using these two parameters the values of $G_b$, $G_p$, and $C_m$ can be calculated. Recall, that $Y_{meas}$ is equal to (2.5) and that blood is purely resistive and the myocardium has both resistive and capacitive electrical properties when using an excitation

frequency of 20 $kHz$. With this knowledge, one can calculate the instantaneous values of $C_m$, $G_p$, and finally $G_b$ using equations (2.8), (2.9), and (2.10), respectively.

$$C_m = \frac{|Y_{meas}| \sin(\theta)}{2\pi f} \tag{2.9}$$

$$G_b = |Y_{meas}| \cos(\theta) - G_p \tag{2.10}$$

These three equations allow the parallel conductance (myocardium conductance) to be dynamically calculated based on the frequency dependent value of $C_m$. This eliminates the need for hypertonic saline injection to calculate $G_p$, which is extremely beneficial for testing in small laboratory animals. Finally, with the complex admittance calculated, Wei's equation (2.3) can be used to calculate accurate volumes of the LV [68] [14].

State–of–the–art LV volume systems use this technique to calculate absolute volumes, however, test animals must still be tethered to the catheter measuring device causing non-ideal blood pressure and volume data. Hence, there is a significant need for wireless miniaturized telemetry systems to retrieve LV pressure and volume from a small living animal

## 2.5 Lock–In Amplifier Background Theory

Lock–in amplifiers are used to measure low voltage AC signals ($\mu$V to nV) within noisy environments. These noise signals can be many times larger than the signal of interest and a lock–in amplifier is still able to extract such a signal [72]. Recall, standard AC voltage measurements measure all voltages at the measurement input, including all noise signals as well as the signal of interest. This can cause signals of interest to be lost or overwhelmed with noise. Lock–in amplifiers are different from these AC voltage measurements because not only is a excitation signal provided to the experiment but a reference signal is also provided [73]. This signal must be phase and frequency locked with the original excitation signal for the amplifier to work cor-

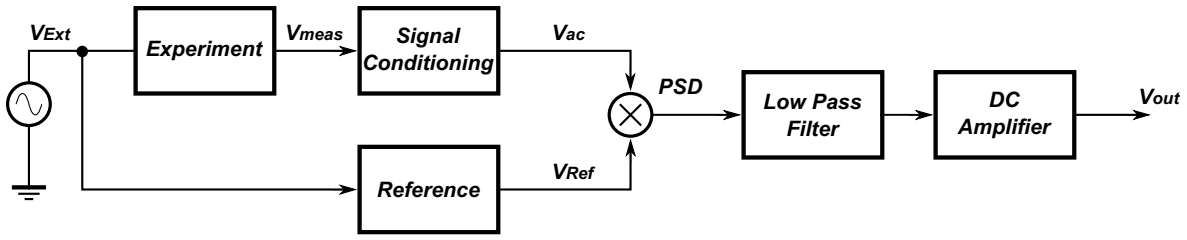


Figure 2.7: Block diagram of a Lock–In Amplifier.

rectly. The lock–in amplifier uses the reference signal to locate the measured signal of interest within the noisy environment, while disregarding all signals that are not of the same frequency as the reference signal. This technique is known as phase sensitive detection [74]. This is the main reason that a lock–in amplifier can measure very small experimental voltage amplitudes in an environment that contains noise signals much greater. Lock–in amplifiers are used in many different applications from gas monitors [75] to wireless embedded applications [76–78].

The basic lock–in amplifier structure, Fig. 2.7, contains seven main components: excitation source, experimental system, signal conditioning, reference generation, phase sensitive detector (PSD), low pass filter (LPF), and DC amplifier [73].

### Time Domain Analysis

The excitation signal $V_{ext}(t) = V_o \cos(2\pi f_o t)$ is fed into the test system to initiate the measurement. The measured signal is first directed through the signal conditioning block. Here, the measured waveform is amplified and filtered to remove unwanted frequencies above and below the frequency of interest, $f_o$. The output of the signal conditioning block is (2.11), where $G_{ac}$ is the gain of the signal conditioning block, $V_o$ is the amplitude of the signal of interest, $f_o$ is the excitation frequency, and $\theta_s$ is that possible phase shift of the signal. This represents one input to the PSD.

$$V_{ac}(t) = G_{ac} V_o \cos(2\pi f_0 + \theta_s) \tag{2.11}$$

The phase sensitive detector is a specific type of frequency mixer (multiplier). A frequency

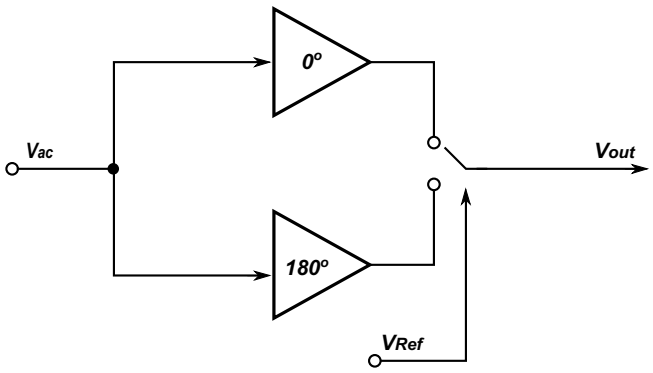


Figure 2.8: Ideal mixer implementation.

mixer in the most basic sense multiplies two signals $V_1(t)$ and $V_2(t)$ to form a new signal. As stated previously, one input is (2.11) and the reference voltage, $V_{ref}(t)$, is the other. A mixer can be implemented in many forms including transistors, diodes, or any non linear device. However, in a simple implementation, the mixing circuit can be described by Fig. 2.8 [76]. Here, the measured signal, (2.11), is split into the in–phase 0° and the anti–phase 180° components, where a switch controls the output. This switch is controlled by the reference signal, $V_{ref}(t)$. This configuration offers the widest dynamic range to maximize the signal recovery [74].

The reference signal is chosen to be a square wave with a gain of 1 to control the switch in the PSD. In different mixer circuit configurations the reference signal can be a general sinusoid. The reference signal is phase and frequency locked to the original excitation frequency $V_{ext}(t)$ and is represented by (2.12).

$$V_{ref}(t) = \frac{4}{\pi}[\cos(2\pi f_o t + \theta_R) - \frac{1}{3}\cos 3(2\pi f_o t + \theta_R) + \frac{1}{5}\cos 5(2\pi f_o t + \theta_R)\ldots] \tag{2.12}$$

When two signals of frequencies $f_1$ and $f_2$ are multiplied together, two additional signals are created with one equal to $f_1 + f_2$ and another equal to $f_1 - f_2$, along with harmonics. Therefore if (2.11) and (2.12) are multiplied (2.13) is created, where $\omega_R = 2\pi f_{ref}$, $\omega_S = 2\pi f_{meas}$ and $\theta_R, \theta_S$ represent the phase shifts of the respective signals.

$$\begin{aligned} V_{PSD}(t) = \frac{2\sqrt{2}V_o G_{ac}}{\pi}[&\cos(\omega_R t \pm \omega_S + \theta_R \pm \theta_S) \\ &- \frac{1}{3}\cos(3\omega_R t \pm \omega_S + 3\theta_R \pm \theta_S) \\ &+ \frac{1}{5}\cos(5\omega_R t \pm \omega_S + 5\theta_R \pm \theta_S)\ldots] \end{aligned} \tag{2.13}$$

If the assumption that the measured signal and reference signal are frequency locked ( i.e., $\omega_R t = \omega_S t$) is made and that the subsequent low pass filter cuts off well below the reference frequency ( i.e., removes upper harmonics) then (2.13) reduces to (2.14).

$$V_{PSD}(t) = \frac{2\sqrt{2}V_o G_{ac} G_{lpf}}{\pi}\cos(\theta_R - \theta_S) \tag{2.14}$$

Equation (2.14) is directly proportional to the amplitude of the signal of interest $V_o$ along with a phase difference of $\theta_R - \theta_S$. However, if the experiment does not introduce a phase shift, then this component can be ignored. In addition, the LPF block acts as an integrator to remove any additional noise created at the output of the mixing circuit. Further DC gain can be obtained through a DC amplifier. All factors are known except for $V_o$, therefore, the measured signal can be extracted from the noisy environment using the final DC output, (2.15).

$$V_{PSD} = \frac{2\sqrt{2}V_o G_{ac} G_{lpf} G_{DC}}{\pi} \tag{2.15}$$

**Magnitude and Phase Measurements**

The previous lock–in amplifier design will only detect the magnitude of the measured signal, however even if $\theta_R - \theta_S \neq 0^\circ$ this design cannot measure it. To measure the phase shift created by the experimental process, two phase sensitive detectors are required [74] [72], Fig. 2.9.

The second PSD requires a reference signal shifted by 90° from the original excitation signal. This allows quadrature signals to be measured or in–phase (I) and out of phase (Q) components. The second PSD's output is (2.16).

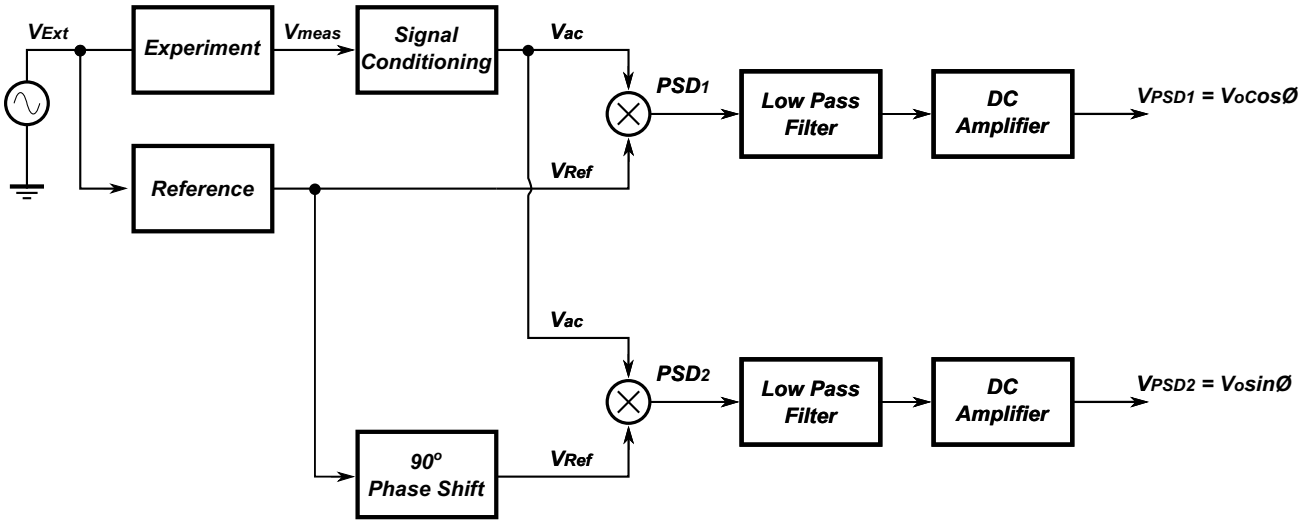


Figure 2.9: Dual Lock–In Amplifier block diagram.

$$V_{PSD2}(t) = \frac{2\sqrt{2}V_o G_{ac} G_{lpf} G_{DC}}{\pi} \sin(\theta_R - \theta_S) \tag{2.16}$$

By using equation (2.14) and (2.16) the magnitude and phase of the measured signal can be calculated using simple trigonometry. The magnitude is calculated by (2.17) and the phase is calculated by (2.18).

$$Magnitude = \sqrt{(V_{PSD1})^2 + (V_{PSD2})^2} \tag{2.17}$$

$$Phase = \tan^{-1}\left(\frac{V_{PSD2}}{V_{PSD1}}\right) \tag{2.18}$$

Using this technique the magnitude and phase of a specific signal can be measured inside a noisy environment.

## 2.6 Summary

In this chapter, an introductory literature review on implantable systems with their various application areas is presented. In addition, the critical publications relevant to this research are

discussed. A brief introduction to pressure–volume loops and some of the cardiac parameters that can be calculated are examined. Furthermore, pressure–volume measurement methods in murine animals are explored in detail. Additional circuit theories are provided for background context into the implementation of the designed wireless telemetry system.

# Chapter 3

# Wireless Telemetry System Architecture

A wireless telemetry system is designed that is suited for measuring blood pressure and volume data from a small laboratory subjects. The system captures, processes and transmits this data wirelessly to an end base station for further processing. The main design requirements for this system are: it must be small in size and have low power consumption. These two criteria allow a system such as this, to be implanted for a long period of time while operating off of battery power. The overall system is divided into two units: external and internal, Fig. 3.1.

The external unit includes both a future power delivery section and an end device. The power delivery section contains a larger transmitting coil, which is connected to a wired power source, and is designed to allow for maximum power transfer to the smaller implant coil. The transmitting and receiving power coils are designed in [79]. The second sub–block is the end device, which can refer to a computer or a more application specific embedded system. The end device is connected wirelessly to the internal unit through a wireless data–link.

The implantable internal unit is a small application specific system, designed to capture biosensor data using a custom interface board and communicate to the end device for further processing. The implantable unit contains four main sub–blocks: power–harvesting, processing, RF transceiver, and an application specific interface block. Each block is discussed in detail in the following sections.

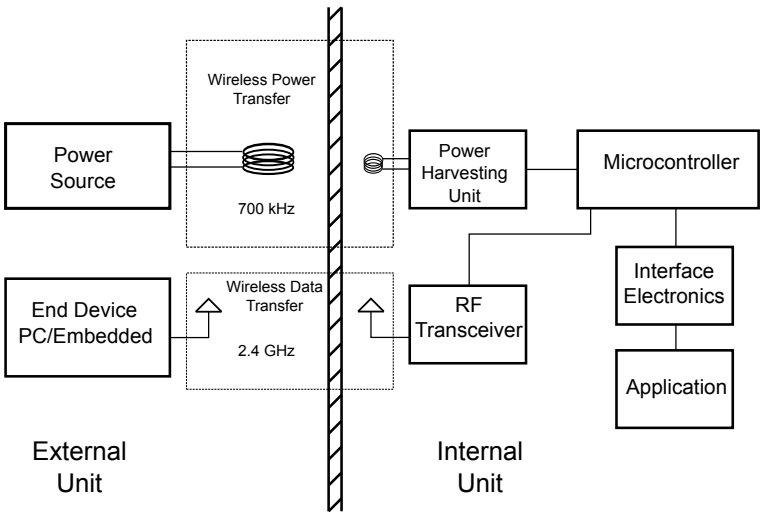


Figure 3.1: Block diagram of the proposed wireless telemetry system.

The main focus for this thesis is the development of the internal implant system. The power delivery section is not discussed here and is being developed concurrently in another project. It is assumed that the implant will be designed around a battery based system, Section 3.1 provides details into this. Two experimental prototypes are created, denoted as Phase 1 and Phase 2 prototypes. These prototypes are discussed in results chapter, Section Section 4.2.1.

The wireless implantable telemetry system architecture is based on the overall structure outlined in Fig. 3.1. The specific design of the internal unit is achieved by creating four main modules: Power Module, Microcontroller Module (Processing Module), RF Module (Transceiver Module), and Interface Module, Fig. 3.2. All these modules communicate with each other through a commutation bus. Each module has access to this bus, and is described in more detail in Section 3.4. There is also an auxiliary module for testing and programming indicated as the Development module, with more information found in Section 4.2.1. The following sections describe the design process for each module culminating in the design of the two prototypes.

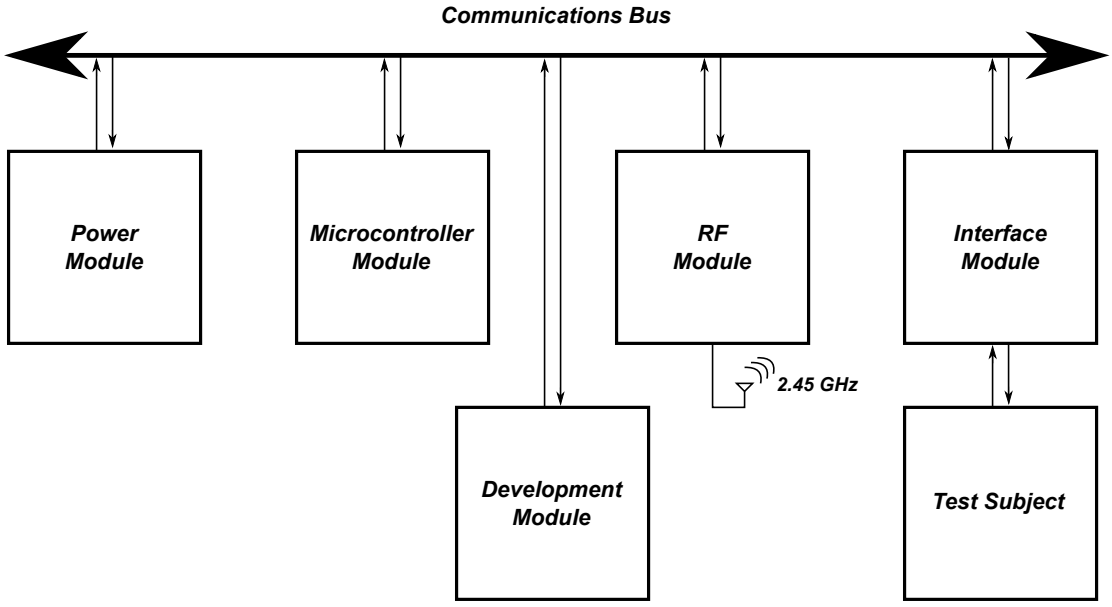


Figure 3.2: Block diagram of internal wireless implantable telemetry system.

## 3.1 Power Module

The power module contains all electronics to provide power to the whole system. The main components in the power module are: a battery, low–dropout regulator, supervisor device, and an analog switch for the interface module, Fig. 3.3. The power module provides 3.6 V DC to the system through the main bus structure. All modules have access directly to the power module, with each module's ground plane connected directly to the batteries ground.

### 3.1.1 Battery

A battery for an implantable system should be small in size but have a large capacity. It also should be rechargeable in order to extend the lifetime of the system. Lithium-ion polymer batteries are chosen for the batteries for this system because of their high capacity and small size characteristics, as well as being rechargeable. Two batteries are chosen for this project, America Kokam SLPB 241019 and Full River 501213, for Phase 1 and Phase 2, respectively.

In the first phase of the project, the battery has a 25 *mAh* capacity with a nominal voltage

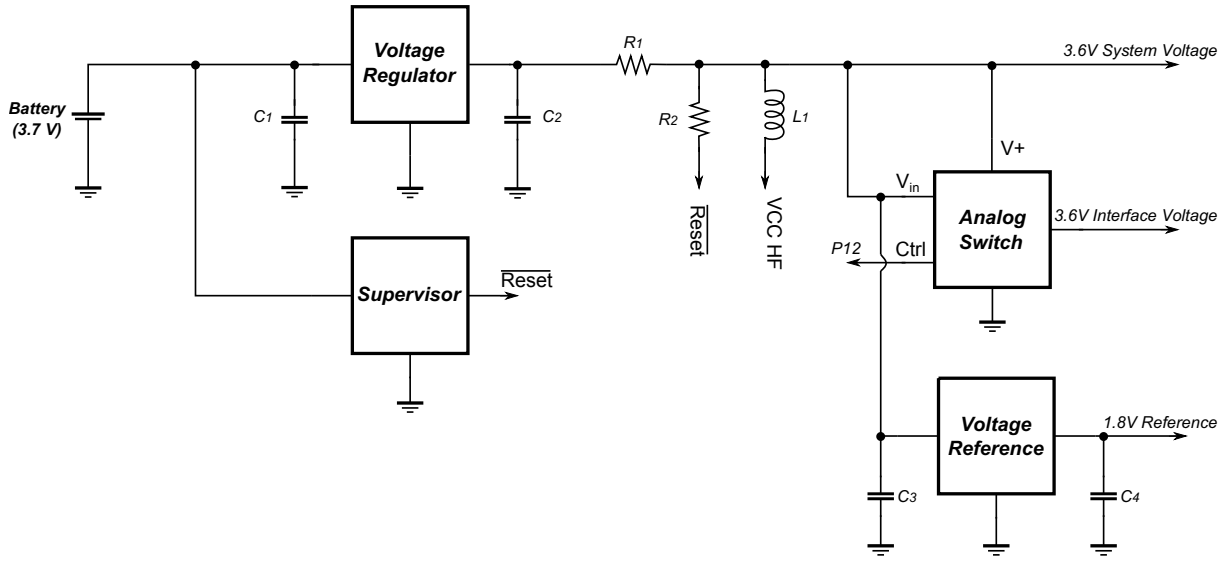


Figure 3.3: Full schematic of the Power Module.

of 3.7 V and a charge condition of 1C. The overall dimensions are 25.35 mm x 10.8 mm x 2.4 mm (L x W x H), Fig. 3.4(a).

The second battery that is used has a 40 *mAh* capacity with a nominal voltage of 3.7V and a charge condition of 1C. The overall dimensions are 15 mm x 11.0 mm x 5 mm, Fig. 3.4(b). The overall area is reduced from 273.78 $mm^2$ to 195 $mm^2$ or a reduction of 27.7% in area compared to the phase 1 battery. However, the volume of the second battery increases to 975 $mm^3$ from 657.07 $mm^3$. This increase is justified by the increase in charge capacity. The overall area is the most import design constraint for the battery as this directly dictates the system size. Each battery is recharged with a Li–Poly USB battery charger.

### 3.1.2 Low Dropout Regulator

A voltage regulator is used to regulate the input voltage from the battery to some select DC voltage, in this case, the battery voltage is 3.7 V and the main system voltage is 3.6 V. The regulator should have a low consumption current (Iq), very low dropout (LDO), and have a high power supply rejection ratio (PSRR).

Two LDO regulators are chosen for this project, one for each phase. The first phase the TI

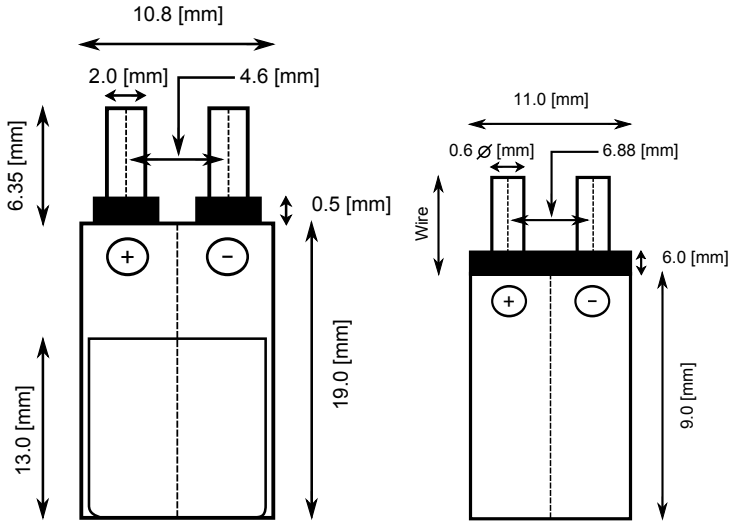


(a) Phase 1 Battery (b) Phase 2 Battery

Figure 3.4: Dimensions of the batteries used in each prototype, 3.4(a) Phase 1 and 3.4(b) Phase 2.

TPS77301DGK, Fig. 3.5, is chosen for LDO regulator. This is an adjustable voltage regulator, where the output can be varied based on a set of two resistors. The TPS77301DGK has a typical Iq current of 92 $\mu A$, with a 200 $mV$ dropout for a 3.3 V output and a PSRR of 55 $dB$. The main advantage of this regulator is the adjustable nature of the output voltage. This allows for flexible system voltages if needed. The output voltage is calculated by (3.1).

$$Vout = V_{ref} * (1 + \frac{R1}{R2}) \tag{3.1}$$

where $V_{ref}$ is 1.1834 V from the internal Bandgap reference. R1 and R2 are chosen for approximately 50 $\mu A$. The resistor values are chosen to output a fixed 3.6 V, where R1 was 68 $k\Omega$ and R2 was 33 $k\Omega$. This regulator provides a stable 3.6V reference for the main system.

The voltage regulator that is used in phase 2 of the project is the TI TLV70036. This regulator has a fixed 3.6V output rather than an adjustable output, with a typical Iq of 31$\mu A$, 175 $mV$ dropout for a 2.35 V output and a PSRR of 68 $dB$. The lower current consumption, higher PSRR and less external components are the main reasons for adopting the new LDO regulator in the second revision of the system. As a result of having a fixed voltage output, no

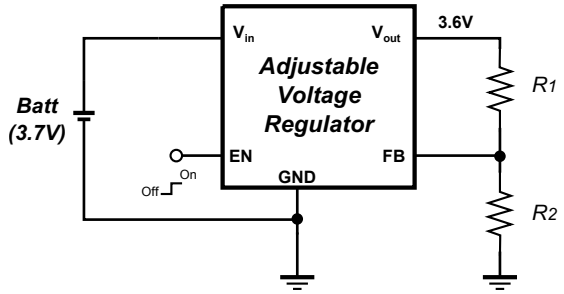


Figure 3.5: Adjustable voltage regulator with feedback voltage divider.

external resistors are needed to create the regulated output voltage. This reduces the component count by two resistors.

### 3.1.3 Supervisor Device

A supervisor integrated circuit (IC) is used in the power module to provide circuit initialization and voltage protection to the microcontroller and battery. The supervisor circuit is connected to the microcontroller's reset pin where an internal delay is started to prevent the microcontroller from powering until the line voltage is stable and above a specific voltage. If the line voltage or in our system, the output of the battery drops below the specific voltage the supervisor chip will cause the microcontroller to reset and prevent damage to the microcontroller. The supervisor chip used in both systems is the TI TPS3838 with a typical power consumption of 220 $nA$ and a supervisor (threshold) voltage of 2.93 V.

### 3.1.4 Voltage Reference

The need for a voltage reference in the designed wireless telemetry system is to provide a virtual ground to the analog circuitry on the interface modules. A virtual ground is needed to allow for full voltage swing to occur in the analog signal chain while using single ended devices. As described in Section 3.1, the telemetry system operates off of a single ended 3.6 V power supply, if full voltage swing is needed in any module, a virtual ground of $VDD/2$ =

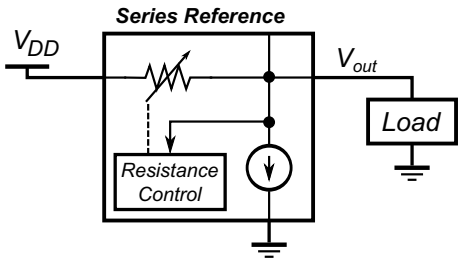


Figure 3.6: Examples of series voltage reference.

$3.6/2 = 1.8V$ is required. A series voltage reference was chosen for this project due to its highly accurate regulated voltage output.

The Maxim MAX6018 1.8 V series voltage reference is chosen to achieve this function. The MAX6018 has an output voltage of 1.8 V with a min voltage of 1.7964 V to a maximum output of 1.8036 V. It also has a supply current of 3 $\mu A$ with a wide input range. The high precision, low power, and minimal component packaging of the MAX6018 were the main reasons for choosing this series voltage reference.

### 3.1.5 Analog Switch for Interface Module

The Interface modules operate using the same DC 3.6 V power supply as the rest of the system, however, the voltage supplied to these modules should be switched off whenever not in use. Therefore, the main power rail is split to form a separate interface module voltage rail (Interface Voltage). An analog Single Pole Single Throw (SPST) is used to perform this purpose. A SPST switch generally has five terminals: power, ground, control, $V_{in}$, $V_{out}$, Fig. 3.7. In this system, the MAXIM MAX4715 is used to provide this function. The MAX4715 contains the five terminals outlined above with 0.4 Ω max of $R_{ON}$ resistance at a 3 V power supply and 0.04 $\mu A$ of current consumption. The main function of this switch is to control when the interface module power is on or off, allowing the overall power consumption to be reduced. The control line for the SPST switch is P12 (GPIO) from the microcontroller. If P12 is low then the output voltage to the interface modules is off and when P12 is high the output voltage to the interface modules is on. By using this logic, the interface module's power supply can be controlled

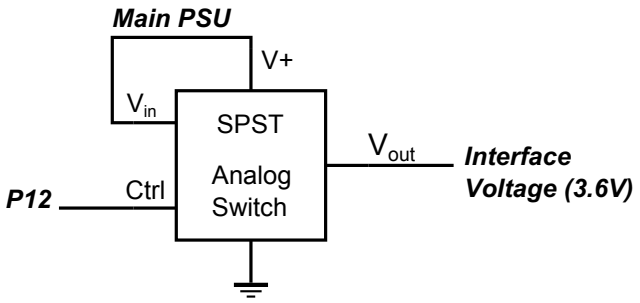


Figure 3.7: Interface Module power switch. P12 controls 3.6 V to Interface module.

by sending digital I/O signals from the microcontroller down the bus to the power module to control the operation of the switch.

## 3.2 Microcontroller Module

The Microcontroller module is the main communications hub between the RF electronics, interface electronics and power electronics, Fig. 3.8. The main duties of this module are to capture the incoming analog data from the interface module, digitize it and then process the data for RF transfer. The transfer of digital data to the RF radio is transferred via the Serial Peripheral Interface (SPI) bus, discussed in more detail in Section 3.3.2. The analog data is transferred down to the microcontroller module through the communication bus and connected directly to the microcontroller's input pins. This data is then digitized by a 10 bit ADC, processed and sent to the CC2500 for RF transfer. The microcontroller module is programmed through a external programming connector that is disconnected after each upload.

### 3.2.1 MSP430

Various microcontrollers exist that perform basic functions such as general digital input and output (GPIO), analog input and communication protocols. These microcontrollers come from a wide range of manufactures such as Atmel, Texas Instruments, PIC, etc. The microcontroller chosen for this project is the MSP430 from Texas Instruments (TI). It is chosen for its

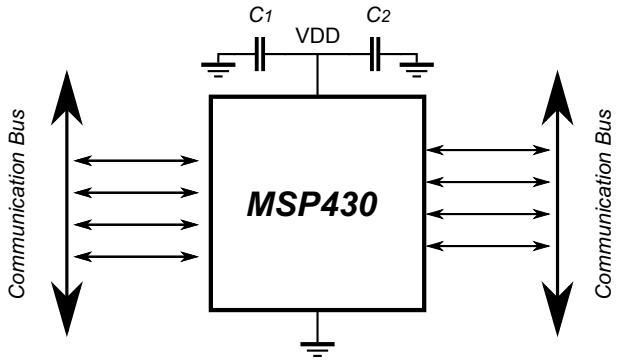


Figure 3.8: Microcontroller Module schematic. Input and output communication through communication bus.

wide availability, low cost, and low power consumption. The MSP430 comes in may different versions, each with different features, the MSP430F2274 is chosen for this project. The MSP430F2274 contains a 12 channel 10-bit SAR ADC, SPI communication bus, a 16 $MHz$ internal clock and many more features within a 40 pin package [80]. All pins of the microcontroller are connected to the main communication bus, allowing each module to communicate directly with the microcontroller. The internal clocking, ADC and power management modules are three of the main MSP430 features that are utilized in this project.

### Clocking MSP430

The MSP430F2274 contains a clock module which includes three main clock sources, LFXT1CK, DCOCLK, VLOCLK. Each clock source can be used to drive any of the three main clock signals: ACLK, MCLK, SMCLK. The low–frequency oscillator is the clock source for external crystals and resonators, with a frequency range of 400 $kHz$ to 16 $MHz$. The internal Digitally Controlled Oscillator (DCO) is the main clock inside the MSP430, with a maximum frequency of 16 $MHz$ and is able to be divided internally to create sub frequencies. Finally the VLOCLK is an internal low–power, low–frequency oscillator in the frequency range of 12 $kHz$. Each of these clock sources are used to route the clock signals to the MSP430's internal architecture. The main clock signal of the MSP430 is MCLK, which is used by the CPU and the supporting architecture. The remaining clock signals, ACLK (Auxiliary Clock), SMCLK (Sub–Main

Clock), are used to control individual peripheral modules.

In the designed telemetry system, the MSP430F2274 is clocked using the internal clock rather than an external crystal. An external crystal is not used to reduce area and component count of the system. The MCLK is sourced from the DCO using a internal frequency of 1 $MHz$ and ACLK, SMCLK are sourced by the VLOCLK. A lower clock frequency is used in the DCO instead of the higher maximum frequency of 16 $MHz$ to conserve power during active modes of the MSP430.

**Analog to Digital Conversion in the MSP430**

The analog to digital (ADC) conversion module is an essential module for the operation of the wireless telemetry system. The ADC is used to convert the analog sensor data to usable digital data. The MSP430 contains a 10–bit successive approximation ADC with eight external inputs. The voltage reference that is used for comparison can be an external or internal voltage reference. A internal 1.5V or 2.5V Bandgap reference is used for the internal voltage reference. Any clock in the MSP430 can be used to control the conversion timing.

The main formula used in the conversion of the analog signal to the 10–bit digital signal is (3.2) [81], where $V_{in}$ represents the analog input voltage, $V_{R+}$ indicates the positive voltage reference used, and $V_{R-}$ indicates the negative voltage reference used, in most cases 0 V.

$$N_{ADC} = 1023 * \frac{V_{in} - V_{R-}}{V_{R+} - V_{R-}} \tag{3.2}$$

In the proposed system, 4–6 analog inputs are used depending on the interface electronics active, with each using the internal voltage reference. The internal voltage reference is used rather than the external voltage reference as less external components are needed, allowing the reduction of the area of the overall system. The internal ADC oscillator is used to clock the conversion of the analog to digital signal.

**Power Management**

One of the key features of the MSP430 is that it's designed for low–power applications, which makes it an ideal choice for the proposed implantable system. The MSP430 has six different operating modes designed specifically for low power operation, Active, LPM 0 – 4. These modes range from 270 $\mu A$ at 1 $MHz$, 2.2 V supply to 0.7 $\mu A$ in LPM4.

The main difference between each mode is the number of clocks in the clocking module that are active. Where in the active mode, all clocks and the CPU are active, while at the other extreme in LPM4, all clocks and the CPU are disabled. Low Power Mode (LPM) 0 to LPM 3 have various clocks on or off. Ideally in a implantable system, the MSP430 would remain in LPM4 for most of the time, only to be placed in one of the other low power modes when processing is needed, this is done using an interrupt. By using these different operating modes, the power consumption of the wireless system can be greatly reduced.

### 3.2.2 Microcontroller Software

The MSP430 was programmed using IAR Embedded Workbench for MSP430 IDE. MSP430 assembly and C are the main programming languages used in this implantable telemetry system. For the preliminary tests of the MSP430, assembly language is used to test each register and specific functions while C language is used for higher level programming. The main telemetry system programming is a separate research project and is not discussed in this thesis. For the purposes of functionality, C and assembly level code is written to enable wireless communication and basic processing.

The MPS430 is programmed using a 6 pin custom connector which contains the pins: Power, Ground, TX, RX, RST, and TEST. The power and ground pins are connected to the USB power and ground to supply power to the microcontroller while programming. The TX and RX pins are the data lines used in communication between the software and the microcontroller. Finally, the RST and TEST pins and used by IAR Embedded Workbench for resetting the device and testing the microcontroller.

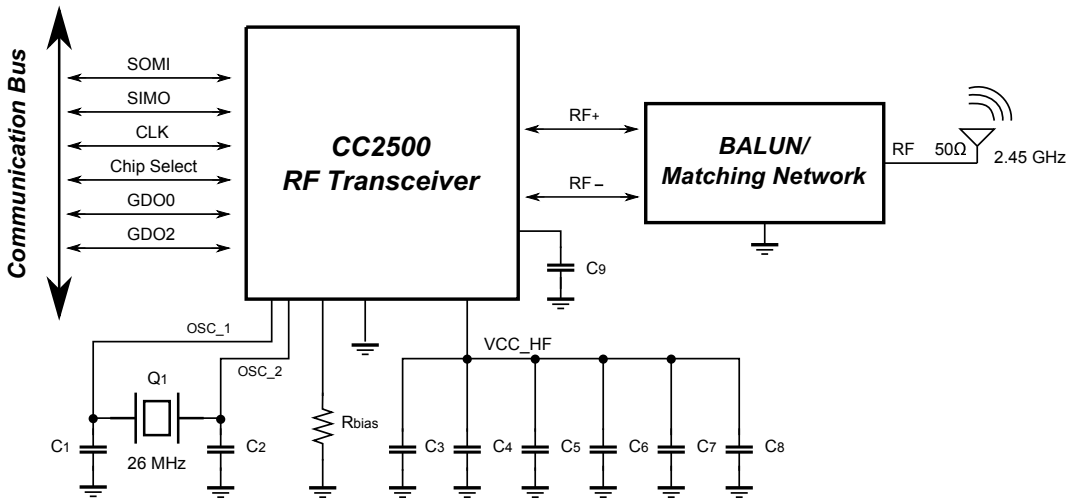


Figure 3.9: Radio Module schematic with SPI communication through the bus. Matching network and RF antenna are also included.

## 3.3 Radio Module

The radio module inside the telemetry system enables wireless communication to an end device and contains four major components: RF transceiver, matching network, antenna, and a clock source, Fig. 3.9.

This module directly interfaces with the Microcontroller Module through the communication bus, with no other modules interfacing with it. The radio module transmits its data wirelessly via a RF antenna with a specific RF protocol. Different wireless protocols exist to transmit data wireless such as bluetooth, WIFI, non-standard 2.4 $GHz$, other RF proprietary RF frequencies, etc. A non–standard TI 2.4 $GHz$ protocol is chosen for its low–power features and its high compatibility with other Texas Instruments components.

The RF transceiver must interface with an external antenna that will allow it to transmit to a base station. Generally, this must be done through a matching network, matching the output impedance of the transceiver to the 50 Ω antenna, discussed in Section 4.2

Along with a matching network and antenna, the RF transceiver must also contain a clock to correctly time the communication between the RF transceiver and the microcontroller for sending data, a 26 $MHz$ quartz crystal is used to achieve this function.

### 3.3.1 CC2500

The Texas Instruments CC2500 is the transceiver used in the proposed implantable wireless telemetry system. The CC2500 is a low–power 2.4 $GHz$ wireless transceiver and is designed for the Industrial, Scientific and Medical (ISM) band along with the Short Range Device (SRD) band, 2400 $MHz$ – 2483.5 $MHz$. The CC2500 has a programmable output power up to +1 $dBm$, with a maximum data rate of 500 kBaud. The CC2500 acts as a receiver as well, with a sensitivity of -104$dBm$.

The CC2500 is chosen for the RF module for its low current consumption (400$nA$ in sleep) and minimal external components required. The CC2500 is programmed by the MSP430 directly through the SPI bus discussed in Section 3.3.2. The CC2500 is clocked using an external 26 $MHz$ crystal, with two 27 $pF$ capacitors connected directly to the IC. Additional external components are needed for decoupling capacitors, bias resistors and matching network circuitry.

The CC2500 interfaces with a 50 Ω antenna through a balun and matching network. The RF input and output of the CC2500 is balanced with an impedance of $Z_{out} = 80 + j74\ \Omega$. A balance to unbalanced (balun) network is generally created from passive components to convert the balanced signal, i.e., differential in/out to unbalanced, i.e., single ended 50 Ω antenna. This intermediate impedance is then matched to the 50 Ω antenna for maximum power transfer. Two balun and matching network designs are implemented in a respective prototype, discussed in detail in Section 4.2.

### 3.3.2 Communication Between Microcontroller and CC2500

The digital communication between the microcontroller (MSP430) and the transceiver (CC2500) is achieved through the SPI bus. Six wired connections make up this bus, four for the main SPI link and two for interrupts, Fig. 3.10. The four SPI wired connections, SPI SIMO, SPI SOMI, SPI CLK, and SPI Chip Select send and receive data from the CC2500. SPI Chip select is used to enable and disable the communications between the two devices. This pin is essential in the

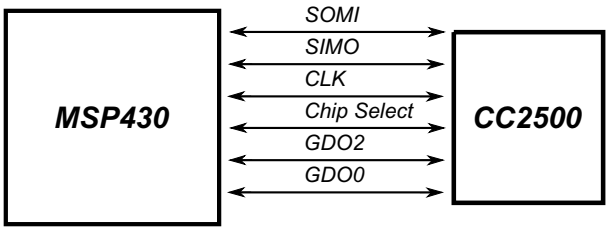


Figure 3.10: SPI digital communication link between MSP430 and CC2500.

design as the SPI bus is utilized in other ares of the system, i.e. digital pressure section, hence allowing the SPI bus to be multiplexed. The timing for the SPI communication is preformed by the SPI CLK pin. This timing is synchronized between both the master and salve devices using this pin automatically. Finally, the two main data lines, SPI SIMO, SPI SOMI, represent the master to slave communication and the slave to master communication, respectively. In this case, the MSP430 acts as the master and the CC2500 as the salve device. However, the CC2500 does not communicate back to the MSP430 through the SPI SOMI pin, it can only receive instructions.

The other two connections, are used for interrupts to allow the CC2500 to trigger the microcontroller to wake up from low–power state when a packet is received. The CC2500 refers to these two pins as GDO0 and GDO2. In the designed telemetry system they are connected to GPIO pins 2 and 3 on the MSP430. By using these two interrupts, the MSP430 is able to go in low–power state while the CC2500 remains in receive mode.

The SPI bus is directly integrated in the main communication bus structure. By doing this, any module can access the SPI bus to communicate digitally with the microcontroller module, only an additional chip select pin is needed to determine which device to communicate with.

### 3.3.3 RF Parameters

The CC2500 includes 47 programmable registers that contain the parameters used in RF transmission. Examples of these registers include configuration for modulation type, frequency, output power, packet size, etc. These registers are all programmed through the SPI bus from the

MSP430. Upon power up, these parameters are copied to the registers from the MSP430, as the CC2500 does not store them after loss of power. The CC2500 is configured to use Frequency-Shift-Keying (FSK) Modulation and an operating frequency of 2.45 $GHz$. These parameters are determined using the TI SimplicTI drivers or manually if optimization is needed.

## 3.4 Communications Bus

The telemetry system's main form of digital and analog communication between each module and the outside world is achieved through the use of a communications bus. When designing the bus structure multiple signals are required and must be taken into consideration. These include: power signals (System Voltage, Interface Voltage, HF voltage), ground signals, I/O, programming pins, charging pins, etc. With the physical design in mind, the communication bus is split across two vertical connectors. There are two different communication bus pinouts used in this telemetry system, one for each prototype version. Refer to Section 4.2.1 for physical connector information.

### 3.4.1 Phase 1 – Communication Bus

In the first phase of the design, a total of 32 pins split across two connectors with 16 pins each are used. In this architecture, 5 pins for power (1 System Voltage, 4 high frequency (HF) Voltage), 12 pins are used for ground, 6 SPI pins, 4 for programming (plus VCC and ground), and 5 I/O pins, Table 3.1. Each module has access to any of these pins, if needed.

The power and ground signals all originate from the power module. The power module creates and distributes these signals from the battery to the communications bus. Every board has access to multiple grounds, which provide a low impedance path back to the battery. There are two main power signals in this version of the communication bus: 3.6 V Rail for System Voltage and 3.6 V Rail for high frequency devices. The main 3.6 V rail is connected to the microcontroller and interface modules, and the 3.6 V HF is only connected to the RF module.

Table 3.1: Communication Bus in Phase 1 prototype

| **Pin** | **Function** |
|---|---|
| System Voltage | 3.6 Volt Rail for System Voltage – From Power Module |
| HF Voltage | 3.6 Volt Rail for RF Module – From Power Module |
| Ground | Ground – Connected Directly to the Battery |
| UCB0STE | Chip Select for SPI Bus |
| UCB0SIMO | Slave In, Master Out for SPI Bus |
| UCB0SOMI | Slave Out, Master In for SPI Bus |
| UCB0CLK | SPI Clock |
| GDO0 | Interrupt for communication between CC2500 and MSP430 |
| GDO2 | Interrupt for communication between CC2500 and MSP430 |
| TEST | Test signal using in programming MSP430 |
| RST | Reset signal to MSP430 |
| TXD0 | Transmit Pin for Programming MSP430 |
| RXD0 | Receive Pin for Programming MSP430 |
| P20 | Pressure Out – Interface Module |
| P21 | I Out – Interface Module |
| P22 | Q Out – Interface Module |
| P23 | General I/O – Extra Pin From MSP430 |
| P24 | General I/O – Extra Pin From MSP430 |

This power is filtered through a inductor on the power board. These three signals provide electric power to every component in the telemetry system.

The connections labeled Test, RST, TXDO, and RXDO are the main MSP430 programming signals along with two power signals. The TEST pin provides a test signal when the MSP430 is being programmed. TXDO and RXDO are the transmit and receive signals to program the MSP430 and RST is the reset signal for the MSP430.

There are five general I/O pins that connect directly to the microcontroller module, P20 – P24. Pins P23 and P24 are set as general I/O pins and are connected to the main bus, serving as optional pins for future connections.

Pins P21, P22, and P23 used in the communication between the interface module and microcontroller module. Here, P20 represents the voltage created from the pressure section of the interface module, and P21–I out, P22–Q out represent the output of the volume section of the interface module. These three signals are connected to the analog inputs of the microcontroller,

where each signal is sampled and processed digitally. The generation of these three signals are discussed in Sections 3.5.2 and 3.5.3.

The communication bus architecture for the first prototype provides each module with only the necessary connections, with two optional connections (P23 and P24). However this was necessary in the first prototype as only a proof of concept was needed. However, in order to create a more functional and advanced telemetry system, a more complex communication bus architecture is needed.

### 3.4.2 Phase 2 – Communication Bus

The second prototype includes a communication bus with a total of 88 pins or 175% increase over the first version, Table 3.2. The additional pins are warranted due to the more expandability and complexity of the second prototype. In this version, the 88 connections can be broken into the following groups: power signals, ground, SPI, programming, and general input and output.

In this version, the system voltage and HF voltage pins are increased to two pin allocations each. Three additional power signals are added to this improved architecture, interface voltage, 1.8 V ref signal, and 5 V USB charging. The interface voltage rail provides power to the interface module through a SPST analog switch located on the Power Module, Section 3.1.5. The 1.8 volt rail is added because of the relocation of the voltage reference chip to the Power Module. Finally, a 5 V power rail is added to the bus to allow for USB charging directly to the battery. There are a total of 44 ground connections used in this architecture of the Communications Bus. The additional grounds do not affect the overall function of the system but do provide additional connections on each module, simplifying the layout. The SPI and programming connections remain the same in this version.

The main additions to this communications architecture are from the added I/O pin. Twenty seven I/O pins are connected to the bus in this version. Here, the pins are allocated into six specific categories: general I/O, power monitoring, enable pins, analog inputs, Interface Mod-

Table 3.2: Communication Bus in the second prototype

| **Pin** | **Function** |
|---|---|
| System Voltage | 3.6 Volt Rail for System Voltage – From Power Module |
| HF Voltage | 3.6 Volt Rail for RF Module – From Power Module |
| Interface Voltage | 3.6 Volt Rail for Interface Module – From Power Module |
| 1.8 V Reference | 1.8 Volt Reference for Interface Module – From Power Module |
| Ground | Ground – Connected Directly to the Battery |
| UCB0STE | Chip Select for SPI Bus |
| UCB0SIMO | Slave In, Master Out for SPI Bus |
| UCB0SOMI | Slave Out, Master In for SPI Bus |
| UCB0CLK | SPI Clock |
| GDO0 | Interrupt for communication between CC2500 and MSP430 |
| GDO2 | Interrupt for communication between CC2500 and MSP430 |
| TEST | Test signal using in programming MSP430 |
| RST | Reset signal to MSP430 |
| TXD0 | Transmit Pin for Programming MSP430 |
| RXD0 | Receive Pin for Programming MSP430 |
| P17, P40, P47, P36, P10, P11, P13, P14, P15, P16 | General I/O – Extra Pin From MSP430 |
| P25 | Digital Potentiometer Control – SPI on and off |
| P20 | Power Supply Voltage (To Monitor Power to the System) |
| P21 | Power Efficiency |
| P22, P37, P23, P24 | Analog A2, A7, A3, A4 |
| INA1 Out | Interface Board Split – Mag/Phase Method |
| SINE | Interface Board Split – Mag/Phase Method |
| Q Gate | Interface Board Split – Lock-in Method |
| I Gate | Interface Board Split – Lock-in Method |
| P41 | Duty Cycle of the Oscillator – Mag/Phase Method |
| P42 | Duty Cycle of the Heart Signal – Mag/Phase Method |
| P43 | Rectifier Out – Mag/Phase Method / Q Out – Lock-in Method |
| P44 | ECG Out – Mag/Phase Method / I Out – Lock-in Method |
| P45 | Pressure Out – Mag/Phase Method and Lock-in Method |
| P46 | Magnitude Out – Mag/Phase Method |
| P12 | Interface Module Enable |

ule outputs, and Interface Module separation. There are ten digital general I/O ports and four analog inputs that are un–allocated on the bus, for future use if needed. Two pins are allocated to monitor the power efficiency and the power supply voltage when an optional wireless power module is added, not currently used in the battery based system. Two enable pins are allocated to control the Interface Module's power supply and the digital potentiometer SPI bus in the magnitude phase version of the Interface module.

Four signals are used in the PCB separation of the Interface Modules, two for each version. These four signals are shared across two physical pins, as only two are used at one time. Six signals are used to form the outputs of the Interface Module, with each version sharing these outputs.

For the lock-in method, P41, P42, and P46 are allocated as general I/O and are not used for any outputs. P43, P44, and P45 are used as the main outputs of this module where P43 represents the Q Out, P44 the I Out and P45 represents the output voltage related to pressure output. For the magnitude and phase method, additional pins are used to monitor various stages of this design. P43, P44 are examples of this and represent the rectifier and ECG signals, respectively. P41 is assigned as the duty cycle of the oscillator, P42 is assigned to the duty cycle of the heart signal, P45 is associated with the output voltage representing the pressure signal and P46 is assigned the Peak Gain Out on the Interface Module.

## 3.5 Interface Modules

The Interface Modules provide the electronics to connect the medical catheters to the telemetry system. Each catheter is connected to the Interface Module directly with the designed electronics providing a way to translate the raw analog signal from the sensor to accurate pressure–volume (PV) data.

Each Interface Module contains electronics to decode both PV data, Fig. 3.11, where M1, M2, M3, M4 represent the volume measurement inputs and SR1, SR2, and COM represent

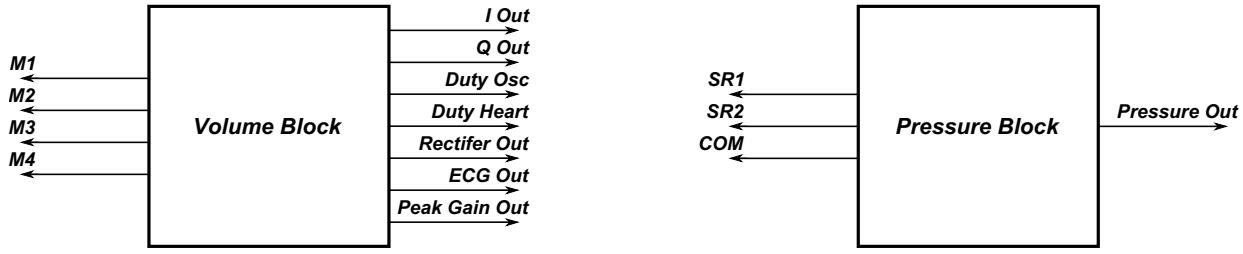


Figure 3.11: Interface Module block diagram.

the pressure measurement inputs. In this implantable telemetry system, two different pressure measurement methods and two different volume measurement methods are used. The following subsections will describe the catheters used in this design, as well as both versions of the pressure and volume measurements.

### 3.5.1 Catheters

Catheters are an essential part of the wireless telemetry system as they provide the structure to house the bio–medical sensors along with a direct connection to the telemetry system. Catheters can contain various types of bio–sensors, in this research project, only two types of sensors are used, pressure and volume. These sensors can be separated into three catheter types: pressure only, volume only, and combined PV, with this design utilizing PV catheters.

An example of a pressure volume catheter used in this system is shown in Fig. 2.4. This diagram represents a 1.2 French catheter, with a width of 0.4 mm. It contains four electrode rings and a pressure sensor separated at specific distances. The top and bottom sets electrodes are separated by a distance of 4.5 mm with each set separated by 0.5 mm. The tetra–polar catheter is inserted directly into a small animal subject's left ventricle to measure blood pressure and volume. The two outer electrodes inject current into the blood and the two inner electrodes measure the voltage created by the electric field inside the left ventricle. Conductance/admittance is calculated from the known current and measured voltage. The blood pressure is directly determined from the included pressure sensor.

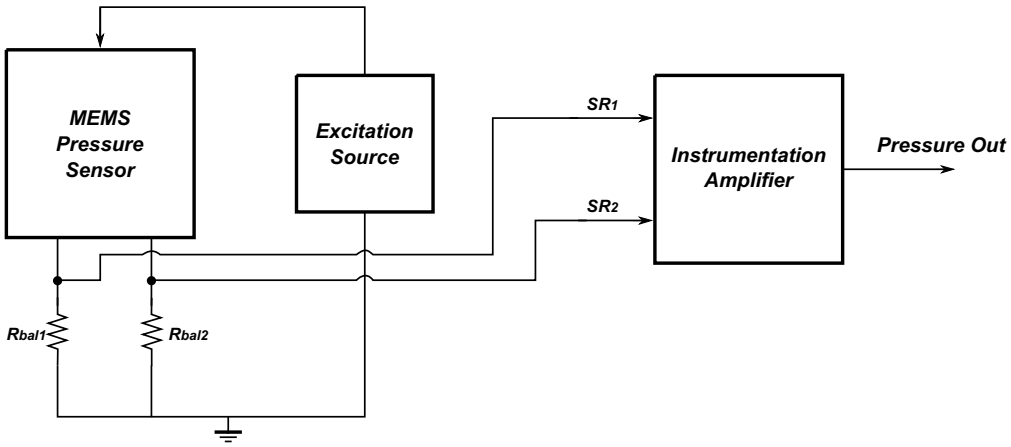


Figure 3.12: Pressure measurement block.

### 3.5.2 Pressure Measurement

The pressure measurement block contains the electronics to convert the pressure created by the blood on the catheter (mmHG) to a voltage (V). This voltage is obtained by the use of a catheter containing a small MEMS based pressure sensor, Section 3.5.1. This pressure sensor is connected directly to the pressure block electronics for processing using three wires, SR1, SR2 and COM. These three wires are used to excite the pressure sensor and provide voltage measurement, Fig 3.12. The pressure sensor used in this telemetry system is the GE P161 Pressure sensor [82]. This is a MEMS based sensor and contains two pressure sensitive resistors with a nominal resistance of 800 Ω. A wheatstone bridge configuration is used as the main voltage measurement method.

The wheatstone bridge is an combination of four branches of resistors used to measure an unknown resistance, by balancing two branches of the bridge circuit, with one branch including the unknown resistance, Fig. 3.13. Nodes A and B represent the measurement points and Ext is the excitation signal. The top two resistors, P1, P2, in the bridge represent the pressure sensor and the bottom two R1, R2, are external matching resistors. If the measured voltage between nodes A and B is zero then the bridge is balanced, in other words there is no pressure exerted. When pressure is exerted on the sensor, the resistance of P1 and P2 will increase

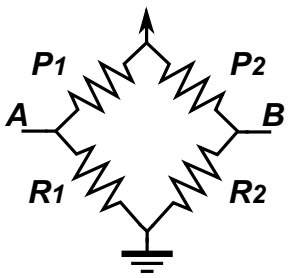


Figure 3.13: Example wheatstone bridge.

or decrease based on the difference in pressure from the calibrated pressure. The calibrated pressure is when the bridge is balanced i.e., no measured output voltage. The sensor resistor P1 will increase when P2 decreases and vice versa, this causes the bridge voltage to be linearly based on the pressure exerted.

In most wheatstone bridge configurations the bridge is driven by a voltage source rather than a current source. In this system, a current source is used because of two main reasons. The first is that current driven whetstone bridges have the advantage of not introducing measurement errors when the excitation circuit is far away from the sensor. In this telemetry system, the catheter is located away from the main electronics and could introduce measurement error due to the increased wire length and wire resistance if voltage driven circuits are used. The second benefit is the pressures sensitivity is directly linear to the excitation current, allowing the sensitivity to be controlled.

The external components of the wheatstone bridge ( R1, R2, Current source) must be completed based on the specifications of the pressure sensor. As the pressure sensor contains two nominal 800 Ω resistors, the bridge completion resistors must be close to 800 Ω to balance the bridge correctly. As well, a constant current source must be constructed to provide the nominal current needed to excite the pressure sensor and drive the circuit. The bridge completion resistors are generally tuned or trimmed to get the resistance needed to complete the bridge. Generally, exact 800 Ω resistors are not used as some adjustment must be made to offset the effects of wire resistance, temperature, etc. Two methods exist to tune these resistors: Analog

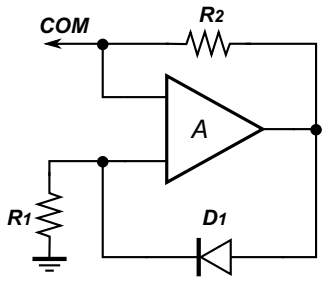


Figure 3.14: Current source design.

and Digital trimming, with each method discussed in detail below.

The current source is constructed using an OP–Amp, a diode and two resistors, Fig. 3.14. This current source is located next to the interface electronics and is directly connected to the pressure sensor through the COM pin on the sensor. The constructed current source is designed to provide $\sim 580 \mu A$ of current as required by the pressure sensor. The current source used is a simple diode and sense resistor configuration. The voltage drop of the diode across the resistor R2 provides the correct current to the sensor.

**Analog Resistive Trimming**

The first version of the telemetry system uses analog resistors to complete the wheatstone bridge, Fig. 3.15(a). In most cases, sets of high precision resistors are connected in parallel to balance the bridge more effectively rather than single resistors. If the overall volume allows, analog potentiometers (POTs) are used to provide additional resistance trimming capabilities. However, these are larger in size and create a lot of mechanical noise. The benefits of using standard resistors or analog (POTs) are that they provide very accurate results as well as generally costing less and no additional ICs are used. The additional space increase for potentiometers and mechanical noise is a downfall of this method. As well, if only precision resistors are used no additional resistance trimming can take place once the circuit is constructed.

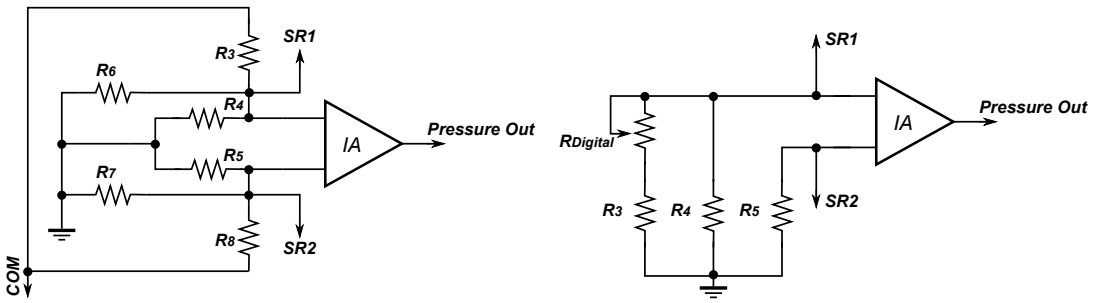


(a) Analog Tuning (b) Digital Tuning

Figure 3.15: Pressure measurement design using (a) Analog Tuning and (b) Digital Tuning techniques along with current source in Fig. 3.14.

**Digital Resistive Trimming**

The more modern way to trim the bridge completion resistors is to tune them digitally. Instead of a mechanical potentiometer that is much larger and can create noise in the circuit, a digital potentiometer is used. This digital potentiometer is a small IC, that is able to provide the same functions as an analog potentiometer but be controlled using SPI communication. These ICs contain many set interval steps between 0 Ω and the maximum resistance. This method is used in the the second version of the telemetry system prototype, Fig. 3.15(b). For example, the digital potentiometer used in the second prototype is a 10KΩ digital potentiometer with 1024 steps, Maxim MAX5484. These POTs are generally connected with additional high precision resistors in parallel to get the exact bridge completion resistance. The digital POTs allow for constant resistive trimming to the bridge during operation. The digital pot in the telemetry system is controlled using the SPI bus from the microcontroller.

### 3.5.3 Volume Measurements

The blood volume is measured using the same catheter as in the pressure measurements, however four electrodes are used rather than a MEMS sensor. These four electrode rings provide the excitation signal to the heart, as well as an interface to provide the voltage measurement, Section 3.5.1. The four rings connect directly to the interface electronics enabling analog processing of the voltage signal and conversion to a volume measurement.

As discussed in the background theory, Section 2.4.2, admittance measurement techniques are used to accurately measure the blood volume in the heart. Two methods are implemented in this telemetry system that precisely measure admittance from the PV catheter. Both methods, lock–in and magnitude and phase, measure a voltage and convert it to a magnitude and phase measurement or into I, Q values. These parameters are used to calculate the admittance, (2.5).

### Lock–in Amplifier Method

One technique to achieve an accurate volume measurement using admittance is to use the Lock–in amplifier technique. This method utilizes the theory of phase–sensitive detectors discussed in detail in Section 2.5. This type of circuit allows the low amplitude voltage signal to be extracted from the noisy environment (e.g., animal body) and amplified to a useable signal.

The circuit implementation of the lock–in amplifier used in this system is realized by the block diagram in Fig. 3.16 where nine stages are used to excite the catheter and extract the in–phase (I) and quadrature (Q) DC voltages to calculate the complex admittance using equations (3.3) and (3.4).

$$Voltag\ Magnitude = \sqrt{I^2 + Q^2} \tag{3.3}$$

$$Voltage\ \theta = \tan^{-1}(Q/I) \tag{3.4}$$

A quadrature oscillator is designed, Fig. 3.17 to generate sine and cosine signals at 19.866 $kHz$ centred around the virtual ground of 1.8 V. As discussed in Section 2.4.2, exciting the heart with a frequency of $\sim$20 $kHz$ causes the blood to become purely resistive and the heart muscle to contain both resistance and capacitance properties, allowing only the blood volume to be measured. This implementation uses only six passive components (three 820 $pf$ capacitors and three 9.76 $k\Omega$ resistors) and two operational amplifiers. High slew rate amplifiers are needed to achieve the required frequency and switching speed of the oscillator. Other oscillator

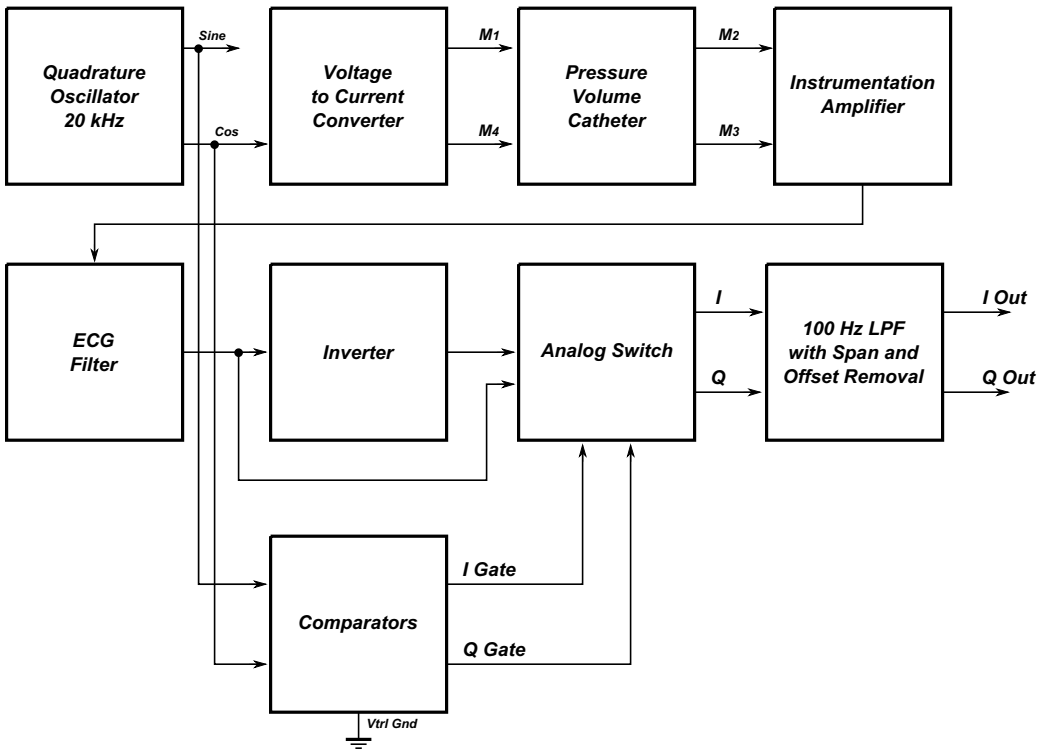


Figure 3.16: Lock–In implementation of Interface Module.

configurations were researched such as phase shift and Wien Bridge oscillators [83] however to achieve the required frequency, dual output (sin and cos) and full voltage swing required more discrete components to create the equivalent circuit.

The reference signals for the analog multiplier are created using two comparators. The inputs to these comparators are the generated sin and cos waveforms and the virtual ground. The resulting output signals are frequency locked square waveforms providing a phase reference for the excitation signal and are connected to the analog switch.

The in phase or cosine signal is used to directly excite the heart through a voltage to current (V to I) converter. This V to I converter uses three resistors (20 $k\Omega$, 12 $k\Omega$, and 1 $M\Omega$) and one operational amplifier to achieve 61 $\mu A$ of alternating current, Fig. 3.18. This current is achieved by using equation (3.5). Additional DC offset compensation is achieved through resistor R4. The two input rings on the catheter are connected to the output of the V to I converter through two 1 $uF$ DC blocking capacitors and a 1 $M\Omega$ resistor separating the two nodes of the circuit.

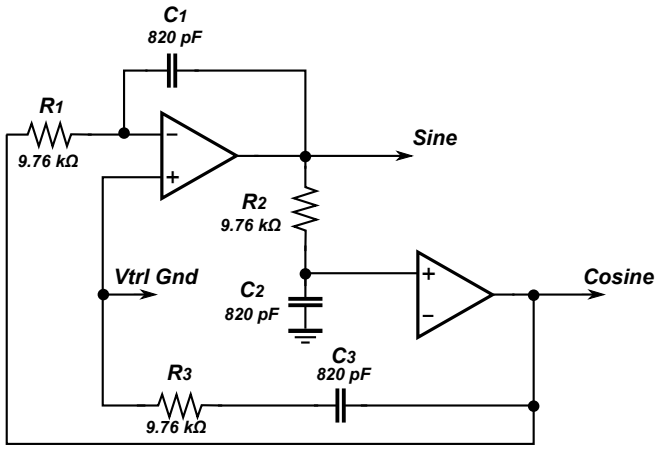


Figure 3.17: Quadrature Oscillator designed with a $F_0$=20$kHz$.

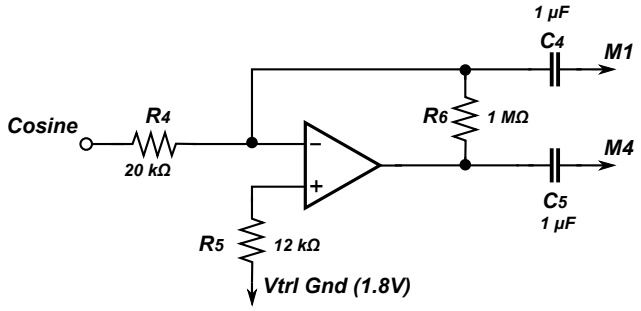


Figure 3.18: Voltage to Current converter implemented.

This excitation current generates an electric field between the two outer rings enabling a voltage to be measured.

$$\begin{aligned} I &= \frac{V_{rms}}{R} \\ I &= \frac{1.22V_{rms}}{20k\Omega} \\ I &= 61\mu A \end{aligned} \tag{3.5}$$

The voltage created by the electric field through the heart is measured through an instrumentation amplifier (IA) with a gain 26 $dB$, Fig.3.19. Two 10 $nF$ capacitors are used to decouple any DC offset created from the electrode rings during measurement. In addition, two 100 $k\Omega$ resistors are used to restore the virtual ground offset to the incoming AC signal. Finally,

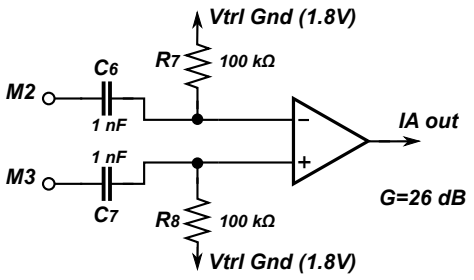


Figure 3.19: Instrumentation Amplifier configuration.

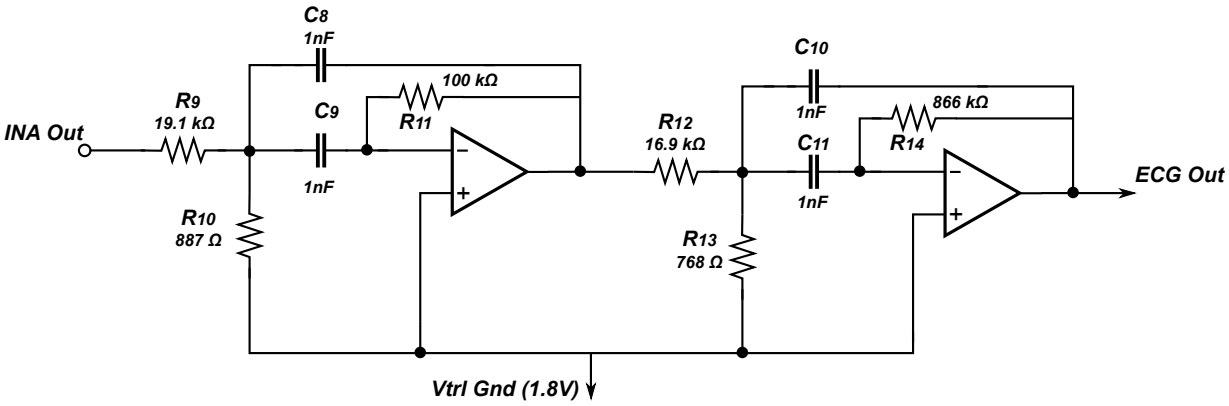


Figure 3.20: ECG bandpass filter to remove ECG signals measured from surrounding heart nerves.

the voltage difference is amplified with a gain of 26 $dB$ to be further processed.

Along with the desired voltage waveform the electrode rings will also measure the electrical signals created from the surrounding heart nerves and muscles causing additional unwanted noise in the signal. A bandpass filter is used to remove the ECG signal and additional noise contained in the measured AC signal. A $4^{th}$ order, two stage multiple feedback bandpass filter is designed with a total gain of 12.04 $dB$ and is centred around 18.59 $kHz$ with a passband of 4 $kHz$. A total of 10 passive components (6 resistors and 4 capacitors) and two OP–Amps are used to implement this filter, Fig. 3.20. This amplified and filtered signal is the main input to the next stage of lock–in amplifier – the phase sensitive detector.

Section 2.5 indicated that the main blocks of the phase sensitive detector are the mixer and low pass filter. It was also noted that one of the simplest forms of a mixer is an inverter/switch

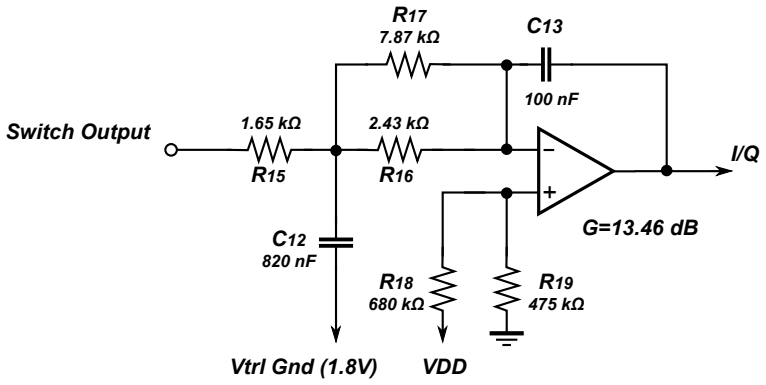


Figure 3.21: 127 Hz Low Pass filter with gain and span included.

combination, Fig. 2.8. The designed interface module implements this mixer architecture with an active low pass filter design. The inverter block is implemented by an unity gain inverting amplifier configuration. An analog switch is used to complete the mixer configuration. To extract both I and Q values, two analog switches are needed. The input to each switch is the inverted and the non–inverted filtered signal with the frequency locked square waves providing the switching controls.

The high frequency harmonics of the output waveform are removed using a low pass filter to reduce the waveform to a DC level which is directly proportional to the magnitude and phase of the voltage signal. To obtain maximum SNR, the DC signal must span the full input range of the microcontroller (0 – 3.6 V). This is achieved by removing the virtual ground offset of 1.8 V and amplifying the DC output to span between 0 and 3.6 V. A $2^{nd}$ order Bessel active low pass filter with a cut-off frequency of 127 $Hz$ is designed with a gain of 13.46 $dB$ and resistors to remove the DC offset, Fig. 3.21. Each switch output is connected to a separate active low pass filter block. The outputs, I and Q, are connected to the communications bus for the MSP430 to convert into magnitude and phase values for the measured voltage. This complex voltage along with the known excitation current are used to calculate the complex admittance to be converted to an absolute volume.

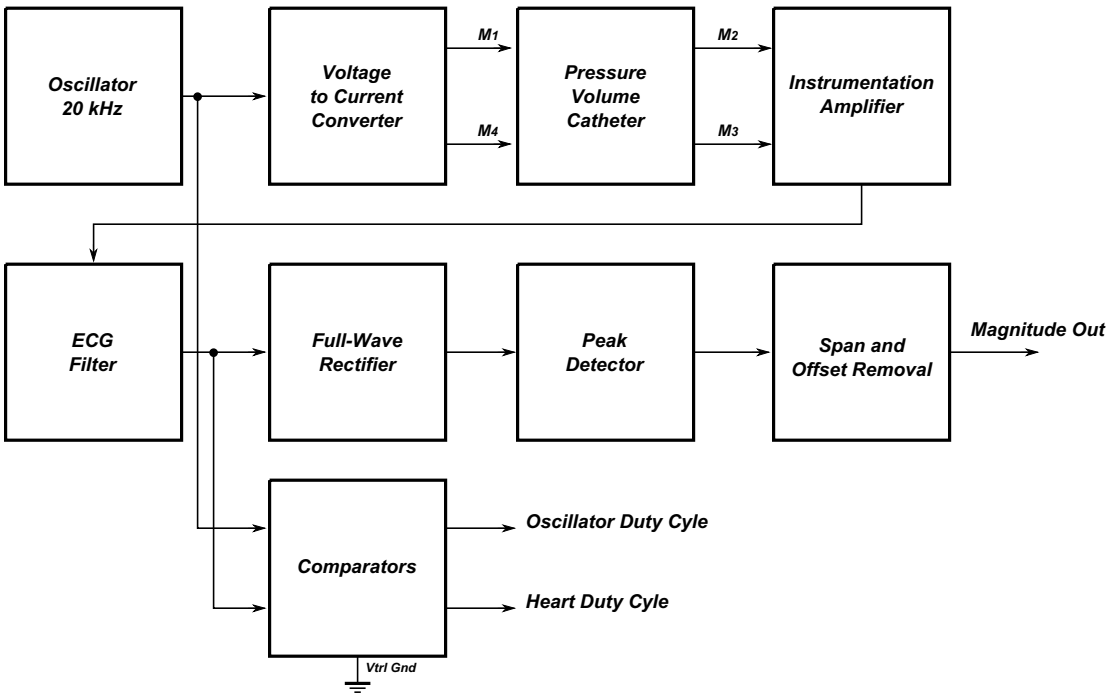


Figure 3.22: Interface Module using the Magnitude and Phase Method.

### Magnitude and Phase Method

The second technique to extract the complex admittance from the measured AC voltage is to use a more straightforward approach. In this method, the magnitude and phase are extracted directly from the measured signal. Based on the mathematical theory of sinusoid signals, a circuit is created to implement the calculation of the magnitude and phase of the measured voltage signal. In comparison to the lock–in method, this technique does not require a mixer or additional filtering to extract the specific signals. Rather, the magnitude is directly measured by using an envelope detector on the rectified signal and the phase is directly extracted using a set of comparators and the microcontroller. A total of eight sub–blocks are used to implement the circuit for the interface module, Fig. 3.22, from creating the excitation signal to the extraction of the magnitude and phase values.

For the same reasons outlined in the lock–in method, an oscillator is needed to excite the catheter inside the test subject. In this method, only a single sinusoid waveform is needed

not both sine and cosine signals, as the lock–in method is not used. Additional sine oscillator designs were researched however, the existing quadrature oscillator design contained the lowest component count to achieve the required signal. Hence, the same circuit design was chosen for the oscillator sub-block, Fig. 3.17. The cosine output of the quadrature oscillator is not used in this version, only the sine output. The circuit implementation, Fig. 3.18, of the voltage to current converter used in the subsequent block is identical to the previous method's impelmentation as well. The AC voltage from the induced electric field is measured using an instrumentation amplifier configuration similar to Fig. 3.19 and the ECG signal is filtered through the designed ECG bandpass filter, Fig. 3.20. The remaining circuitry deviates from the lock–in method with four new sub-blocks.

To extract the magnitude or absolute value of the signal the waveform must be rectified. The circuit implementation of the rectifier has to satisfy various requirements as to remain as close as possible to the ideal rectified sinusoid. These requirements include minimal peak loss, operate on a single supply voltage, low component count, full wave rectification, and work within the operating frequency of the system. A four diode bridge configuration was first researched as this would provide the lowest component count and would provide full rectification if used with a symmetrical power supply. However, the peak loss created by the diodes' voltage drop was unacceptable for the power supply used in this system. For example, if standard 0.7 V drop diodes are used, a total of 1.4 V is lost in rectification process from the original power supply maximum of 3.6 V. Therefore, this configuration was not implemented in the system. Active rectification methods are needed to mitigate the peak loss created by any diodes used in the circuit topology. The main issue with discrete active rectification methods is that most topologies are designed with symmetrical power supplies in mind. This creates a problem if implemented in the proposed telemetry system architecture as a single ended power supply is used, substantially reducing the amount of topologies to choose from. A two stage single supply active full wave rectifier [84] is chosen as the implemented rectifier design, Fig. 3.23.

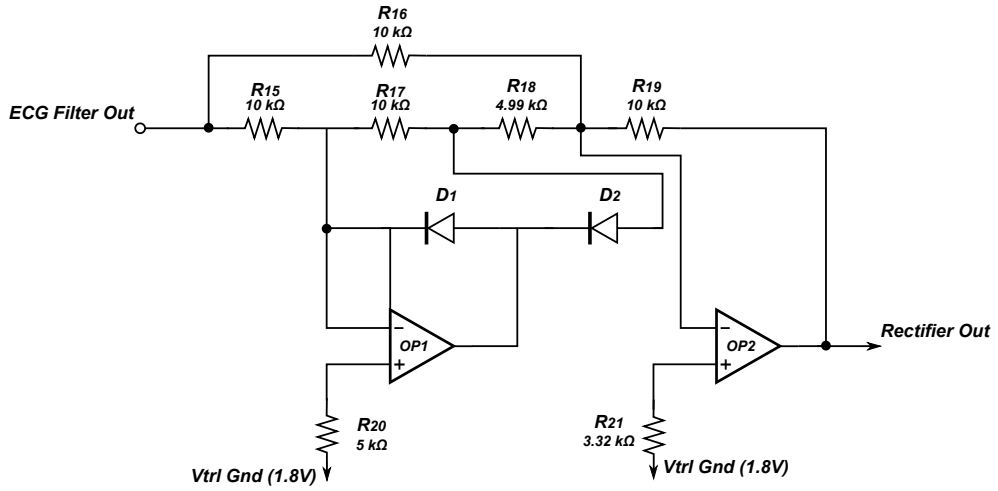


Figure 3.23: High precision two stage full wave rectifier.

This full wave rectifier is separated into two stages defined by their respective OP-Amp configuration. In the first stage, OP1 has two defined states: an inverter with a gain of one and a unity gain buffer with a output equal to virtual ground; that are controlled by two diodes D1 and D2. State 1 is active when the input voltage is greater than virtual ground causing D2 to be on, enabling the inverting amplifier configuration. State 2 is active when the input voltage is less than virtual ground causing D1 to be on, creating the unity buffer configuration. The overall function of the two states of OP1 is a half wave inverter. For the case when $V_{in} = Vtrl\ gnd$, D1 and D2 are off causing OP1 to be completely disconnected from the output of the rectifier. This can lead to irregularities in the output voltage where the output voltage is calculated as $V_{out} = V_{in} \times R19 \times (R16 \parallel R15 + R17 + R18)$. The second stage of this rectifier is defined by OP2's operation, where it sums the inverted half wave signal with the original waveform and amplifies it with a gain of 6.02 $dB$. The combination of the two stages creates the full wave rectified signal. In addition, resistors R20 and R21 in Fig. 3.23 are used to limit the bias current due to the voltage offsets created by the input impedance the inverting node of each amplifier.

Peak amplitudes are detected from the rectified waveform by using an peak detector, Fig. 3.24. A general peak detector can be made with a diode connected to a resistor in parallel with a capacitor. However, a super diode configuration is needed to counter the peak loss created by

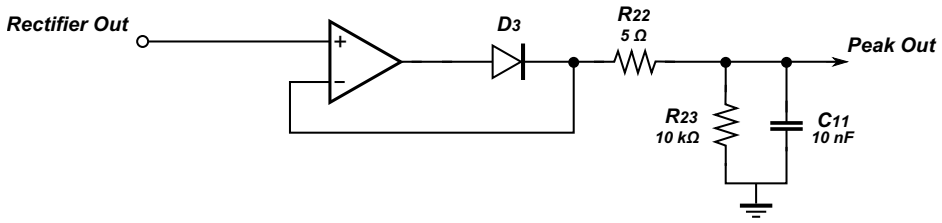


Figure 3.24: Envelope detector for amplitude detection.

the turn on voltage of the diode. To calculate the values of the RC components two conditions must be met for the envelope detector to work properly [85]. First off, the output voltage should follow the envelope of the signal rather than the changes in the main excitation signal. The time interval between each peak is controlled by the discharge rate of the capacitor. This rate is approximately equal to the inverse of the excitation frequency, or in this case $\frac{1}{19.4\,kHz}$. In between each peak of the excitation signal the output voltage of the envelope detector is defined by $V(t) = \exp(-1/f_c RC)$. Hence, for the output voltage to only follow the peaks, the timing constant RC should be chosen to be close to $\frac{1}{F_c}$. The timing constant must also be small enough so that the peak detector can still follow changes in the envelope not only the peak values. The changes in the envelope itself are related to the message bandwidth (mb) ( e.g., the heart rate of the animal), with the timing constant resulting in a value close to $\frac{1}{f_{mb}}$. These conditions are combined (3.6) to calculate a timing constant to allow the envelope detector to work correctly for the given excitation frequency and heart rate (message bandwidth).

$$\frac{1}{f_c} \ll RC \ll \frac{1}{f_{mb}} \tag{3.6}$$

For example, if the test subject is a small mouse with a maximum heart rate of 200 beats per min and allowing for 20 harmonics, the maximum frequency bandwidth needed is 6.66 Hz. Using this information with an excitation frequency of 19.4 $kHz$, a range of RC values can be found from 51.54 $\mu$Sec to 15.01 mSec. Through experimentation it was found a value of $RC = 500\mu Sec$ (10 K$\Omega$, 50 nF) adequately tracks the waveforms shape and allows for variations in the envelope bandwidth as well.

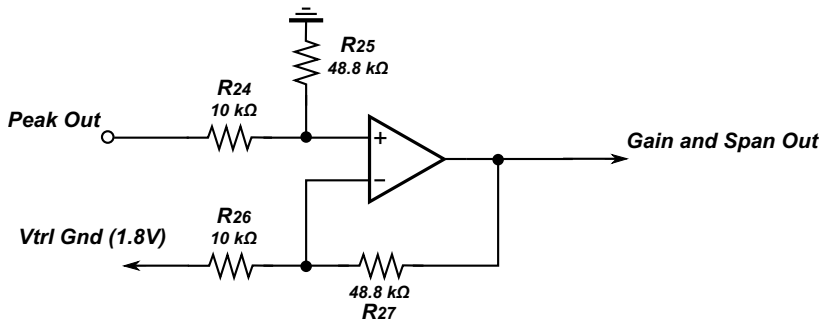


Figure 3.25: Span and offset removal circuit.

The span and offset removal block serves the same purpose as the lock-in amplifier method, to remove the virtual ground and span the output to a 0 to 3.6 V value. However, the implementation is slightly different, with the main difference being the lock-in method's implementation is combined with a LPF where only the span and offset functions are needed in this implementation. A difference amplifier is used, Fig. 3.25, to accomplish this function with an overall gain of 13.76 $dB$.

The phase difference between the excitation signal and the measured waveform is calculated in 4 steps. 1) Convert the excitation signal and output of the ECG filter (before rectification) to square waveforms. 2) These waveforms are read by the microcontroller's digital inputs, where the period of the excitation is calculated and stored in the MSP430's memory using timers. 3) The waveforms are XOR'ed in software where the output waveform represents the phase difference in time of the two signals, with a high voltage representing a out of phase signal and a low voltage as an in phase signal. 4) The phase difference is determined by the amount of time the XOR output is high with reference to the original excitation period. The measured signal can be out of phase 0-180 degrees from the original excitation signal. If the measured waveform is 180° out of phase, the XOR'd output will be high for the whole excitation signal's period. If the signal is in-phase then the XOR output will be low during this time. The phase difference is directly proportional to the time this signal is high. The specific

phase difference can be calculated using (3.7).

$$Phase\ Difference\ (^\circ) = \frac{Time\ XOR\ output\ is\ high}{Excitation\ Signal\ Period\ /\ 180^\circ} \tag{3.7}$$

This implementation of interface module uses envelop tracking similar to AM modulation methods to extract the magnitude and uses specific hardware and the MSP430 to extract the phase from the measured voltage signal. The electronics are much simpler than the lock–in implementation however, it is more reliant on the microcontroller for phase measurements. Magnitude measurements can be improved by adding additional filters and using lower voltage diodes. Phase measurements can be implemented in hardware however, this reduces the flexibility in correcting for phase offsets in signal path.

## 3.6 Summary

In this chapter an implantable wireless telemetry system architecture is developed. This system contains four main modules: power, microcontroller, radio, and sensor interface. Along with the four main modules, the communications bus architecture is discussed. Two interface module implementations are developed, Lock–in method and magnitude and phase, to interface the pressure–volume sensors to the wireless system. The proposed telemetry system architecture is capable of measuring blood pressure and volume data from a test subject and wirelessly transmit it via a 2.45 $GHz$ RF signal to a end device for full processing.

# Chapter 4

# Simulation and Experimental Results

In this chapter, simulation results of the interface modules will be shown. Two prototypes were constructed based on the architecture designed in Chapter 3. The construction and 3D modelling of these prototypes are discussed. In addition, the test setups used in the preliminary experimental testing are also examined along with the initial test results.

## 4.1 Simulation Results

Each interface module version is simulated before the physical construction to ensure proper operation. Behavioural simulations are completed on the direct magnitude and phase method and SPICE simulations were preformed on the Lock–in method.

### 4.1.1 Behaviour modelling

The magnitude and phase implementation of the interface module is simulated using behavioural modelling techniques inside the Cadence simulation environment. Each block in Fig. 3.22, is verified mathematically using Verilog–A behavioural modelling language. All the main circuit elements are treated as ideal elements either as Verilog–A code or ideal circuit models such as a voltage controlled voltage source. The goal of the behavioural simulations is to demonstrate

Table 4.1: Myocardial parameters used in behavioural simulations

| Domain | Conductivity (S/m) | Permittivity (F/m) |
|---|---|---|
| Myocardium | 0.17 | $4.419 \times 10^{-7}$ |
| Blood | 0.93 | $8.853 \times 10^{-9}$ |

that the functionality of the circuit.

A variable heart model is created that is based on a similar model developed by Wei [71], similar to Fig. 2.6. The value of the resistors and capacitors are treated as variables and controlled by an oscillator at a specific frequency. This frequency is the intended heart rate of the test subject. The myocardial parameters used in the simulations are shown in Table 4.1. There is no Electrocardiogram (ECG) filter used in these simulations as the circuit is ideal. A voltage controlled oscillator is used to excite the system and provide an input to the comparators that are created using ideal behavioural models. The rectifier is represented by the mathematical function $|X|$ and is created in one single block with the peak detector. There is also no need to create a span and offset removal as everything is ideal and power supplies are not an issue. Instead of having the output's of the comparators connected to the microcontroller as is the case in the actual design, an ideal XOR gate is used instead to measure the phase difference in respect to the duty cycle.

This behavioural model is simulated with a input frequency of 20 $kHz$, Fig. 4.1(a) and the heart model is controlled by a voltage source with a frequency of 17.5 Hz. An example simulation ran for 100 ms and created differential amplifier, Fig. 4.1(b), magnitude, Fig. 4.1(c), and phase, Fig. 4.1(d) measurements. These measurements are used to calculate the complex voltage, to be used in the admittance to volume conversion. As indicated by the simulation results the designed circuit behaves as expected.

### 4.1.2 Lock–In Circuit Simulation

The architecture of the lock–in amplifier implementation of the interface module is simulated using SPICE in National Instruments Multisim 12. SPICE models for each component were

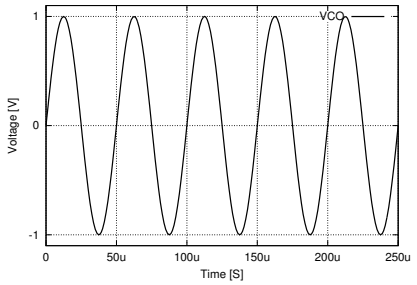


(a) VCO Excitation Signal with a frequency of 20 $kHz$

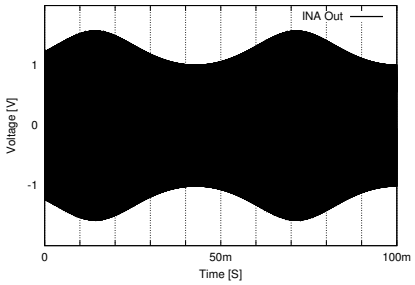


(b) Differential Amplifier Output

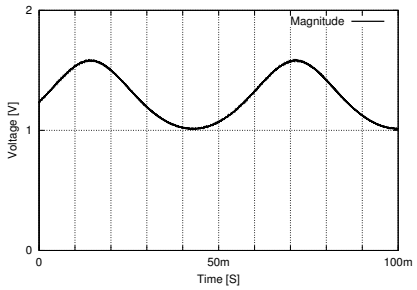


(c) Magnitude Output

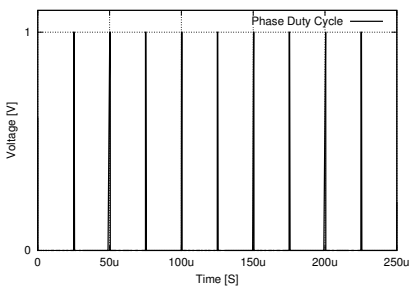


(d) Phase Output – Duty Cycle

Figure 4.1: Outputs of behaviour modelling simulations.

found to correctly model the operation of the Lock–In amplifier. Each block, as discussed in Section 3.5.3, is simulated for functionality. The blocks simulated are: quadrature oscillator, voltage to current converter, instrumentation amplifier, comparators, analog switch, gain and offset and the overall operation. A power supply of 3.6 V with a virtual ground of 1.8 V is used in the simulations along with LMV554 OP-Amps.

The quadrature oscillator designed in Fig. 3.17 is simulated. The oscillator produced two waveforms swinging from rail-to-rail and are 90° out of phase from one another, Fig. 4.2. The quadrature oscillator is designed to oscillate at 19.86 $kHz$ however, in simulations the oscillation frequency is found to be 18.6 $kHz$. Each resistor and capacitor is given realistic tolerances which attributed to the difference in oscillations. The voltage-to-current converter, Fig. 3.18, is simulated using a sine wave as the input with a frequency of 18.6 $kHz$ to produce the expected 61 $\mu A$ of AC current. The heart model used in these SPICE simulations is a simple parallel combination of a 100 Ω resistor and a 15 $nF$ capacitor. These components are

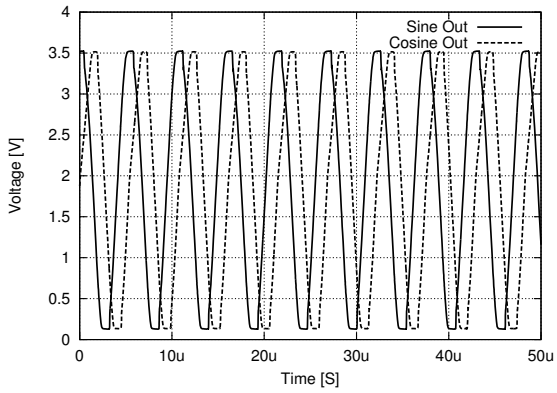


Figure 4.2: Quadrature Oscillator output where the solid lines represent the Sine output and dashed represent the Cosine output.

variable to allow the full heart cycle to be tested. The simpler heart model is used rather than the complex model used in the behavioural model because it reduces overall simulation times. The heart model is attached to the V-to-I converter and the instrumentation amplifier in the overall simulation. The instrumentation amplifier, Fig. 3.19, is simulated using two sin sources with 18.86 $kHz$, 1 $mv$ input signals 180° out of phase to verify the correct gain. The simulated frequency response of the ECG bandpass filter is shown in Fig. 4.3(a). The comparators block is simulated using the outputs of the quadrature oscillator and the appropriate square waves are created. The analog switch and gain and offset blocks are simulated together for validation. Two sine sources along with a digital pulse are used as inputs and a single output is measured. As discussed in Section 3.5.3, the gain offset block is a 127 Hz active low pass filter with a gain of 13.46 $dB$, the filter response is shown in Fig. 4.3(b). This testing process confirmed the functionality of each block before an overall simulation.

Each block is connected together along with the heart model to create the full lock–in amplifier implementation of the interface module. The full range of R and C values of the heart are simulated to validate the module however, only two specific simulations will be discussed, R = 100 Ω C= 0 nF and R = 50 Ω C = 15 $nF$.

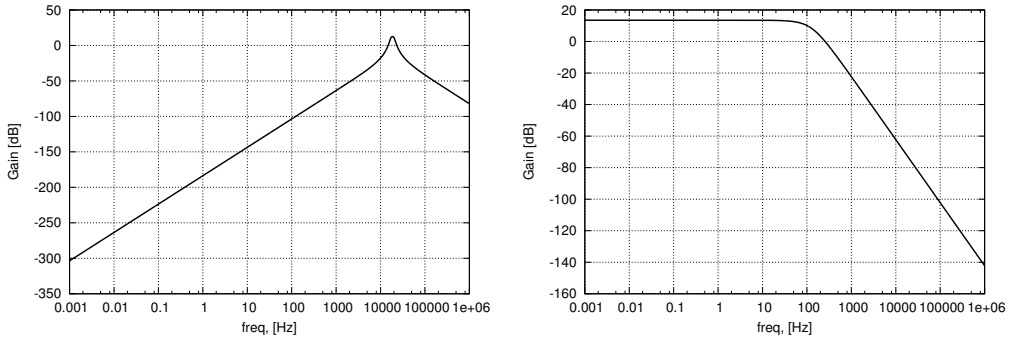


(a) ECG Filter (b) Low Pass Filter

Figure 4.3: Frequency response of (a) ECG filter with a centre frequency of 18.596 $kHz$ and a gain of 12.04 $dB$ and (b) $2^{nd}$ order low pass filter with a cut-off frequency of 127.4 $Hz$ and a gain of 13.4 $dB$.

**R = 100 Ω C= 0 nF**

The measured voltages at the inputs to the instrumentation amplifier with an excitation current of 61 $\mu A_{rms}$ are V+= 6.96 $mV_{rms}$ and V- = 993 $\mu V_{rms}$ and an output voltage of 478 $mV_{rms}$. The ECG filter used in the simulations is set with a gain of 3.02 $dB$ which further increased the voltage signal to 964 $mV_{rms}$, Fig. 4.4(a). The second control signal to the analog switch, the inverted signal is shown as well, Fig. 4.4(a). As described in the Lock–In amplifier theory in Section 3.5.3, the analog switch acts as a voltage mixer, the output in time domain of the in phase and quadrature signals are shown in Fig 4.5(a) and 4.5(b), respectively. The signal is then passed through the 127 $Hz$ active filter to reduce the upper harmonics, amplify the signal further, and remove the voltage offset. The output's of this stage are DC values proportional to the I and Q values of the measured voltage and are displayed in Table 4.2. In practice the measured IQ values would be converted to admittance if used to convert to an absolute volume. It should be noted that an initial calibration should be completed on a known resistive load to calibrate any phase shift and gain offset created by the components in the signal path. The process to complete this is not discussed in this thesis.

**R = 50 Ω C= 15 nF**

The second simulation example is completed in the same fashion as the initial example. For

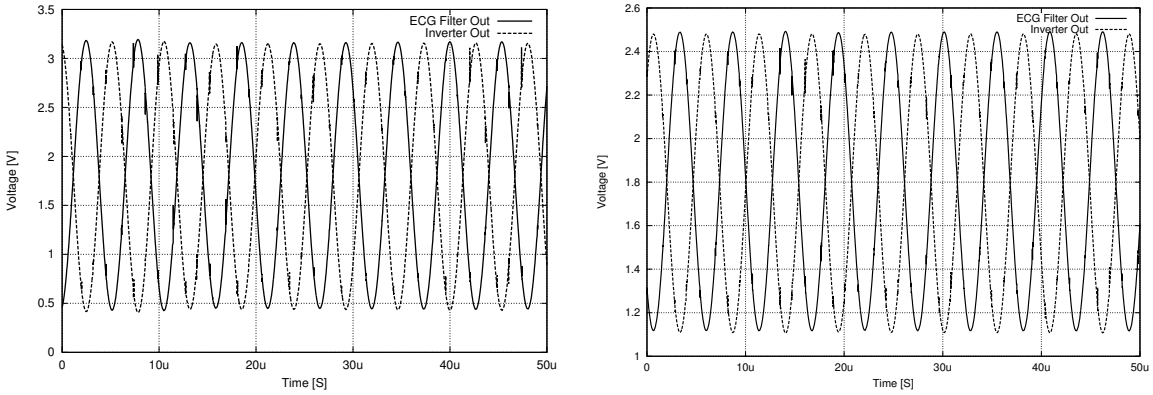


(a) R = 100 Ω, C = 0 $nF$ (b) R = 50 Ω, C = 15 $nF$

Figure 4.4: Outputs of ECG filter (Solid) and Inverter (Dashed) when (a) R = 100 Ω, C = 0 $nF$ and (b) R = 50 Ω, C = 15 $nF$.

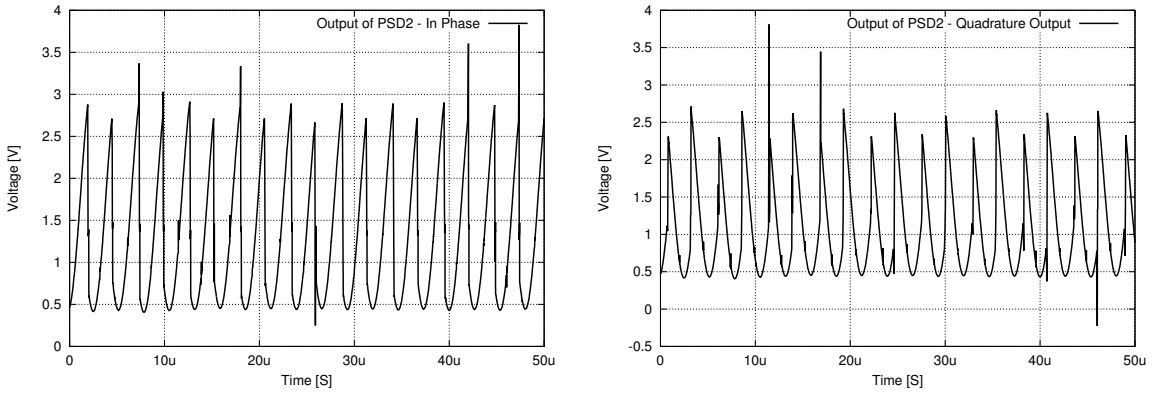


(a) In Phase Output of Phase Sensitive Detector (b) Quadrature Output of Phase Sensitive Detector

Figure 4.5: (a) in phase and (b) quadrature outputs of the dual phase sensitive detectors before the low pass filter, when R = 100 Ω, C = 0 $nF$.

Table 4.2: IQ values of R = 100 Ω, C = 0 $nF$

| Output | Measured Voltage |
|---|---|
| I | 3.31641 V |
| Q | 2.51542 V |

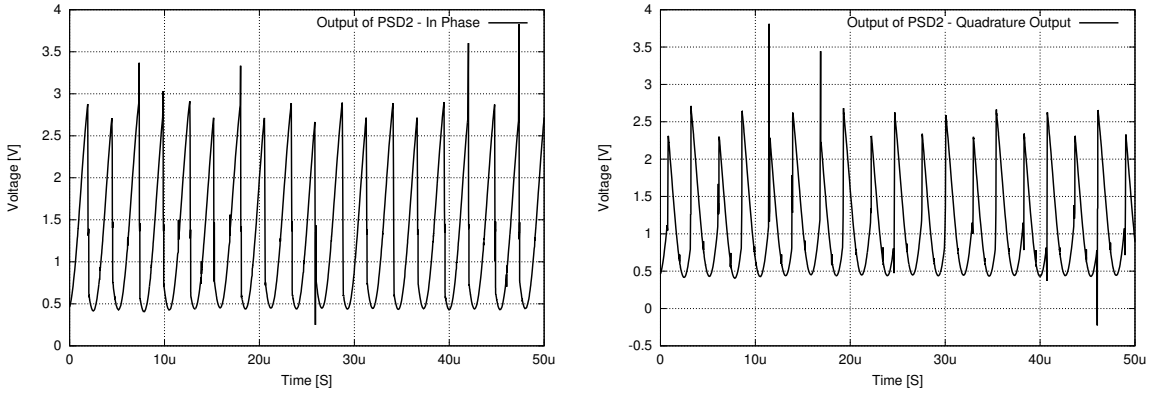


(a) In Phase Output of Phase Sensitive Detector (b) Quadrature Output of Phase Sensitive Detector

Figure 4.6: (a) in phase and (b) quadrature outputs of the dual phase sensitive detectors before the low pass filter, when R = 50 Ω, C = 15 $nF$.

Table 4.3: IQ values of R = 50 Ω, C = 15 $nF$

| Output | Measured Voltage |
|---|---|
| I | 1.560957 V |
| Q | 1.394040 V |

this specific load the inputs to the IA are V+ = 3.86 $mV_{rms}$, V- = 976 $\mu V_{rms}$ and an output voltage of 239 $mV_{rms}$. This is further increased to 487 $mV_{rms}$ by the ECG filter, Fig. 4.4(b), the inverted signal is also shown. The outputs of the analog switch for the in phase and quadrature signals are displayed in Fig. 4.6(a) and Fig. 4.6(b) respectively. Finally after low pass filtering and amplification, the measured I and Q values are shown in Table 4.3. These two examples demonstrate the validity of this implementation and allow for absolute volumes to be measured.

## 4.2 Physical Prototypes

Two physical prototypes are developed to implement the architecture designed in Chapter 3. The first prototype is a proof of concept design where functionality is the main design criteria and miniaturization a secondary one. A second prototype is created to further miniaturize the system by reducing the volume, weight and power of the system. 3D modelling is completed on both prototypes to ensure clearance and overall construction before the physical prototype

was manufactured. Each prototype is discussed in detail below.

### 4.2.1 Phase 1 – Prototype

The first prototype contained a total of seven printed circuit boards (PCBs) connected through a vertical communications bus. As discussed in Chapter 3, this first prototype contains the modules: power, microcontroller, radio and interface modules. Along with these four, two additional modules are created for testing and programming purposes.

This system is constructed on 1.6 mm thick FR-4 printed circuit boards and contains passive components of 0402 size. The boards varied from 2 layer to 4 layer designs. The additional layers are used as either power planes or for routing signals. Each module is designed on a 15 mm x 30 mm surface. This area contains all vertical connectors, integrated circuits (IC), passives and any other components needed. The telemetry system's modules are connected to each other in a stack formation. The interface module represents the top of the structure and the power module the bottom. The reason for this design decision is to allow easy access for the catheter to be soldered on at the top and the larger battery at the bottom of the structure. The vertical connectors increased the clearance in between each module to allow larger components to be used. The final assembled size of this prototype is 15 mm x 30 mm x 24 mm and contains the main four modules along with the Li–Poly battery.

**Power Module – Physical Construction:** As describe in detail in Section 3.1, the power PCB contains a low dropout (LDO) regulator, supervisor IC, USB charging IC and a battery. The majority of the ICs and passives are located on the top of the board leaving the bottom for the battery, Fig. 4.7. An additional five pin surface mount header is used to switch between the battery powering the system, charging or completely off. Two additional pins are used to connect a custom USB cable to provide an external 5 V connection. Small outline integrated circuit (SOIC) and mini small outline package (MSOP) packages are chosen for the ICs as they are more readily available and can be hand soldered. A LED is added to view if the the circuit

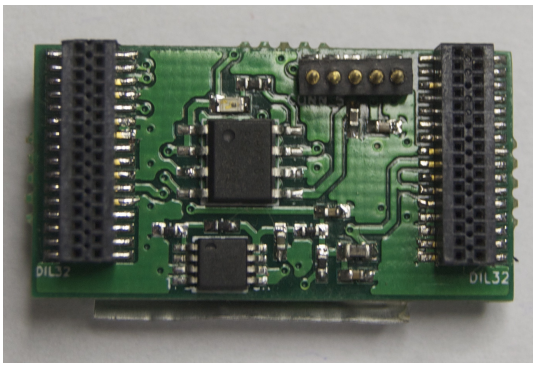


Figure 4.7: Power Module – prototype 1 PCB layout.

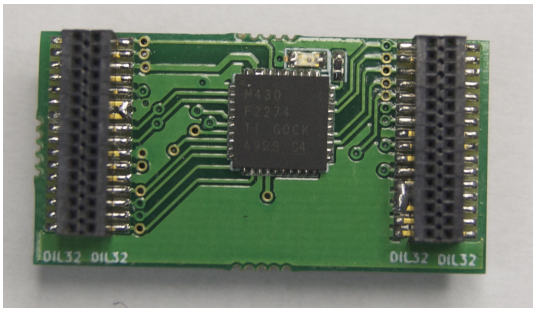


Figure 4.8: Microcontroller Module – prototype 1 PCB layout.

is operating, allowing to debug the power module if necessary. The MAX1811 is chosen to charge the Li–Poly batteries and can have either a 100 *mA* or 500 *mA* charge rate, 100 *mA* is chosen as required by the lower rated vertical connectors used. The general charging time is about 30min – 1 hr.

**Micro Module – Physical Construction:** The physical implementation of the micro module contains a single 40 pin no–lead package along with the headers and receptacles for insertion into the stack, Fig. 4.8. A test LED along with a current limiting resistor is added along with the microcontroller for programming tests.

**RF Module – Physical Construction:** The RF module in the first prototype is separated into two distinct PCBs, RF transceiver with supporting passives and an antenna board. The module is split into two PCBs, Fig. 4.9 due to the limited space and size requirements of the specific components used. The RF transceiver, CC2500, is also a no–lead package that contains 6

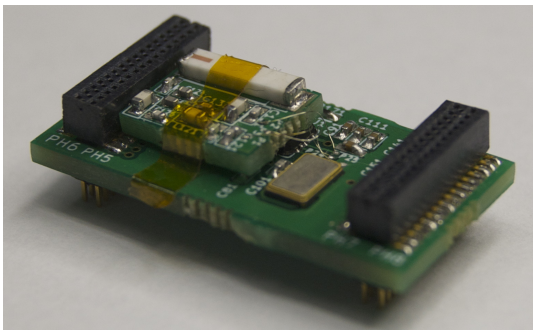

Figure 4.9: Radio Module – prototype 1 PCB layout.

decoupling capacitors and a bias resistor. The ABM3B 26 $MHz$ crystal is chosen to provide timing for the transceiver and has a physical size of 5 mm x 3.2 mm. With these components added along with the connectors there is no additional space left to house the antenna and matching network passives. Therefore, an additional PCB is created to accommodate the antenna and matching network with a size of 9 mm x 11 mm. The balun is created using a series of inductors and capacitors to not only convert the differential output to a single ended signal but also convert the output impedance to a intermediate source that is matched, Fig. 4.10(a). The matching network is passive based, created out of a single inductor and two capacitors, Fig. 4.10(b), to match to 50 Ω. The antenna chosen is a single ended chip antenna designed for 2.4 $GHz$ operation. This antenna provides about 30 m of range in non–line of sight configurations. This provides simple wireless connection to occur but is not suited for implantable devices as it is not modular and cannot be located away from the system (i.e., closer to the surface), to achieve lower power levels. The antenna also only has a distinct radiation pattern that does not fare well when placed into a stack configuration. These effects are taken into account when the second prototype is created. Finally, the antenna board is connected through three 42 AWG copper/ beryllium wires (RF+, RF-, GND) to the RF transceiver. The antenna PCB is placed on top of the RF PCB to complete the overall RF module.

**Interface Module – Physical Construction:** The interface module is constructed using a 4 layer PCB with the physical size of 21 mm x 30 mm, Fig. 4.11. The volume and pressure

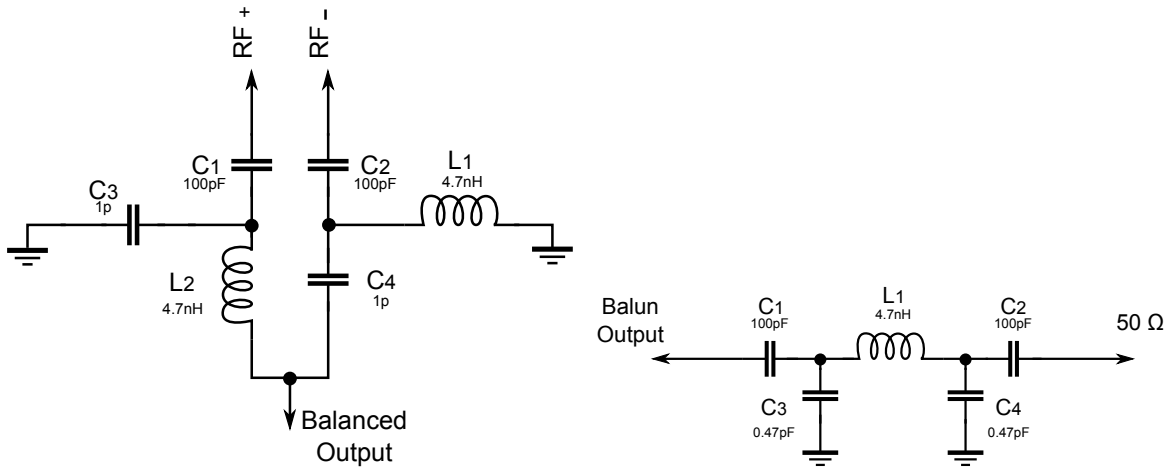


(a) Balun (b) Matching Network

Figure 4.10: (a) Balun used in first prototype (b) matching network used in first prototype.

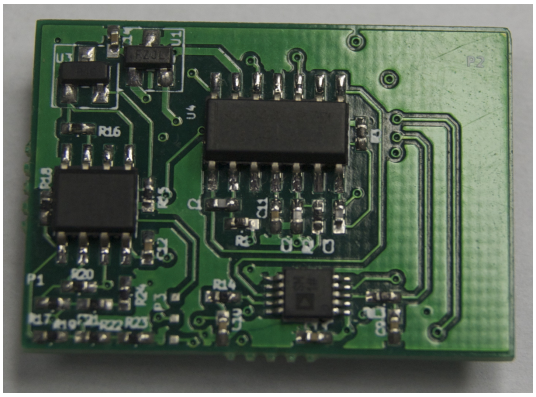

Figure 4.11: Interface Module – prototype 1 PCB layout.

electronics are located on this PCB. The IQ method is used in volume measurements and the pressure section was comprised of fixed resistances. In this version of the telemetry system the 1.8 V voltage reference is located in the interface module rather than the power module using a SOT-23 package.

The layout of the interface printed circuit board is separated into the volume electronics and the pressure electronics based off the designed schematic, Figures 3.15(a) and 3.16. Electronic packages are shared when needed by both sections. Analog Devices AD8607 and AD8609 are used in this system as they are micro power OP–Amps with 50 $\mu A$ of power consumption. These operational amplifiers are shared between sections to reduce the component count. The instrumentation amplifier (IA) is designed using two OP–Amps to reduce component count.

High precision resistors are used in this IA to reduce common mode rejection. Multiple 0402 passive components are also used in the construction of this module. In addition, a shunt voltage reference is used in the current source located in the pressure section to provide the voltage drop. Lastly, an Analog Devices ADG787 is used to accomplish the analog switch functions in the lock–in volume method. This IC is chosen as its a ultra low power device along with a 2.5 Ω on resistance and a small MSOP–10 package.

The catheter pads are located on the top (pressure) and bottom (volume) of the PCB. The interface module is inserted at the top of the telemetry system stack allowing the catheter wires to directly solder on. As a result, only header connectors are soldered on to this PCB. The IQ and pressure outputs are directed to the communications bus to be processed by the microcontroller and then to the end device.

**Testing / Programming Board – Physical Construction:** Two additional PCBs are created for testing and programming purposes, Fig. 4.12. Both of these boards can only be placed at the top of the stack due to only containing header vertical connectors. The testing PCB, Fig. 4.12(b), contains two right angled through hole headers, 6 and 7 pins each. These pins are attached to the vertical bus to measure power consumption, battery voltage, and have access to the input/output pins on the microcontroller. The programming PCB, Fig. 4.12(a) contains a single 6 pin through hole receptacle which is connected to the external USB programming device. Only a single extra board may be used at a time, either programming or testing as they are attached at the top of the stack.

**Vertical Connectors – Physical Construction:** As discussed in Section 3.4.1 the vertical connectors in this system contain a total of 32 pins. The physical connector must have specific design requirements to fit in the telemetry system. The connector must be small in size, fine pitch, low mated height and a simple mating system. The first design specification used to select a connector is the width of the boards. The connector has to be less than 15 mm, as to not extend out from the stack and it has to have a minimum width to maximize component

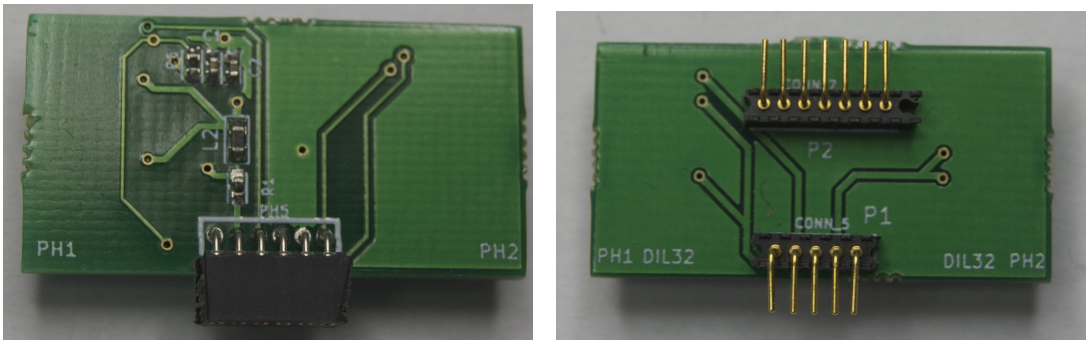


(a) Programming Board – Top (b) Testing Board – Top

Figure 4.12: Interface Module – prototype 1 PCB layout.

space. In order to increase the pin count of the connector, a fine pitch connector is needed. There is a trade off between the pitch and the overall physical size of the connector. When the pitch increases (i.e., becomes finer) the overall physical size becomes larger. This is due to the extra housing needed for the header to fit in. A mated height of less than 5 mm is needed to reduce overall height of the structure but still provide adequate clearance for components. The connectors must also be able to be physically removed easily without additional force, as to not damage the connectors.

Taking all the above requirements into account the Samtec CLE (receptacle) [86] and FTE (header) [87] series of connectors are chosen for this design. These connectors are 3.18 mm wide by 12.8 mm long with a mated height of 4.09 mm. They feature dual 0.8 mm pitch 16 pin rows for a total of 32 pins per connector. Single row connectors were also investigated however, to obtain the required pin count the size increase was not justifiable as well as most connectors of this micro–pitch do not come in single row designs.

Headers and receptacles are placed on the micro and RF PCBs to allow for interchangeability. Only receptacles are added to the power module as it is placed in the bottom of the stack. On the other hand, only headers are added to the interface, testing and programming modules as they are placed at the top of the stack. Additional modules can be connected to the communication bus as long as the connectors are placed in the same positions and the pinout is followed.

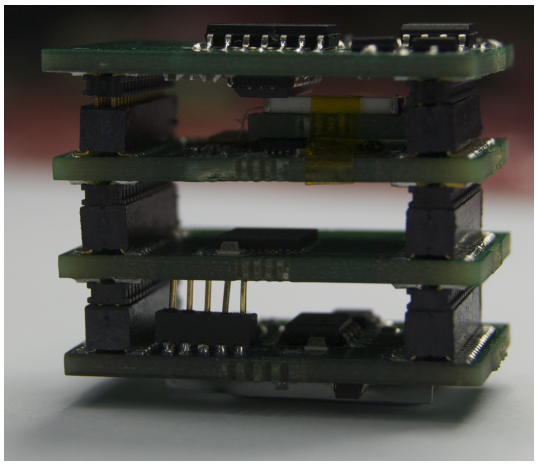

Figure 4.13: Fully assembled prototype 1.

**Overall Assembly – Prototype 1:** The overall system is assembled with each module placed on top of each other, with the stackup from top to bottom as follows: interface module, RF module, microcontroller module, and power module. The system including the battery is 15 mm x 30 mm x 24 mm with a total volume of 10.8 $cm^3$. Between each module there is a $\sim$5 mm space to allow for proper airflow and component clearance. The final assembled wireless telemetry system is shown in Figure 4.13.

### 4.2.2 Phase 2 – Prototype

Using the first prototype as a foundation to build upon, an improved experimental model of a wireless telemetry system is developed. The main motivation to develop a second prototype is to further miniaturize the telemetry system for future implantable use. In addition, this new prototype would consume less power and provide further testing and optimization opportunities.

The new prototype features eight four layer 15 mm x 15 mm PCBs that are built using 0.4 mm thick FR-4 substrates. Major changes to the physical structure of this prototype are made in comparison to the initial physical design. Some of these changes include all passives components being 0201 sized, new vertical communication bus connectors, both volume measurement techniques included, and a full debugging interface is designed and implemented.

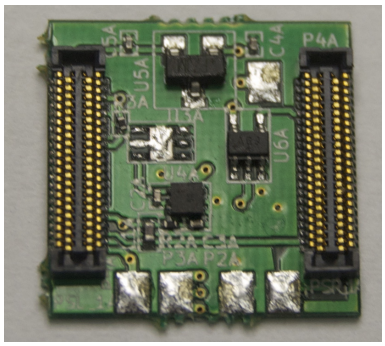


Figure 4.14: Power Module – prototype 2 PCB layout.

Each module's physical construction will be discussed in detail in the following sections.

**Power Module – Physical Construction:** The second revision of the power board contains all the main sub–blocks found in the original design however with some modifications. These modifications include a different battery, different packaging, and the addition of new components. The ICs and passives are located on the top side of the PCB and leaving the battery to be located on the bottom, Fig. 4.14.

The new battery is chosen to fit exactly in the desired board dimensions 15 mm x 15 mm. As mentioned in Section 3.1.1 the new battery does have an increased volume however this provides an increased capacity to 40 $mAh$. The battery is soldered on to the bottom of the PCB using two wires and is glued on for stability purposes.

The packages of the supervisor device and the voltage regulator are changed in this version. In the previous design, these ICs came in larger packages such as SOT-23 and a 8 pin VSSOP which are not suitable for the smaller size telemetry system. Therefore, new packages are chosen which minimize the physical footprint and still keep the overall functionality. The same supervisor IC that is found in the first prototype is also available in a no lead package. The new fixed LDO regulator (TI TLV70036) also comes in a small 1.5 mm x 1.5 mm no lead package and does not require additional resistors to control the output voltage, further reducing the overall size and component count.

Two additional components are added to the power module in this prototype, the voltage

reference and the analog switch. The 1.8 V voltage reference was originally located on the interface module however, it is relocated to the power module to consolidate all power electronics in one central location. The 1.8 V reference output is connected to the communications bus for every module to access. This component is still in a SOT-23 package. The second new component to be located on the power PCB is the analog switch, MAX4714. This IC is connected to the communications bus turning off and on the interface module power. The MAX4714 comes in a SC70-5 package allowing it to fit into the available PCB space as well as not needing any external passives to operate. In this version of the telemetry system the USB charging IC is removed from the power module and moved to the external development board. The large SOIC-8 package of the MAX1811 does not fit into the allowable design space of the PCB as well as connecting an external cable to these small PCBs is not recommended. Furthermore, the space restrictions also removed any physical switch for controlling the power to the system. The battery is now fixed to the PCB powering at least the voltage regulator, supervisor IC, voltage reference and analog switch. However, these components have very low current consumption sub $\sim 5\ \mu A$ and is still taken into consideration in power measurements.

Additional test pads are added to the power module to provide testing and fail safes to the system. Three test pads are added to test the main power supply voltage, ground and the 1.8 V voltage reference. These pads are added to test the power module directly without the external development board. Two additional pads provide direct access to the battery for charging purposes. These pads are added to provide charging access to the battery if the vertical bus happens to fail. It should be noted that an external charging PCB should be used if the battery is charged using this method. If voltage is directly applied, the battery may be damaged.

**Microcontroller Module – Physical Construction:** The second prototype of the microcontroller module contains the same MSP430F2274 that is in previous version along with the new headers and receptacles that are inserted into the main stack, Fig. 4.15. There is no longer a LED for testing as size and power restrictions do not allow this component to placed in the 15

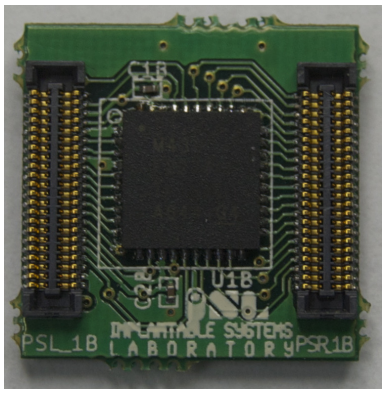


Figure 4.15: Microcontroller Module – prototype 2 PCB layout.

mm x 15 mm PCB area. However, multiple LEDs are located on the development board for testing purposes.

**RF Module – Physical Construction:** In this prototype the RF module underwent significant changes to the components used in this design, Fig. 4.16. Major changes are made on the balun/matching network, RF antenna, and a smaller crystal is used.

In the previous prototype the balun and matching network are created using 11 passive components (8 capacitors and 3 inductors). These components are 0402 sized and do not take up much space in the previous prototype as the size of the boards are larger. However, when miniaturizing the system even further the balun and matching network has to be redesigned. Various options were researched such as using 0201 components to create the same balun/matching network as was previously done, creating a custom ceramic device using LTCC technology to achieve the matching and finally looking at other commercial options available. Using 0201 components would reduce the overall area as smaller passive devices are used however, the component count is still the same which is not desirable. A custom ceramic device is also not recommended as it is very costly to manufacture and is not desirable for high yield systems. Finally, commercial solutions were researched and the Anaren BD2425N50ATI [88] is chosen to replace the existing balun/matching network structure.

This new component replaces the previous balun/matching networking with a single 1.05

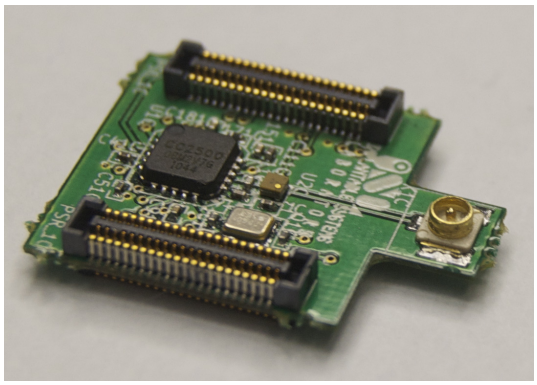

Figure 4.16: Radio Module – prototype 2 PCB layout.

mm x 1.05 mm x 0.65 mm mutli–layer ceramic structure and 2 external passive components. The extremely miniature size and low external components are the main reasons that this design is chosen. The Anaren balun along with 2 external components, 10 nH inductor and 5.6 pF capacitor, is designed specifically for the CC2500 RF transceiver used in the RF module's architecture. It is made to convert the balanced output impedance of the CC2500 to an intermediate unbalanced impedance and then convert it to 50 Ω to be connected to a RF antenna. The steps to convert the 50 Ω antenna impedance to the balanced input/output impedance of 80+j74 Ω as outline in [88] are: 1) the 50 Ω connector and trace are attached to the Anaren balun, which directly transforms the impedance to 127 + j34 as noted in the specifications of the device. 2) The added 10 nH inductor at the differential output of the BALUN converts the 127 + j34 Ω to 76 + j66 Ω. 3) The connecting differential trace to the CC2500 converts the impedance to 83 + j87 Ω. 4) The DC blocking capacitor, 5.6 pF coverts the overall impedance to 89 + j86Ω. This impedance is slightly off of the optimum differential impedance of the CC2500, which causes a negligible loss in overall performance. This possible performance loss is a tradeoff of the minimization of the size and area of the circuit. The overall space savings from the initial 0402 passive balun and matching network to the new ceramic solution is approximately 84% [88].

The second major change in the physical construction of the RF module is the addition of an RF connector. Previously, a fixed 50 Ω 2.4 $GHz$ antenna was used. This allowed for direct

communication to occur however, it had some drawbacks. First, it is fixed on the antenna PCB and does not allow for very much movement to the antenna itself. Secondly, it did not allow different antennas to be tested to determine optimal physical design for implantable systems. Finally, the previous antenna is too large to fit into the new miniaturized design. Therefore, a new RF connector is added to the system rather than a specific fixed antenna. The TE Ultraminiature Coax Connector (UMCC) [89] is chosen to be the new RF connector. The main reason this connector is chosen it's small PCB footprint of 3 mm x 3 mm and also can interface with any type of antenna. The UMCC can interface with various larger connectors such as SMA, BNC, etc using 50 Ω adapter cables. Currently, for testing purposes this is attached to a SMA connector with a 2.4 $GHz$ pigtail antenna. A full antenna study is to be undertaken where the optimal antenna for implantable applications will be found.

The 26 $MHz$ crystal is also changed to a smaller package. The new package is 2 mm x 1.6 mm (3.2 $mm^2$) which 5 times smaller in area than the previous crystal (5 mm x 3.2 mm or 16 $mm^2$). The same CC2500 package is used in this prototype, 20 pin no–lead package, along with the new headers and receptacles to connect to the main stack. As this is an RF layout, extra care is taken when laying out the components along with proper grounding procedures. In addition, the trace connecting the ceramic balun to the RF connector is designed to be exactly 50 Ω based the physical PCB parameters provided by the PCB manufacture. The entire RF module is designed in the 15 mm x 15 mm however, an extension is made to allow the mated height (2 mm) of the RF connector to not interfere with the internal clearance of the stack.

**Interface Module – Physical Construction:** Two interface modules are constructed in this prototype: one with the lock–in method for volume measurement and analog pressure trimming and a second module using the magnitude and phase method for volume measurement and digital pressure trimming.

*Interface Version 1 – Lock–in with analog resistive trimming:* The interface module is designed with the prior knowledge from the first prototype, this includes component choices

and board size. Rather than extend the area of a single printed circuit board it is more beneficial to extend the design to two separate PCBs. This increases the overall volume slightly however, it does not change the shape of the system, as it still remained cubic shaped. Design decisions are made on how to separate the design across two PCBs, this includes which signals are connected to the communications bus, which packages are used, and where the catheter pads are located. In addition, this module's power supply is controlled by the analog switch located on the power module.

In the original prototype the catheter pads are located on the top and bottom of the PCB. This is inconvenient when attaching a catheter and could cause the catheter wires to break during movement. Therefore, it is recommend to have them attached on the top of the first PCB on the stack. This allows the catheter to be attached with no physical issues. The second critical design decision that is made is which packages and components are used. In the initial prototype Analog Devices AD8607 and AD8609s are used. It was discovered that due to their low power consumption, they do not provide a high enough slew rate to create the oscillations required by the quadrature oscillator. In most cases when choosing OP-Amps with high slew rate they generally have higher current consumption. As this design is an implantable system, if at all possible the lowest current consumption amplifiers should be chosen that still achieve the correct slew rate. National Semiconductor LMV554 OP-Amps are chosen. These operational amplifiers consume an average of 37 $\mu A$ of current, work in the designed voltage supply range and are available in single, dual and quad packages. Another major component change from the previous prototype is the addition of a dedicated instrumentation amplifier. In the previous prototype, two discrete OP-Amps along with precision resistors are used to create the instrumentation amplifier. The reason for this is to reduce active and passive component count. However, in practice this is not ideal and a dedicated instrumentation amplifier with high gain and high CMRR is used instead, TI INA2332. The dual analog switch from the previous prototype is still used.

As interface module is split across two PCBs multiple signals are to be routed to the com-

munication bus to be connected to the second PCB in the stack. When choosing which signals are to be connected, the physical packages of the components are considered. In this design, there are a total of 12 OP-Amps, 2 IAs and 2 switches that are used by the lock–in and analog pressure sections. The OP-Amps can be split up into different combinations of quad and dual packages (i.e., 3 quads or 2 quads and 2 duals, etc). In addition, all pressure components should be on a single PCB not split up, as well the instrumentation amplifier used by the pressure circuit is located in a dual packaged shared with the volume section. Therefore, taking these considerations and analyzing the schematic to view logical separation points it is determined that three signals are used for separation purposes, I-Gate, Q-Gate and INA Out, and one output, pressure. I-Gate and Q-Gate represent the output of the comparators to create the Lock–In reference signals for the I and Q signal chains. The signal INA Out represents the signal taken from the output of the instrumentation amplifier in the volume section. In addition to the three separation signals, output pressure is also sent to the communication bus to be digitized by the microcontroller for transmission.

Using these three signals along with output pressure the interface module is split into two PCBs created by using a total of six packages. The first PCB contains three packages: 1 quad OP-Amp, 1 dual OP-Amp and a dual instrumentation amplifier. The second PCB contains three packages as well: 1 quad OP-Amp, 1 dual OP-Amp and 1 dual analog switch. The complete pressure section is located on the top PCB along with the catheter pads. The second PCB contains the outputs I and Q which are connected to the microcontroller through the communications bus. The two PCBs are fabricated using the same 15 mm x 15 mm FR-4 boards as the previous modules and are shown in Fig, 4.17(a) and Fig 4.17(b) for the first and second board, respectively.

*Interface Version 2 – Magnitude and Phase method with digital resistor trimming:* This interface module contains all the magnitude and phase electronics required for volume measurement along with pressure electronics with digital resistive trimming capabilities. As this design is not implemented in the previous prototype a new design is created. Along with the

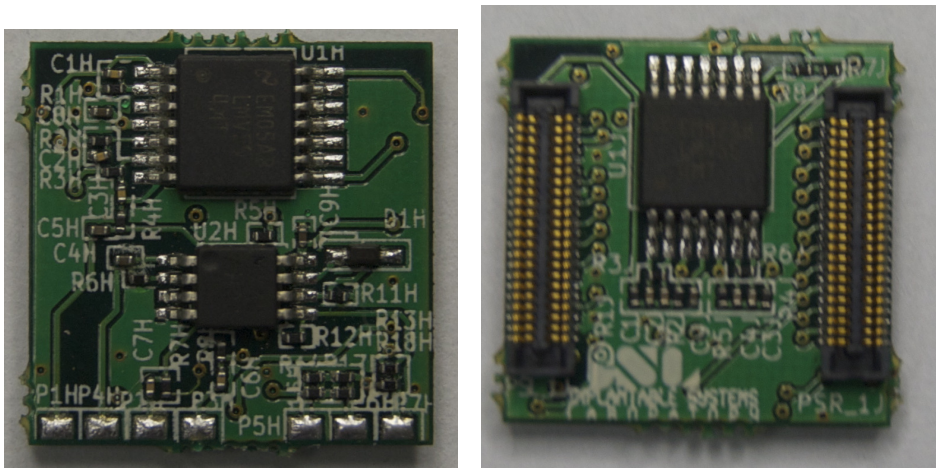


(a) First PCB (b) Second PCB

Figure 4.17: Interface Module Lock–In method – prototype 2 PCB layout. (a) first PCB (b) second PCB.

Lock–in version, this interface module is separated into two separate PCBs. By using the same design methodology of the Lock–In version, specific signals are chosen for separation along with using smallest packages for each major component.

As with the previous version, the catheter pads are chosen to be located on the top of the first PCB to ensure a strong connection. This implementation of the interface board contains a total of seven operational amplifiers with six using the same LMV554's as utilized in the Lock–In version. The Op–Amp used in the envelope detector requires a higher slew rate to track the incoming rectified signal therefore, the LMV651 is chosen to achieve this. The LMV651 is the class above the LMV554, consumes an average of 112 $\mu A$, and is packaged in a SOT-23. Two instrumentation amplifiers are required, one each for the pressure and volume electronics. The INA333 is chosen to implement this function. The INA333 is a single IA that consumes 50 $\mu A$ of current and is packaged in a small no–lead package. The main reason for choosing this IA is the minimal package size. As noted in Section 3.5.2 the MAX5484 is used in the pressure section for digital resistor trimming and is contained within a no-lead package. In addition, dedicated comparators, TLV3402 (MSOP-8), are used in the phase detection.

Following the procedure used in the Lock–in implementation, the boards are separated using connecting signals through the communications bus. Two signals are used along with

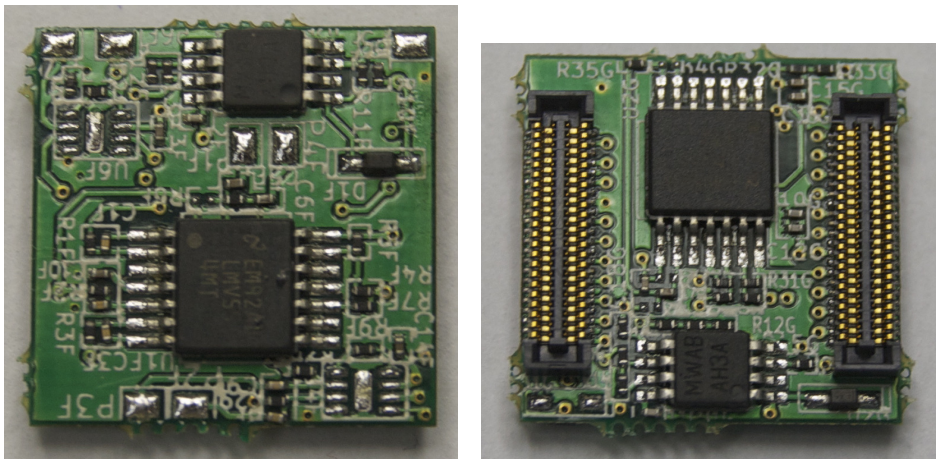

(a) First PCB (b) Second PCB

Figure 4.18: Interface Module Magnitude and Phase method – prototype 2 PCB layout. (a) first PCB (b) second PCB.

one output on the first board, sine, gain out and output pressure. The Sine signal represents the sine output from the quadrature oscillator and the gain out signal is taken from after the IA gain stage in the volume electronics. The output pressure is provided to the microcontroller through the communication bus.

By taking into account the two separation signals along with the output pressure, the interface module can be created using a total of nine packages. The first PCB contains five packages: 1 quad OP-Amp, 1 dual OP-Amp, two single IAs, and a single digital potentiometer. The second PCB contains four packages: 1 quad OP-Amp, 1 dual OP-Amp, a single high speed OP-Amp, and 1 dual comparator package. The complete pressure section is located on the top PCB along with the catheter pads. The second PCB contains the outputs magnitude, heart duty cycle, oscillator duty cycle, and rectifier and ECG out for testing. These signals are connected to the microcontroller through the communications bus. The fabricated printed circuit boards are shown in Fig 4.18(a) and Fig 4.18(b) for the first and second board, respectively.

**Vertical Connectors – Physical Construction:** With the miniaturization of the second prototype, new connectors are required to facilitate the increased pin count, reduced height and smaller footprint. The previous connectors have a much larger footprint with a mated height of

$\sim$ 5 mm. This height is drastically reduced to miniaturize the telemetry system even further. New Molex micro–connectors [90] [91] are chosen to serve as the vertical connectors in this prototype. These headers and receptacles are much smaller than the previous connectors with a size of 1.54 mm x 10.26 mm (15.8 $mm^2$) and a mated height of 1.5 mm with a total of 44 pins at 0.4 mm pitch. The mated height of 1.5 mm is the minimum height to allow for proper clearance for ICs located above and below the specific module. The new micro–miniature connectors provide a physical area savings of 61% compared to the previous connectors (40.70 $mm^2$).

**Debugging Interface:** The first prototype features two printed circuit boards that are added to the vertical stack to be used for programming and testings purposes. This design is modified for the the second prototype as the size of the overall system is much smaller and does not allow for debugging to be completed directly on the system. Instead, a new testing system is developed to allow for full programming, charging, and debugging of the wireless telemetry system. This system consists of two PCBs, a breakout board and a full featured development board.

The breakout board's main purpose is to route all the signals from the communication bus to two additional connectors. These connectors are located on the opposite ends of the board compared to the vertical communication bus, Fig. 4.19(a). Flat flex connectors (FFC) are chosen for the breakout connectors, more specifically 26 pin 0.5 mm pitch Molex FFC connectors [92]. These are right angle flat cable connectors with a mated height of 2 mm. The overall PCB size is increased to 25 mm x 21 mm to facilitate the new FFC connectors and avoid all clearance issues associated with the increased mated height and the system stack. Two identical FFC connectors are placed on the development board to transfer the signals from the vertical bus to the development board. Flat flex cables, 0.305 m, are used for this connection. No additional components are placed on this PCB, only the two FFC connectors and the vertical connectors. The breakout board provides only signal routing to the development board and

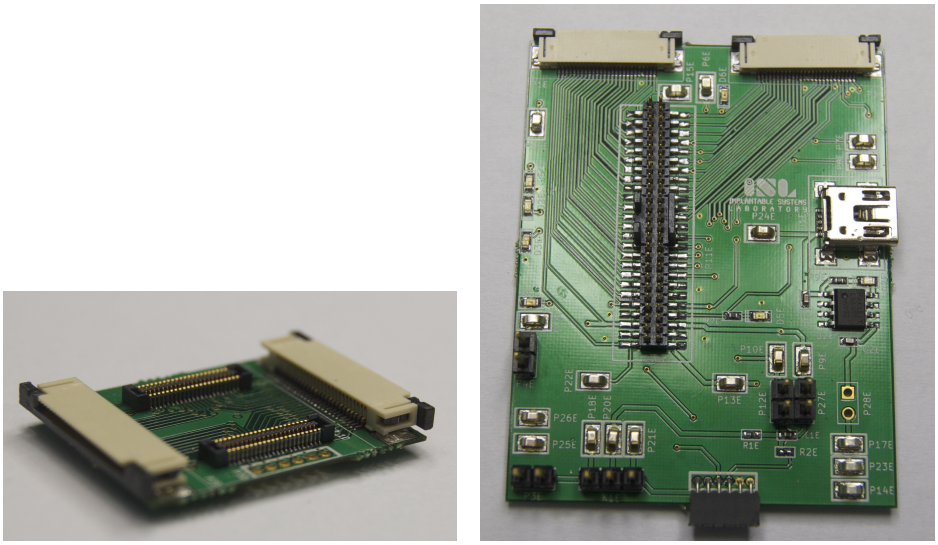

(a) Breakout Board (b) Development Board

Figure 4.19: (a) Breakout board and (b) Development boards of the second physical prototype.

serves no other functional purpose inside the system stack.

The second board in the debugging interface is a much larger PCB (60 mm x 47 mm) which contains programming, charging and debugging capabilities. This PCB receives the communication bus signals from the FPC cables and distributes them to various sections of the boards, Fig. 4.19(b). These sections are separated into battery charging, power management, USB programming, and testing components.

The battery charging is located on the development board rather than the power board in this prototype due to size restrictions as noted in above sections. A mini USB connector is added to the PCB to provide a direct connection to USB power for the MAX1811. Test pins are provided to test the input voltage from the USB connector and the output voltage of USB charging IC. This power signal is routed directly to the FFC connectors and directly connects to the external battery to charge it. An LED is also used to indicate when the battery is being charged.

Power management and testing functionality is also designed into the development board. The main telemetry system can be powered through the attached battery or by the development board in testing. The power signals are routed to test points along the PCB to test for correct

voltages for the system voltage, interface voltage and 1.8 V reference. Another design feature of this PCB is enabling an external power connection to the development board, which in turn can power the whole system without the use of a battery. This feature is extremely important in testing and debugging the system as precise current consumption can be calculated. All three main telemetry system voltages can be applied externally through custom 2 pin connectors located on the PCB. Additional connectors are added to switch between battery power and external power as to not damage the electrical components.

A programming interface is also provided on the development board. The programming of the MSP430 is achieved through at the same 6 pin connector as used in the previous prototype. The programming interface also provides external power to the system and must be disconnected from any additional power source when connected.

Finally, multiple debugging connections are added to the PCB. There are a total of six LEDs which are directly connected to the pins of the microcontroller and can be controlled for testing. Furthermore, test pins are provided for all outputs of the interface module as well as various other inputs and outputs of the microcontroller. Lastly, all the signals from the FFC are also routed to a larger external breakout connector. This is 50 pin connector that is used for additional pin out or connection to an external board. The breakout and development boards provide all the testing functionality to the wireless telemetry system along with USB charging and programming features.

**Overall Assembly – Prototype 2:**

*3D modelling:*

Once the layouts of each board were initially completed, 3D modelling was done to ensure full clearance and mechanical connection. Simple 3D modelling is completed for the first prototype however, size and clearance were not of critical importance, therefore it was only used as an elementary mock–up. On the other hand, 3D modelling plays a major role in the second prototypes design and is modelled to scale.

The second prototype is modelled using SolidWorks 3D CAD software. An additional tool, Read3Di, is used to convert the gerber files from the layout design phase to compatible SolidWorks files. This software allows an exact scale FR-4 substrate model to be created based on the gerber files. The full stack up of gerber layers must be provided along with dialectic and solder layer sizes to create an accurate model. As this prototype uses 0.4 mm thick FR-4 substrate it is crucial that the model be accurate, this includes even the solder pads modelled. Each component is then modelled. Component 3D models are obtained by each manufacture if possible, however, in some cases custom models are created based on the specifications in the respective data sheets. The battery is also modelled based on the data sheet dimensions. Each component is mounted on their specific solder pads and all PCB's are modelled.

As this prototype pushes the limits of discrete components, component clearance is a main design constraint. The mated height of the vertical connectors only allows for 1.5 mm of clearance. This does not create a problem for most 0201 passive components as they are generally only 150 $\mu m$ to 250 $\mu m$ high. However, for active components such as the integrated circuits used in this design, this is a major problem for clearance. Most packaged IC's heights are minimum $\sim$1 mm for most no–lead packages and upwards of 1.1 mm for a TSSOP package. When components are placed on the bottom side of the above board they may interfere physically with the components placed on the PCB below. Initial modelling confirmed that multiple clearance issues did exist. These are mostly found on the dual board interface modules and physical clearance between the RF module and the extended breakout connectors. Therefore, these issues and any other clearance issues found in modelling are dealt with by redesigning the layout of the PCB. This process is repeated until all clearance issues are resolved. A 3D rendering of the fully assembled wireless telemetry system – $2^{nd}$ prototype is displayed in Fig. 4.20(a).

*Assembly:*

Once the 3D modelling ensured clearance and a correct mechanical connection, the overall telemetry system is assembled with each module placed on top of each other, with the stickup

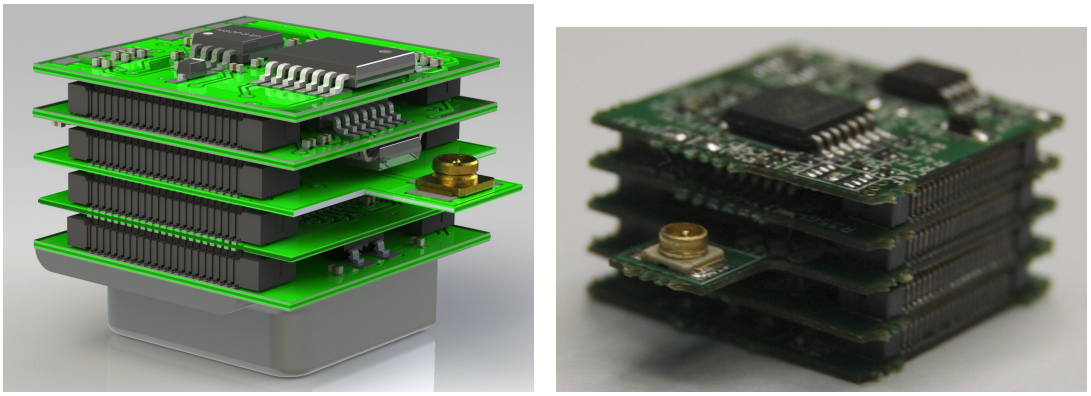

(a) Full 3D rendering (b) Fully assembled prototype 2 without battery

Figure 4.20: (a) Full 3D rendering of assembled wireless telemetry system with battery and lock–in method interface boards; (b) Fully assembled prototype 2 without battery attached.

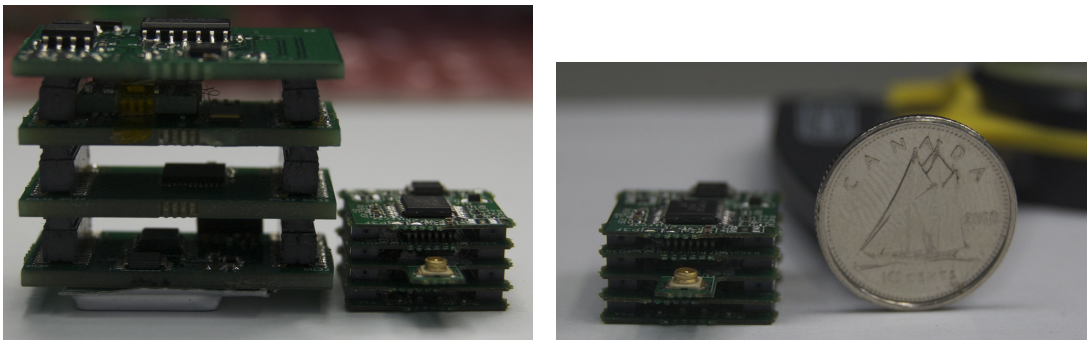

(a) Prototype 1 vs Prototype 2 (b) Prototype 2 vs Canadian Dime

Figure 4.21: (a) Comparison – prototype 1 on the left and 2 (without battery) on the right (b) Prototype 2 vs Dime size comparison.

from top to bottom as follows: interface module board 1, interface board 2, RF module, microcontroller module and, power module. The system including the battery is 15 mm x 15 mm x 11 mm with a total volume of 2.475 $cm^3$. Between each module there is a $\sim$1.5 mm space to allow for proper airflow and component clearance. During testing the breakout board is added to the stack to connect the communications bus to the development board. To ensure full clearance the breakout board must be connected directly above the power module to allow for clearance between the breakout and RF boards. The final assembled wireless telemetry system is shown in Figure 4.20(b), comparing it to the 3D rendering.

Table 4.4: Comparison of relevant works

| **Functions** | **Uemura [36]** | **Raghavan [35]** | **Cong [1]** | **Prototype 1** | **Prototype 2** |
|---|---|---|---|---|---|
| Sensor Type | PV | PV | Pressure | PV | PV |
| Size | – | Interface Board<br>17.67 $cm^2$ | Dia – 6.4 mm<br>L – 4 mm | L = 30 mm<br>W = 15 mm<br>H = 24 mm | L = 15 mm<br>W = 15 mm<br>H = 11 mm |
| Weight | 26 g | 27 g | 330 mg | 11.50 g | Without Battery –2.67 g<br>With Battery – 4.01 g |
| Battery Size | Li–ion | 625 mAh | No Battery | 25 mAh | 40 mAh |
| Power Consumption | Unknown | Active – 151.2 $mW$<br>Standby – 79.2 $mW$ | 300 $\mu W$ | Active 57.72 $mW$<br>Standby – 37.74 $mW$ | Power Module<br>130.5 $\mu W$ |
| Volume Type | Conductance | Admittance | – | Admittance | Admittance |

### 4.2.3 Comparison – Prototype 1 vs Prototype 2

The second prototype not only reduced the overall size of the wireless telemetry system but it also increased functionality. The volume from the first prototype to the second is reduced by 77%. This is attributed to the minimal PCB substrate used at 0.4 mm along with reductions in mated connector height from 5 mm to 1.5 mm. Additional size reductions are found from using smaller passive components 0201 compared to 0402 and switching to no–lead packages whenever possible. Further functionality is added from the modular RF connector and the designed development board. Physical comparisons are shown in Fig 4.21(a) where the second prototype is compared with the first. As the represented in Fig 4.21(a), the second prototype is much smaller than the initial prototype and is even smaller than a Canadian dime, Fig. 4.21(b). A comparison of this work with relevant previous works is shown in table 4.4. This work is smaller than the previous two pressure volume implantable telemetry systems, however is larger than Cong's pressure only version.

**Future Bio-Compatible Capsule Rendering:**

Future bio–compatible shell renderings are created for both prototypes. As with the other 3D models designed for the first prototype the shell design is also very simple. The capsule houses the first prototype along with a future wireless power solution, Fig. 4.22(a). The second prototype's capsule is designed specifically to house this prototype. The capsule contains two access connectors, these attach the catheter and the external antenna, Fig 4.22(b). These

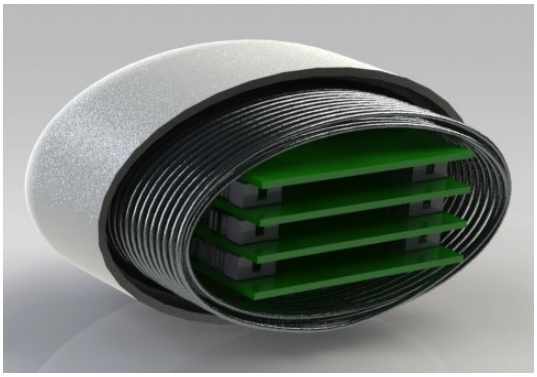

(a) Preliminary rendering of capsule design – prototype 1

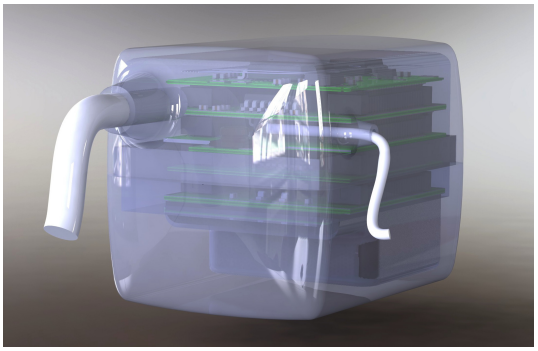

(b) Preliminary rendering of capsule design – prototype 2

Figure 4.22: Future bio-compatible capsule renderings

capsules would be located inside the test animal's body with the catheter placed in the left ventricle. A separate study is being preformed on bio–compatible materials and other possible capsule designs to optimize the design for the designed wireless telemetry system.

## 4.3 Preliminary Experimental Testing

The prototypes are experimentally tested for power consumption, wireless range, and wireless communication. The first prototype is tested fully and the second prototype is only preliminarily tested with future plans for a full characterization study to be completed.

The prototypes are tested using state–of–the–art equipment with a specific test plan to ensure proper documentation of results. The power modules are tested using a Keithley Battery simulator. This device allows a Li–Poly battery to be emulated along with instantaneous current to be recorded. During power consumption tests this is attached to the battery solder terminals on the PCB rather than the Li–Poly battery. In addition, a 6.5 digit multimeter is used to measure any DC voltages or resistances in testing of the electronics. The first prototype's power module is initially powered without connecting to the main stack. The power consumption recorded by the battery simulator with a set battery voltage of 3.7 V is 17.76 $mW$. The majority of the power consumption of the power module is from the LED that is used

to indicate if the module is powered, the regulator and supervisor ICs attribute to less than a $mW$ to the overall power consumption of the power module. When connected to the full stack with the microcontroller running in a timing loop where analog data is acquired by the ADC from the internal temperature sensor, digitized and sent to an end unit every 1 sec with the RF electronics set to an output power of -12 $dBm$, and the interface electronics attached, the power consumption increased to 57.72 $mW$ during transmission and 37.74 $mW$ when not acquiring and transmitting data. The second prototype's power consumption is tested on the power module only with a power consumption of 130.53 $\mu W$. The full power consumption of the second prototype will be tested in future work with the results being published in journal publications.

The microcontroller module is tested by creating small test programs to evaluate specific functions of the microcontroller. Although intended for testing the first prototype, these test procedures work on the second prototype with slight modifications. These programs are written in the MSP430 assembly language and programmed to the MSP430 through the IAR Embedded Workbench. The first program created is a simple LED test program, to light up an LED. A second program is created to test the SPI bus between the microcontroller and RF transceiver. Finally, a main test program is created to initiate communication with the transceiver, write the RF modulation and power settings to the transceiver and to send data every few seconds using the built in timers. More extensive microcontroller programs written in C will be created for the second prototype along with further improvements to power management and data transmission.

The RF module of the first prototype is tested using a spectrum analyzer. This is used to test the output power along with viewing the frequency spectrum of the transceiver. Simple distance measurements are also performed to determine the range of the SMD antenna used in the first prototype. The first prototype is able to achieve a range of $\sim$30 m with a direct line of site. A sample output spectrum of the RF module with a distance of 10 cm and a constant data stream output with an output power of 0 $dBm$ from the RF transceiver is shown, Fig. 4.23. The received power level is -50 $dBm$ at a centre frequency of 2.433592 $GHz$. The second

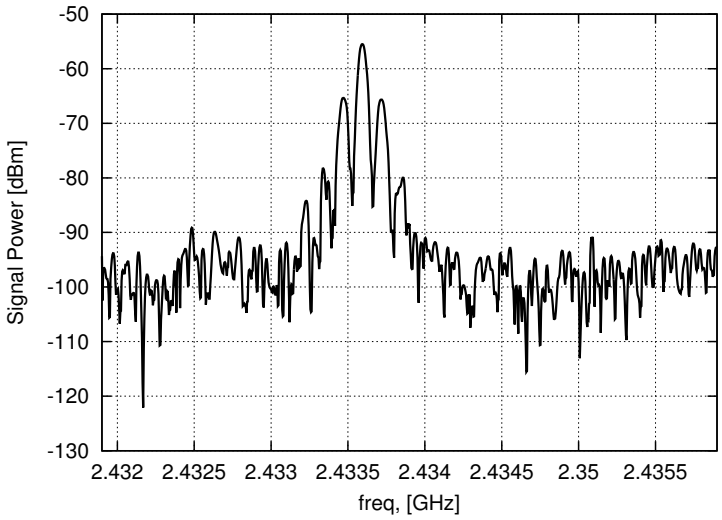


Figure 4.23: Frequency spectrum of RF transmission output at 10cm distance and 0 $dBm$ input power. $F_{centre}$ = 2.433592 $GHz$.

prototype will undergo a full antenna study to determine the best antenna to use for biomedical applications and the same test equipment will be used to determine output power, frequency spectrum, and modulation used.

The interface module from the first prototype is tested using a digital sampling scope. This allows the outputs of the Lock–in amplifier, I and Q, to be measured and recorded with high precision. It was determined that due to the low slew rate of the OP-Amps used in the initial design of the quadrature oscillator, oscillations did not occur. This failed to create the excitation signal for the interface module. Both outputs of the oscillator along with the power supply and virtual ground terminals were also measured. Therefore, during this testing stage of the first prototype it was determined that the interface board needed modifications to operate properly. These modifications included selecting new high speed operational amplifiers and modifying the structure of the instrumentation amplifier, listed in detail in Section 4.2.2. With these modifications included, it is estimated that the full characterization of the second prototype will include results from the interface boards that are comparable with the simulation results listed in Sections 4.1.1 and 4.1.2. Future in-vivo testing is planned once full characterization of the second prototype is completed. This will indicate areas of improvement to the implantable

system that would be included when further miniaturizing the system.

## 4.4 Summary

In this chapter two physical prototypes of an implantable wireless telemetry system are developed. These prototypes are based on the architecture designed in Chapter 3. The complete assembly and 3D modelling was also discussed. The first prototype's size including the battery is 15 mm x 30 mm x 24 mm with a total volume of 10.8 $cm^3$ and the second prototype was miniaturized even further creating a new improved implantable system with the dimensions 15 mm x 15 mm x 11 mm (including the battery) and a total volume of 2.475 $cm^3$. The second prototype reduced the overall volume by 77%. In addition, future bio-compatible shells are shown that would encompass each prototype for implantation.

Initial simulations were completed on both implementations of the interface module, magnitude and phase and the lock–in method. Behavioural simulations were completed to ensure theoretical operation of the magnitude and phase method and SPICE simulations were performed on the Lock–In implementation. Preliminary experimental testing procedures and results are discussed, Each model's testing is discussed along with improvements to the first prototypes interface module. These physical prototypes demonstrate an implantable wireless implantable system capable of measuring pressure and volume data from laboratory animals.

# Chapter 5

# Conclusion

The aim of this thesis is to design and implement a discrete level prototype of a miniature, short–distance, low–power, RF wireless telemetry system. In correspondence to this goal, a telemetry system architecture based on four modules is created along with two physical prototypes for measuring blood pressure and volume data. This chapter gives a summary of the contribution made by this thesis, plus suggestions on future work.

## 5.1 The Contribution of the Thesis

In this thesis, the following achievements are made:

- A custom telemetry system architecture is designed which is focused on implantable systems. It features four main modules: sensor interface, data and signal processing, RF transmission, and power electronics. It is designed around a low–power microcontroller and RF transceiver, MSP430 and CC2500, respectively and is designed to be modular to allow for future improvements without a complete redesign of the major components. This architecture provides the basis to build miniaturized implants for blood pressure and volume research in small laboratory animals.

- In order to convert the measured signals into absolute blood pressure and volume, a

sensor interface had to be created. Two different implementations of sensor interfaces are developed for the pressure and volume measurements. First, a direct approach is used to extract the measured complex voltage and convert it to Admittance for absolute volume conversion. This is denoted as the magnitude and phase method. Here, the magnitude and phase are extracted directly from the measured waveform using a peak detector and comparators. The advantages of this system are that it is very simple to implement mathematically however, it does rely on the microcontroller for phase measurements. A second improved implementation was developed, the lock–in method, where phase–sensitive detectors are used to extract the low amplitude voltage signal from the environment and produce DC I and Q values. These values are used are then used to calculate the measured admittance to be converted into a absolute volume. The magnitude and phase method is theoretically proven using behavioural level simulations and the lock–in method is simulated using SPICE to validate the results. In addition to the volume circuitries, pressure electronics are also designed using both analog and digital resistive trimming techniques.

- Two physical prototypes were developed that are based on the designed implantable system architecture. The first prototype measures 15 mm x 30 mm x 24 mm with a total volume of 10.8 $cm^3$. This prototype system consumes 57.72 $mW$ of power during ADC acquisition test when having all modules including the sensor interface active. A much smaller implantable system prototype is created to build upon the knowledge gained in the initial physical design. This second prototype is 15 mm x 15 mm x 11 mm with a total volume of 2.475 $cm^3$, or a volume reduction of 77 % from the first prototype. State–of–the–art PCB manufacturing techniques including utilizing PCB FR-4 board thickness of 0.4 mm and minimal track sizes along with the reduction of external components are the main reasons for the miniaturization in size. In comparison to previous works [35], both physical prototypes are smaller in size than the prototype created in [35] with the second prototype being 87.24 % smaller in area than the instrumentation board recored

in [35].

The achievements completed in this thesis create a benchmark to enable further advancement of micro–wireless telemetry systems through the use of a variety of sensors, not limited to cardiac monitoring, as well as allowing for future benefits in eHealth monitoring systems for humans.

## 5.2 Future Work

General trends in this field are leading to increased miniaturization of implanted sensors leading to sub 1 $mm^3$ systems [93] and unique RF techniques such as carbon nanotube radios [94]. These trends among others indicate that this research field continues to improve and create new improved telemetry systems. Therefore, improvements should be made on the current system to further improve pressure–volume implantable telemetry system for small laboratory animals. Based on the preliminary results of this thesis, further miniaturization is required to enable the telemetry system to be implanted in small laboratory animals such as a mouse. To achieve this, a new improved telemetry system will be developed based on CMOS integrated circuit (IC) and system in a package (SiP) technologies. The future work is outlined below

- Full characterization of the second prototype should be completed along with software optimization. In addition, in–vivo testing should be completed to verify experimental results.

- A CMOS 0.13 $\mu m$ integrated circuit of the sensor interface should be tested and developed. This would reduce the sensor electronics area from 225 $mm^2$ to 4 $mm^2$.

- A custom integrated circuit of the RF transceiver should be developed. The power consumption will be optimized specifically for implantable devices, further reducing the systems overall power consumption.

- A custom IC of the processing module should be developed. This processor should be designed only to perform the tasks needed by this specific application, allowing power consumption to be optimized specifically for the low–power requirements of this implantable system.

- Finally, the three subsystems should be integrated using system–in–a–package (SiP) technology provided by the Cadence RF SiP Methodology Kit, enabling the encapsulation of the three ICs (whose volume will be reduced to $\sim$8mm$^3$) into a single biocompatible implantable package. This reduction in volume represents the physical limits of the state–of–the–art semiconductor and packaging technologies.

# Bibliography

[1] P. Cong, W.H. Ko, and D.J. Young. Wireless batteryless implantable blood pressure monitoring microsystem for small laboratory animals. *Sensors Journal, IEEE*, 10(2):243–254, 2010.

[2] B.D. Hoit, S. Kiatchoosakun, J. Restivo, D. Kirkpatrick, K. Olszens, H. Shao, Y.H. Pao, and J.H. Nadeau. Naturally occurring variation in cardiovascular traits among inbred mouse strains. *Genomics*, 79(5):679–685, 2002.

[3] J. Baan, E.T. Van Der Velde, H.G. De Bruin, G.J. Smeenk, J. Koops, A.D. Van Dijk, D. Temmerman, J. Senden, and B. Buis. Continuous measurement of left ventricular volume in animals and humans by conductance catheter. *Circulation*, 70(5):812–823, 1984.

[4] J. Francis, RM Weiss, SG Wei, AK Johnson, and RB Felder. Progression of heart failure after myocardial infarction in the rat. *American Journal of Physiology-Regulatory, Integrative and Comparative Physiology*, 281(5):R1734–R1745, 2001.

[5] Y. Gao, Y. Zheng, S. Diao, W.D. Toh, C.W. Ang, M. Je, and C.H. Heng. Low-power ultrawideband wireless telemetry transceiver for medical sensor applications. *Biomedical Engineering, IEEE Transactions on*, 58(3):768–772, 2011.

[6] P. Dario, M.C. Carrozza, A. Benvenuto, and A. Menciassi. Micro-systems in biomedical applications. *Journal of Micromechanics and Microengineering*, 10(2):235, 2000.

[7] S.B. Lee, H.M. Lee, M. Kiani, U.M. Jow, and M. Ghovanloo. An inductively powered scalable 32-channel wireless neural recording system-on-a-chip for neuroscience applications. *Biomedical Circuits and Systems, IEEE Transactions on*, 4(6):360–371, 2010.

[8] R. Häusler, C. Stieger, H. Bernhard, and M. Kompis. A novel implantable hearing system with direct acoustic cochlear stimulation. *Audiology and Neurotology*, 13(4):247–256, 2008.

[9] E.Y. Chow, A.L. Chlebowski, S. Chakraborty, W.J. Chappell, and P.P. Irazoqui. Fully wireless implantable cardiovascular pressure monitor integrated with a medical stent. *Biomedical Engineering, IEEE Transactions on*, 57(6):1487–1496, 2010.

[10] K. Sagawa, H. Suga, and W.S. Maugham. *Cardiac contraction and the pressure-volume relationship*, volume 480. Oxford University Press New York:, 1988.

[11] H.L. Haber, C.L. Simek, L.W. Gimple, J.D. Bergin, K. Subbiah, A.R. Jayaweera, E.R. Powers, and M.D. Feldman. Why do patients with congestive heart failure tolerate the initiation of beta-blocker therapy? *Circulation*, 88(4):1610–1619, 1993.

[12] M.D. Feldman, P.H. Pak, C.C. Wu, H.L. Haber, C.M. Heesch, J.D. Bergin, E.R. Powers, T.D. Cowart, W. Johnson, A.M. Feldman, et al. Acute cardiovascular effects of opc-18790 in patients with congestive heart failure: time-and dose-dependence analysis based on pressure-volume relations. *Circulation*, 93(3):474–483, 1996.

[13] P. Cong, N. Chaimanonart, W.H. Ko, and D.J. Young. A wireless and batteryless 10-bit implantable blood pressure sensing microsystem with adaptive rf powering for real-time laboratory mice monitoring. *Solid-State Circuits, IEEE Journal of*, 44(12):3631–3644, 2009.

[14] A. Kottam, J. Dubois, A. McElligott, and K.K. Henderson. Novel approach to admittance to volume conversion for ventricular volume measurement. In *Engineering in Medicine*

*and Biology Society, EMBC, 2011 Annual International Conference of the IEEE*, pages 2514–2517. IEEE, 2011.

[15] R.A.M. Receveur, F.W. Lindemans, and N.F. de Rooij. Microsystem technologies for implantable applications. *Journal of Micromechanics and Microengineering*, 17(5):R50, 2007.

[16] T. Stieglitz. Implantable microsystems for monitoring and neural rehabilitation, part i. *Med Device Technol*, 12:16–18, 2001.

[17] W. Mokwa and U. Schnakenberg. On-chip microsystems for medical applications. In *Proc. Microsystem Symp.(Delft)*, pages 69–75, 1998.

[18] Y.C. Shih, T. Shen, and B. Otis. A 2.3$\mu$w wireless intraocular pressure/temperature monitor. In *Solid State Circuits Conference (A-SSCC), 2010 IEEE Asian*, pages 1–4. IEEE, 2010.

[19] JFL Goosen, D. Tanase, and PJ French. Silicon sensors for use in catheters. In *Microtechnologies in Medicine and Biology, 1st Annual International, Conference On. 2000*, pages 152–155. IEEE, 2000.

[20] A. Schneider, T. Stieglitz, W. Haberer, H. Beutel, and J. Meyer. Flexible interconnects for biomedical microsystems assembly. In *34th Int. Symp. Microelectronics IMAPS, Baltimore, MD*, 2001.

[21] A. Sivard, P. Bradley, P. Chadwick, and H. Higgins. The challenge of designing in-body communications. *Embedded Systems Programming*, 17(11):20–28, 2004.

[22] Z. Yang, W. Liu, and E. Basham. Inductor modeling in wireless links for implantable electronics. *Magnetics, IEEE Transactions on*, 43(10):3851–3860, 2007.

[23] M. Ghovanloo and K. Najafi. A wireless implantable multichannel microstimulating system-on-a-chip with modular architecture. *Neural Systems and Rehabilitation Engineering, IEEE Transactions on*, 15(3):449–457, 2007.

[24] N.M. Neihart and R.R. Harrison. Micropower circuits for bidirectional wireless telemetry in neural recording applications. *Biomedical Engineering, IEEE Transactions on*, 52(11):1950–1959, 2005.

[25] M.M. Ahmadi and G.A. Jullien. A wireless-implantable microsystem for continuous blood glucose monitoring. *Biomedical Circuits and Systems, IEEE Transactions on*, 3(3):169–180, 2009.

[26] S. Smith, TB Tang, JTM Stevenson, BW Flynn, HM Reekie, AF Murray, AM Gundlach, D. Renshaw, B. Dhillon, A. Ohtori, et al. Miniaturised drug delivery system with wireless power transfer and communication. In *MEMS Sensors and Actuators, 2006. The Institution of Engineering and Technology Seminar on*, pages 155–162. IET, 2006.

[27] P. Basappa Khannur, Kok Lim Chan, Jia Hao Cheong, Kai Kang, A. Astuti Lee, Xin Liu, Huey Jen Lim, K. Ramakrishna, and Minkyu Je. A 21.6 $\mu w$ inductively powered implantable ic for blood flow measurement. In *Solid State Circuits Conference (A-SSCC), 2010 IEEE Asian*, pages 1 –4, nov. 2010.

[28] RC Turner, RR Holman, CA Cull, IM Stratton, DR Matthews, V. Frighi, SE Manley, A. Neil, K. Mcelroy, D. Wright, et al. Intensive blood-glucose control with sulphonylureas or insulin compared with conventional treatment and risk of complications in patients with type 2 diabetes (ukpds 33). *lancet*, 352(9131):837–853, 1998.

[29] T. Karacolak, A.Z. Hood, and E. Topsakal. Design of a dual-band implantable antenna and development of skin mimicking gels for continuous glucose monitoring. *Microwave Theory and Techniques, IEEE Transactions on*, 56(4):1001–1008, 2008.

[30] T. Karacolak, R. Cooper, and E. Topsakal. Electrical properties of rat skin and design of implantable antennas for medical wireless telemetry. *Antennas and Propagation, IEEE Transactions on*, 57(9):2806–2812, 2009.

[31] M.W. Baker and R. Sarpeshkar. Feedback analysis and design of rf power links for low-power bionic systems. *Biomedical Circuits and Systems, IEEE Transactions on*, 1(1):28–38, 2007.

[32] A. Kumar, S. Mirabbasi, and M. Chiao. Resonance-based wireless power delivery for implantable devices. In *Biomedical Circuits and Systems Conference, 2009. BioCAS 2009. IEEE*, pages 25–28. IEEE, 2009.

[33] E.K.F. Lee. An inside body power and bidirectional data transfer ic module pair. *Solid-State Circuits, IEEE Journal of*, (99):1–1, 2010.

[34] H. Fassbender, W. Mokwa, M. Gortz, K. Trieu, U. Urban, T. Schmitz-Rode, T. Gottsche, and P. Osypka. Fully implantable blood pressure sensor for hypertonic patients. In *Sensors, 2008 IEEE*, pages 1226–1229. IEEE, 2008.

[35] K. Raghavan, M.D. Feldman, J.E. Porterfield, E.R. Larson, J.T. Jenkins, D. Escobedo, J.A. Pearce, and J.W. Valvano. A bio-telemetric device for measurement of left ventricular pressure–volume loops using the admittance technique in conscious, ambulatory rats. *Physiological Measurement*, 32:701, 2011.

[36] K. Uemura, T. Kawada, M. Sugimachi, C. Zheng, K. Kashihara, T. Sato, and K. Sunagawa. A self-calibrating telemetry system for measurement of ventricular pressure-volume relations in conscious, freely moving rats. *American Journal of Physiology-Heart and Circulatory Physiology*, 287(6):H2906–H2913, 2004.

[37] A.M. Katz. *Physiology of the Heart*. Lippincott Williams & Wilkins, 2010.

[38] P. Nardinocchi, L. Teresi, and V. Varano. Myocardial contractions and the ventricular pressure–volume relationship. *arXiv preprint arXiv:1005.5292*, 2010.

[39] D. Burkhoff, I. Mirsky, and H. Suga. Assessment of systolic and diastolic ventricular properties via pressure-volume analysis: a guide for clinical, translational, and basic researchers. *American Journal of Physiology-Heart and Circulatory Physiology*, 289(2):H501–H512, 2005.

[40] H.L. Haber, E.R. Powers, L.W. Gimple, C.C. Wu, K. Subbiah, W.H. Johnson, and M.D. Feldman. Intracoronary angiotensin-converting enzyme inhibition improves diastolic function in patients with hypertensive left ventricular hypertrophy. *Circulation*, 89(6):2616–2625, 1994.

[41] T.P. Broten, S.D. Kivlighn, C.M. Harvey, A.L. Scott, T.W. Schorn, and P.K.S. Siegl. Techniques for the measurement of arterial blood pressure. *Measurement of cardiovascular function*, 1997.

[42] WH Ko, J. Hynecek, and S. Boettcher. Implantable pressure transducer for biomedical applications. In *27th Electronic Component Conf., Arlington, Virginia, May*, volume 16, 1959.

[43] Wen Hsiung Ko, J. Hynecek, and S.F. Boettcher. Development of a miniature pressure transducer for biomedical applications. *Electron Devices, IEEE Transactions on*, 26(12):1896 – 1905, dec 1979.

[44] F.W. Casadei, M. Gerold, and E. Baldinger. Implantable blood pressure telemetry system. *Biomedical Engineering, IEEE Transactions on*, (5):334–341, 1972.

[45] CG Caro. *The Mechanics of the circulation*. Oxford University Press (Oxford and New York), 1978.

[46] B.P. Brockway, P.A. Mills, and S.H. Azar. A new method for continuous chronic measurement and recording of blood pressure, heart rate and activity in the rat via radio-telemetry. *Clinical and Experimental Hypertension*, 13(5):885–895, 1991.

[47] S.E. Whitesall, J.B. Hoff, A.P. Vollmer, and L.G. D'Alecy. Comparison of simultaneous measurement of mouse systolic arterial blood pressure by radiotelemetry and tail-cuff methods. *American Journal of Physiology-Heart and Circulatory Physiology*, 286(6):H2408–H2415, 2004.

[48] J.A. Potkay. Long term, implantable blood pressure monitoring systems. *Biomedical microdevices*, 10(3):379–392, 2008.

[49] T.A. Bowdle et al. Complications of invasive monitoring. *Anesthesiology Clinics of North America*, 20(3):571, 2002.

[50] B.V. Scheer, A. Perel, and U.J. Pfeiffer. Clinical review: complications and risk factors of peripheral arterial catheters used for haemodynamic monitoring in anaesthesia and intensive care medicine. *Critical Care*, 6(3):199, 2002.

[51] EE Frezza, H. Mezghebe, et al. Indications and complications of arterial catheter use in surgical or medical intensive care units: analysis of 4932 patients. *The American Surgeon*, 64(2):127, 1998.

[52] RG Wilkins. Radial artery cannulation and ishaemic damage: a review. *Anaesthesia*, 40(9):896–899, 2007.

[53] S. Chatzandroulis, D. Tsoukalas, and P.A. Neukomm. A miniature pressure system with a capacitive sensor and a passive telemetry link for use in implantable applications. *Microelectromechanical Systems, Journal of*, 9(1):18–23, 2000.

[54] R. Pais, A. Duttaroy, M. Dobbs, and E. Pastalkova. Implantable blood pressure monitoring cuff for small laboratory animal. *NA*, 2010.

[55] J.F. James, T.E. Hewett, and J. Robbins. Cardiac physiology in transgenic mice. *Circulation research*, 82(4):407–415, 1998.

[56] F. Franco, S.K. Dubois, R.M. Peshock, and R.V. Shohet. Magnetic resonance imaging accurately estimates lv mass in a transgenic mouse model of cardiac hypertrophy. *American Journal of Physiology-Heart and Circulatory Physiology*, 274(2):H679–H683, 1998.

[57] Y.Q. Zhou, F.S. Foster, B.J. Nieman, L. Davidson, X.J. Chen, and R.M. Henkelman. Comprehensive transthoracic cardiac imaging in mice using ultrasound biomicroscopy with anatomical confirmation by magnetic resonance imaging. *Physiological genomics*, 18(2):232–244, 2004.

[58] M. Drangova, N.L. Ford, S.A. Detombe, A.R. Wheatley, and D.W. Holdsworth. Fast retrospectively gated quantitative four-dimensional (4d) cardiac micro computed tomography imaging of free-breathing mice. *Investigative radiology*, 42(2):85–94, 2007.

[59] G. Esposito, LF Santana, K. Dilly, J.D.S. Cruz, L. Mao, WJ Lederer, and H.A. Rockman. Cellular and functional defects in a mouse model of heart failure. *American Journal of Physiology-Heart and Circulatory Physiology*, 279(6):H3101–H3112, 2000.

[60] J. Baan, T.T.A. Jong, P.L.M. Kerkhof, R.J. Moene, A. D VAN DIJK, E. T VAN DER VELDE, and J. Koops. Continuous stroke volume and cardiac output from intraventricular dimensions obtained with impedance catheter. *Cardiovascular Research*, 15(6):328–334, 1981.

[61] M.D. Feldman, J.M. Erikson, Y. Mao, C.E. Korcarz, R.M. Lang, and G.L. Freeman. Validation of a mouse conductance system to determine lv volume: comparison to echocardiography and crystals. *American Journal of Physiology-Heart and Circulatory Physiology*, 279(4):H1698–H1707, 2000.

[62] E.B. Lankford, D.A. Kass, W.L. Maughan, and A.A. Shoukas. Does volume catheter parallel conductance vary during a cardiac cycle? *American Journal of Physiology-Heart and Circulatory Physiology*, 258(6):H1933–H1942, 1990.

[63] P.A. White, C.I.O. Brookes, H.B. Ravn, E.E. Stenbøg, T.D. Christensen, R.R. Chaturvedi, K. Sorensen, V.E. Hjortdal, and A.N. Redington. The effect of changing excitation frequency on parallel conductance in different sized hearts. *Cardiovascular research*, 38(3):668–675, 1998.

[64] T. J. Gawne, K. S. Gray, and R. E. Goldstein. Estimating left ventricular offset volume using dual-frequency conductance catheters. *Journal of Applied Physiology*, 63(2):872–876, 1987.

[65] D. Georgakopoulos and D.A. Kass. Estimation of parallel conductance by dual-frequency conductance catheter in mice. *American Journal of Physiology-Heart and Circulatory Physiology*, 279(1):H443–H450, 2000.

[66] C.L. Wei, J.W. Valvano, M.D. Feldman, and J.A. Pearce. Nonlinear conductance-volume relationship for murine conductance catheter measurement system. *Biomedical Engineering, IEEE Transactions on*, 52(10):1654–1661, 2005.

[67] J.E. Porterfield, A.T.G. Kottam, K. Raghavan, D. Escobedo, J.T. Jenkins, E.R. Larson, R.J. Treviño, J.W. Valvano, J.A. Pearce, and M.D. Feldman. Dynamic correction for parallel conductance, gp, and gain factor, $\alpha$, in invasive murine left ventricular volume measurements. *Journal of Applied Physiology*, 107(6):1693–1703, 2009.

[68] K. Raghavan, J.E. Porterfield, A.T.G. Kottam, M.D. Feldman, D. Escobedo, J.W. Valvano, and J.A. Pearce. Electrical conductivity and permittivity of murine myocardium. *Biomedical Engineering, IEEE Transactions on*, 56(8):2044–2053, 2009.

[69] S. Gabriel, RW Lau, and C. Gabriel. The dielectric properties of biological tissues: Ii. measurements in the frequency range 10 hz to 20 ghz. *Physics in medicine and biology*, 41:2251, 1996.

[70] M. Reyes, M.E. Steinhelper, J.A. Alvarez, D. Escobedo, J. Pearce, J.W. Valvano, B.H. Pollock, C.L. Wei, A. Kottam, D. Altman, et al. Impact of physiological variables and genetic background on myocardial frequency-resistivity relations in the intact beating murine heart. *American Journal of Physiology-Heart and Circulatory Physiology*, 291(4):H1659–H1669, 2006.

[71] C.L. Wei, J.W. Valvano, M.D. Feldman, M. Nahrendorf, R. Peshock, and J.A. Pearce. Volume catheter parallel conductance varies between end-systole and end-diastole. *Biomedical Engineering, IEEE Transactions on*, 54(8):1480–1489, 2007.

[72] Stanford Research Systems. *About Lock-In Amplfiers- Application Note 3*.

[73] J.H. Scofield. Frequency-domain description of a lock-in amplifier. *American Journal of Physics*, 62(2):129–132, 1994.

[74] M.L. Meade. Lock-in amplifiers: principles and applications. *Majalah LAPAN*, 1, 1983.

[75] A. De Marcellis, G. Ferri, A. D'Amico, C. Di Natale, and E. Martinelli. A fully-analog lock-in amplifier with automatic phase alignment for accurate measurements of ppb gas concentrations. *Sensors Journal, IEEE*, 12(5):1377–1383, 2012.

[76] M. Gabal, N. Medrano, B. Calvo, and S. Celma. A low-voltage single-supply analog lock-in amplifier for wireless embedded applications. In *Smart Objects: Systems, Technologies and Applications (RFID Sys Tech), 2010 European Workshop on*, pages 1–6. VDE, 2010.

[77] J. Aguirre, N. Medrano, B. Calvo, and S. Celma. Lock-in amplifier for portable sensing systems. *Electronics letters*, 47(21):1172–1173, 2011.

[78] G. de Graaf and RF Wolffenbuttel. Lock-in amplifier techniques for low-frequency modulated sensor applications. In *Instrumentation and Measurement Technology Conference (I2MTC), 2012 IEEE International*, pages 1745–1749. IEEE, 2012.

[79] Shawon Senjuti, Kyle Fricke, Anestis Dounavis, and Robert Sobot. Misalignment analysis of resonance-based wireless power transfer to biomedical implants. In *Electrical Computer Engineering (CCECE), 2012 25th IEEE Canadian Conference on*, pages 1 –5, 29 2012-may 2 2012.

[80] Texas Instruments. *MSP430X22X4 Mixed Signal Microcontroller*. SLAS504D, July 2006.

[81] Texas Instruments. *MSP430X2XX Family User's Guide*. SLAU144e, 2008.

[82] GE. *GE P161 3F Gauge Pressure Sensor Die*. General Electric, 2012.

[83] R. Mancini. *Op amps for everyone*. Newnes, 2003.

[84] Analog Devices. *Analog Devices AD8519 Datasheet*, 2007.

[85] F.G. Stremler. Introduction to communication systems. *Introduction to Communication Systems, 3rd edition by Ferrel G. Stremler, 3rd edition, Addison-Wesley, 770 p., ISBN: 0201184982*, 1, 1990.

[86] Samtec. *Samtec CLE - Datasheet*, 2011.

[87] Samtec. *Samtec FTE - Datasheet*, 2011.

[88] Niels Kirkeby Nithya Subramanian. *Anaren 0404 balun optimized for TI CC2500 Transceiver*. Anaren, April 2008.

[89] Tyco Electronics. *UMCC – Ultraminiatrue Coax Connector & Cable Assembly Series*, 2007.

[90] Molex. *Molex SlimStack 0.4mm Pitch Board-to-Board Connectors*, July 2012.

[91] Molex. *Molex SlimStack 0.4mm Pitch Board-to-Board Connectors*, July 2012.

[92] Molex. *0.50mm Pitch SMT Right-Angle FFC/FPC Connector*, March 2012.

[93] M. Mark, Y. Chen, C. Sutardja, C. Tang, S. Gowda, M. Wagner, D. Werthimer, and J. Rabaey. A $1mm^3$ 2mbps 330fj/b transponder for implanted neural sensors. In *VLSI Circuits (VLSIC), 2011 Symposium on*, pages 168–169. IEEE, 2011.

[94] K. Jensen, J. Weldon, H. Garcia, and A. Zettl. Nanotube radio. *Nano letters*, 7(11):3508–3511, 2007.

# Curriculum Vitae

| | |
|---|---|
| **Name:** | Kyle Fricke |
| **Post-Secondary Education and Degrees:** | The University of Western Ontario<br>London, Ontario, Canada<br>2006 – 2010 B.E.Sc. |
| **Honours and Awards:** | Ontario Graduate Scholarship<br>2012 |
| **Related Work Experience:** | Teaching Assistant<br>The University of Western Ontario<br>2010 - 2012 |

**Publications:**

[1] K. Fricke, R. Sobot, and A. Dounavis. Analogue portable electrooculogram real-time signal processor. International Journal of Circuit Theory and Applications, 2012.

[2] S. Popa, K. Fricke, R. Sobot, "Calibration and Finite Element Numerical Analysis of an Admittance Based Volume Sensor for the Murine Heart", IEEE International Conference for Upcoming Engineers, (ICUE) 2012, August 2, 2012, Toronto ON, Canada

[3] L. Luo, K. D. Gannes, K. Fricke, S. Senjuti, R. Sobot, "Low – Power CMOS Voltage Regulator Architecture for Implantable RF Circuits", 4th International IEEE EURASIP Workshop on RFID Technology, EURASIP, September 27 – 28, 2012, Torino, Italy

[4] S. Senjuti, K. Fricke, A. Dounavis, and R. Sobot. Misalignment analysis of resonance–based wireless power transfer to biomedical implants. In Electrical Computer Engineering (CCECE), 2012 25th IEEE Canadian Conference on, pages 1–5, 29 2012-may 2 2012.